

**Best  
Available  
Copy**

AD-A008 870

COMPLEX REFRACTIVE INDEX OF ICE FOG AT A RADIO  
WAVELENGTH OF 3MM

John W. Perry, et al

Texas University at Austin

Prepared for:

Cold Regions Research and Engineering Laboratory  
Advanced Research Projects Agency

October 1974

DISTRIBUTED BY:

**NTIS**

National Technical Information Service  
U. S. DEPARTMENT OF COMMERCE

# COMPLEX REFRACTIVE INDEX OF ICE FOG AT A RADIO WAVELENGTH OF 3 MM

John W. Perry  
Archie W. Straiton and Bob M. Fannin

October 1974

PREPARED FOR  
ADVANCED RESEARCH PROJECTS AGENCY  
ARPA ORDER 1615

BY

CORPS OF ENGINEERS, U.S. ARMY  
**COLD REGIONS RESEARCH AND ENGINEERING LABORATORY**  
HANOVER, NEW HAMPSHIRE

*ib*

APPROVED FOR PUBLIC RELEASE; DISTRIBUTION UNLIMITED.

**PREFACE**

This report was prepared by Dr. John W. Perry, Archie W. Straiton and Bob M. Fannin of the Millimeter Wave Group, Electrical Engineering Research Laboratory, The University of Texas at Austin, under Grant DA-ENG-27021-73-G39. The work was performed as part of the Advanced Research Projects Agency's Arctic Surface Effect Vehicle program under ARPA Order 1615, Dr. Pieter Hoekstra and Dr. Richard Munis monitored the project for USA CRREL.

Technical review of the report was performed by Dr. Roger Berger of USA CRREL.

The findings in this report are not to be construed as an official Department of the Army position unless so designated by other authorized documents.

ACCESSION for	
NTIS	White Section <input checked="" type="checkbox"/>
DDC	Buff Section <input type="checkbox"/>
UNANNOUNCED	<input type="checkbox"/>
JUSTIFICATION	
BY	
DISTRIBUTION/AVAILABILITY CODES	
Dist.	AVAIL. and/or SPECIAL
A	

Unclassified

AD-A008870

Security Classification		<b>DOCUMENT CONTROL DATA - R &amp; D</b>	
<i>Security classification of title, body of abstract and indexing annotation must be entered when the overall report is classified</i>			
1. ORIGINATING ACTIVITY (Corporate author) U.S. Army Cold Regions Research and Engineering Laboratory Hanover, New Hampshire 03755		2a. REPORT SECURITY CLASSIFICATION Unclassified	
3. REPORT TITLE COMPLEX REFRACTIVE INDEX OF ICE FOG AT A RADIO WAVELENGTH OF 3 MM		2b. GROUP	
4. DESCRIPTIVE NOTES (Type of report and inclusive dates)			
5. AUTHOR(S) (First name, middle initial, last name) John W. Perry, Archie W. Straiton and Bob M. Fannin			
6. REPORT DATE October 1974		7a. TOTAL NO. OF PAGES <del>103</del> 104	7b. NO. OF REFS 89
8a. CONTRACT OR GRANT NO. DA-ENG-27021-73-G39		9a. ORIGINATOR'S REPORT NUMBER(S) Technical Report 255	
8b. PROJECT NO. ARPA Order 1615		9b. OTHER REPORT NO(S) (Any other numbers that may be assigned this report)	
10. DISTRIBUTION STATEMENT Approved for public release; distribution unlimited.			
11. SUPPLEMENTARY NOTES Reproduced by NATIONAL TECHNICAL INFORMATION SERVICE U.S. Department of Commerce Springfield, VA. 22151		12. SPONSORING MILITARY ACTIVITY Advanced Research Projects Agency 1400 Wilson Blvd. Arlington, Va. 22209	
13. ABSTRACT An investigation of the complex index of refraction at 97 GHz for low temperature ice fogs was carried out over the temperature interval -30° to -48°C in a specially constructed environmental chamber of approximately 70 cubic foot volume. A Fabry-Perot semi-confocal cavity, consisting of a 6-in.-diam aluminum spherical mirror of a 72-in. radius of curvature and a copper flat plate separated 36 in. from the spherical mirror, was used to make the electromagnetic measurements. Waveguide feeds brought through the back of the flat plate coupled energy into and out of the cavity. The complex index of refraction of the ice fog medium in the fields of the Fabry-Perot resonant cavity were found from the change in the resonant frequency and amplitude response of the cavity when the fog was present. The fog could be controlled and introduced to the cold chamber from an external steam source, and a blower located inside the chamber was used to mix and dissipate the fog as desired. A phase locking technique was used to sweep the klystron signal source over the response range of the Fabry-Perot cavity. The sweep frequency was beat with known marker frequency oscillators to			

DD FORM 1473

REPLACES DD FORM 1473, 1 JAN 66, WHICH IS OBSOLETE FOR ARMY USE.

Unclassified  
Security Classification

Security Classification

KEY WORDS	LINK A		LINK B		LINK C	
	ROLE	WT	ROLE	WT	ROLE	WT
Air cushion vehicles Ground effect machines Ice fog Millimeter waves Refractivity Surface effect vehicles						
13. Abstract (Cont'd)  provide reference markers, and this, plus the output of the loosely coupled square law detector connected to the Fabry-Perot cavity, was put on an oscilloscope and photographed for later study. The cavity frequency change was measured by positioning the marker frequency beats at the peak of the cavity response before and after the ice fog was admitted. Ice fog particle number-density measurements, together with the measured extinction of a helium-neon laser (6328Å), were used to help characterize the fog properties at the time of the electromagnetic measurements. For the fogs studied in this experiment, corresponding to 1 dB/m of laser extinction, measured refractive index changes of 1 to 2 N-units occurred, and the extinction was about $5 \times 10^{-7} \text{ cm}^{-1}$ at the lower temperatures, and reached 3 or $4 \times 10^{-6} \text{ cm}^{-1}$ at the $-30^{\circ}\text{C}$ upper temperature limit. A literature search indicated there were no reported complex dielectric constant measurements of ice at 97 GHz. The complex dielectric constant of ice is important both for understanding 3-mm radio wave propagation in an arctic environment and for some of the theoretical development of this ice fog research. Accordingly, these measurements were made for laboratory prepared slab-ice samples and the results are reported						

herein.

*ia*

Unclassified

Security Classification

## CONTENTS

	Page
I. Introduction.....	1
General .....	1
Problem description .....	1
Method of presentation .....	2
II. Complex permittivity measurements of solid ice .....	3
Introduction .....	3
Review of the literature on dielectric behavior of ice .....	3
Theory of dielectric measurements.....	7
Instrumentation for ice dielectric measurements .....	12
Calibrations with polystyrene and water samples .....	13
Results for ice.....	20
III. The meteorology of ice fog .....	24
Introduction .....	24
Physical distinguishing characteristics and optical properties.....	25
Ice fog crystal size and formation .....	26
Ice crystal density distribution .....	28
The role of nuclei and low temperatures in crystal formation .....	28
Phase change effects on development of ice fog .....	30
IV. Dielectric behavior of a medium with homogeneously distributed particles...	31
Dielectric behavior of a medium of small particles .....	31
Radio wave energy loss mechanisms .....	33
V. Method for making complex permittivity measurements of a fog .....	26
Literature review of millimeter wave Fabry-Perot interferometry .....	36
Theoretical considerations .....	37
VI. Instrumentation .....	43
Electronic frequency locking system .....	43
Environmental chamber and refrigeration system .....	47
VII. Measurements .....	51
FPS operation .....	51
FPS mirror effects.....	54
Ice fog particle measurements.....	55
Electromagnetic measurements and applications: one-way propagation through ice fog .....	63
Comparison of computed and measured values .....	71
VIII. Summary and conclusions .....	75
Literature cited .....	79
Appendix .....	85
Abstract .....	99

## ILLUSTRATIONS

Figure	Page
1. Complex dielectric spectrum of water and ice .....	7
2. Geometry of dielectric material holder .....	10
3. Phase relative delay as a function of dielectric thickness .....	11
4. Quasi-optical free-space method of measuring complex permittivity, $\epsilon'$ and $\epsilon''$ .....	12
5. Phase relationship of transmitted and reference fields in the slotted line section for the null condition .....	13
6. Polystyrene phase shift curve .....	14
7. Polystyrene attenuation curve .....	15
8. Holder arrangement for water samples .....	15
9. Phase shift curve for distilled water .....	16
10. Phase shift curve for lake water .....	17
11. Attenuation curve for distilled water .....	17
12. Attenuation curve for rain water .....	18
13. Attenuation curve for lake water .....	18
14. Phase shift curve, ice made from distilled water, $T = -28^{\circ}\text{C}$ .....	20
15. Phase shift curve, ice made from distilled water, $T = -28^{\circ}\text{C}$ .....	21
16. Phase shift curve, ice made from lake water, $T = -28.5^{\circ}\text{C}$ .....	21
17. Phase shift curve, ice made from lake water, $T = -30.5^{\circ}\text{C}$ .....	22
18. Attenuation curve, ice made from distilled water, $T = -28^{\circ}\text{C}$ .....	22
19. Attenuation curve, ice made from lake water, $T = -28.5^{\circ}\text{C}$ .....	23
20. Small snow crystals .....	26
21. "Diamond dust" crystals of about 0.1 mm diameter .....	27
22. Ice fog crystals collected from a dense ice fog in a Fairbanks, Alaska, supermarket parking lot .....	27
23. Relationship between mean diameters of total ice-fog crystals and temperatures .....	29
24. Confocal and semi-confocal Fabry-Perot interferometers .....	37
25. Terminology appropriate to theoretical treatment of FPS .....	39
26. Power loss per transit vs $N = a^2/b\lambda$ for confocal spherical mirrors .....	39
27. Amplitude distribution of $\text{TEM}_{00q}$ mode .....	41
28. Two views of cold chamber interior, showing details of evaporator mounting and FPS placement .....	43
29. Block diagram of classical millimeter-wave frequency measuring system using variable-frequency markers .....	44
30. Instrumentation for phase locking and sweeping of FPS cavity at 96.5 GHz .....	45
31. Triplexer assembly .....	46
32. View of electronic hardware associated with klystron phase locking system .....	47
33. Further details of environmental chamber and peripheral equipment .....	48
34. Environmental chamber floor plan and equipment layout .....	49
35. Laser extinction due to 0.3 normal density optical filter .....	50
36. Teapot mode of steam fog production .....	51
37. Fabry-Perot response curves in laboratory environment .....	53
38. Cavity response curves in dry, cold chamber with no fog .....	53
39. Method for photographing ice particle accumulations on mirrors .....	54
40. Photographs made from 6328 Å light scattered by particles on mirror surface .....	55
41. Liberally dusting mirror with 3- $\mu$ polystyrene dust produces almost no effect .....	56

Figure	Page
42. $Q$ -perturbation due to a thin film of water on mirror surface.....	56
43. Photomicrographs of 10 $\mu$ and 7 $\mu$ craters left by ice fog particles on a magnesium oxide slide .....	57
44. Assumed number-density distribution used in laser extinction computations	61
45. Normalized ice fog N-unit measurements at 97 GHz .....	64
46. Normalized ice fog extinction coefficient measurements at 97 GHz .....	65
47. Sample cavity response due to ice fog, $T = -30^{\circ}\text{C}$ .....	66
48. Sample cavity response due to ice fog, $T = -30^{\circ}\text{C}$ .....	66
49. Sample cavity response due to ice fog, $T = -35^{\circ}\text{C}$ .....	67
50. Sample cavity response due to ice fog, $T = -35^{\circ}\text{C}$ .....	67
51. Sample cavity response due to ice fog, $T = -39^{\circ}\text{C}$ .....	68
52. Sample cavity response due to ice fog, $T = -39^{\circ}\text{C}$ .....	68
53. Sample cavity response due to ice fog, $T = -43^{\circ}\text{C}$ .....	69
54. Sample cavity response due to ice fog, $T = -43^{\circ}\text{C}$ .....	69
55. Sample cavity response due to ice fog, $T = -46.5^{\circ}\text{C}$ .....	70
56. Sample cavity response due to ice fog, $T = -46.5^{\circ}\text{C}$ .....	70

### TABLES

Table	Page
I. Complex permittivity of glacier ice core samples from 150 MHz to 1 GHz..	5
II. Reported complex permittivity of ice .....	8
III. Complex permittivity of polystyrene and water samples at 96.5 GHz .....	19
IV. Measured complex permittivity of ice at 96.5 GHz .....	23
V. Complex scattering coefficients and attenuation cross sections for ice particles at 96.5 GHz .....	35
VI. Measured particle diameter .....	58
VII. Gross statistics .....	59
VIII. Calculated and measured 6328 Å optical properties of ice fog.....	60
IX. Optical extinction cross section for ice spheres at 6328 Å .....	60
X. Electromagnetic measurements, normalized to 1 dB/m at 6328 Å extinction	62
XI. Propagation constants of ice fogs at 97 GHz for 1 dB/m extinction of 6328 Å red light .....	69
XII. One-way radio wave propagation effects .....	70

1.

## COMPLEX REFRACTIVE INDEX OF ICE FOG AT A RADIO WAVELENGTH OF 3 MM

by

John W. Perry, Archie W. Straiton and Bob M. Fannin

### I. INTRODUCTION

#### General

The last decade has seen a strong trend toward expanding commercial communications from the highly congested low-frequency channels into the UHF microwave and millimeter wave spectrum. This move toward using higher and higher frequencies has been helped along considerably by the increasing use of satellite-borne millimeter wave transponders and the increasing pressure for higher data bit rates.

The millimeter wave region is a transition region between the radio (long-wave) domain and the infrared region. Many of the problems and peculiarities of this domain are unique. Molecular absorption becomes important, and absorption and scattering by raindrops represents a severe atmospheric limitation for communication links. Thermal (blackbody) radiation becomes increasingly more important as a source of background noise, and at the same time millimeter wave hardware such as harmonic generators, mixers and sources are at about their maximum usable frequencies, particularly when operating at 90 GHz and above.

Since atmospheric behavior represents one of the most important factors in millimeter wave propagation, much effort has been made to understand and study its effects. However, most of this effort has been devoted to the warm atmosphere.

#### Problem description

Very little is known of the effects of arctic and subarctic atmospheric propagation on millimeter waves. It is important to understand and study these effects because in recent years extensive efforts have been underway to link arctic communities with the rest of the world by ground-based and satellite-based links. Recently a 95-GHz pulse-type radar was planned to be used on a surface effect vehicle for navigation/guidance purposes. This proposed vehicle would travel at high speeds (up to 100 knots or about 115 mph) over water, ice and open tundra surfaces, and since it has limited deceleration characteristics it must be capable of detecting ice objects and other obstacles far enough in advance to be able to change course or slow down. This 3-mm radar looks horizontally at low grazing angles and must be capable of penetrating fog and snow (at least light, dry snow).

In arctic areas ice fog is a common occurrence. Ice fog is a low temperature phenomenon, and almost never forms at temperatures above about  $-30^{\circ}\text{C}$ . Ice fogs form where open sea water leads

## 2 COMPLEX REFRACTIVE INDEX OF ICE FOG AT A RADIO WAVELENGTH OF 3 MM

form in cracks in sea ice packs; where warm, moist air is advected over cold, dry areas; or where moist air from natural hot springs, cooling tower stacks, or industrial or automobile exhausts is injected into cold, dry air. The transition from a liquid state to an all solid state takes place between  $-30^{\circ}$  and about  $-36^{\circ}\text{C}$ , and it is in this region that the maximum radio signal absorption effects are expected to occur. Extremely dense ice fogs have been observed in arctic areas, and their extent and duration have proven to be very disruptive to airport and other commercial and private activities.

Very little is known about the effects of ice fogs on 3-mm radio wave propagation, particularly in the transition temperature interval  $-30^{\circ}$  to  $-36^{\circ}\text{C}$ . It has been the goal of this research to measure the complex index of refraction, phase constant, and signal loss associated with ice fogs of uniform density formed over the temperature interval  $-30^{\circ}$  to  $-48^{\circ}\text{C}$ .

Since this was to be a laboratory experiment, it was necessary to construct an environmental chamber especially suited for making these low temperature fog measurements. The chamber so constructed has a volume of  $70\text{ ft}^3$  and a temperature control capability down to  $-50^{\circ}\text{C}$ .

Fog particle size measurements were made with an impactor to help characterize the fog but, for reasons shown later, a far more accurate indication of fog uniformity was given by continuously monitoring the extinction of a  $6328\text{ \AA}$  helium-neon laser beam shot through a prescribed path in the ice fog. In this manner, a "reference fog level" can be readily attained for each operating temperature.

A high-Q Fabry-Perot cavity was designed and constructed for making the electromagnetic measurements to determine the complex index of refraction of the fog. The resonant frequency change and signal amplitude change of the cavity due to the introduction of the fog were measured by a method devised for phase locking and sweeping the klystron signal source over the cavity response frequency range. A high degree of frequency stability and precision frequency measurement was attained in this manner.

As a supplement to these electromagnetic ice fog measurements, the complex dielectric constant of slab ice was measured. The authors could not find any reported dielectric constant measurements of ice at 3 mm. These measurements are an obvious asset for the theoretical calculation of ice reflections, and the backscattering and extinction cross sections of hail at 3 mm. These ice measurements were made separately using a free-space quasi-optical technique commonly described in the literature.

### Method of presentation

As far as the presentation of the material is concerned, it was deemed appropriate to present first the results for the slab ice complex dielectric constant measurements. The literature review of solid ice permittivity measurements, instrumentation, and calibration techniques was incorporated in the same chapter (Chapter II).

Chapter III is concerned with the meteorology and the appropriate literature research of arctic ice fog formation.

Chapter IV is devoted to a theoretical development of the dielectric behavior of a gas with homogeneously distributed small dielectric spheres.

Chapters V and VI are devoted to describing theoretically the Fabry-Perot cavity used in these measurements and the means of electronically generating and sweeping the signal over the response frequency of the cavity. It is in this section on instrumentation that the refrigeration chamber and laser extinction measurement methods are described. Literature surveys are included where appropriate.

The measurements and results are treated fully in Chapter VII. The early sections in this chapter are devoted to analyzing empirically the effects of ice accumulation on the mirrors. Data analysis and application to one-way signal propagation are treated here, and the results appropriate to propagation through fogs of a given reference laser extinction are plotted and tabulated.

## II. COMPLEX PERMITTIVITY MEASUREMENTS OF SOLID ICE

### Introduction

In microwave remote sensing applications, the dielectric constant of the material being sensed is a very important parameter. The backscattering cross section of an ice sphere in a thunderstorm, when struck by a radar wave, is a function of the sphere circumference in wavelengths and the dielectric constant of the material. Mie's (1908) treatment of the scattering and extinction cross sections of dielectric spheres was restated by Stratton (1941), and numerical methods of machine computing the  $n^{\text{th}}$  electric and magnetic modes involved in these calculations have been devised (Aden 1950).

In order to model the complex permittivity of a low temperature ice fog, it is necessary to have a knowledge of the complex permittivity of ice. No published data appropriate to the operating frequency of 96 GHz exist. Inference from published data at other frequencies leads to inconsistent conclusions. It is therefore appropriate to make dielectric constant measurements of ice at 96 GHz. This chapter contains a literature survey of the available published data for ice, and details the theory of dielectric measurements and the instrumentation, calibrations and results for ice at this frequency.

### Review of the literature on dielectric behavior of ice

Ice can occur in six allotropic forms for pressures in excess of 2000 atmospheres (Bertie and Whalley 1964), and for pressures of 1000 atmospheres or less, ice can occur in the normal hexagonal ( $I_h$ ), cubic ( $I_c$ ), or amorphous state, depending upon temperature and the method of preparation (Bertie and Whalley 1964, Lonsdale 1958). Between about  $0^\circ$  and  $-80^\circ\text{C}$  the equilibrium form of ice is the normal hexagonal form  $I_h$ . For temperatures below  $-80^\circ\text{C}$  and above  $-130^\circ\text{C}$  ice may exist in the cubic form  $I_c$ , and below about  $-130^\circ\text{C}$  ice may be in the amorphous form. These temperatures are approximate since disagreement exists in the literature as to the exact boundary values. However, as it occurs naturally in the terrestrial environment, the normal form of crystalline ice is  $I_h$ . While it is important to recognize what possible crystalline forms ice can take, it is not important to the purpose of this research to further discuss these forms since for all practical temperatures and forms (slab ice, snow, hail and ice fog) only  $I_h$  exists.

Irvine and Pollack (1968) reviewed the literature on the absorption coefficient and reflectivity of both water and ice, and for each phase they tabulated both the real and imaginary parts of the index of refraction ( $m = n' - jn''$ ) for wavelengths between 0.95 and 152 microns. Their values of the complex index of refraction are well accepted in this wavelength interval.

The microwave values for the complex refractive index of ice given by Gunn and East (1954) are for  $n' = 1.78$  at all temperatures and  $n'' = 24 \times 10^{-4}$  at  $0^\circ\text{C}$ ,  $8 \times 10^{-4}$  at  $-10^\circ\text{C}$ , and  $6 \times 10^{-4}$  at  $-20^\circ\text{C}$ . These values are based upon the work of Dunsmuir and Lamb (1945), Lamb (1946), Lamb and Turney (1949), and Cumming (1952) over the centimeter band. Lamb (1946) used a cavity operating at 3 cm (10 GHz) and found a relative permittivity of 3.05. However, he later found a 4% error in his measurements due to effects from an ice holder cup in his cavity, and Lamb and Turney (1949) repeated these cavity dielectric measurements at 3-cm and 1.25-cm wavelengths (10 and 24 GHz). They reported a relative permittivity near 3.17 at both frequencies near  $0^\circ\text{C}$ , and this value

changed only slightly for temperatures down to  $-195^{\circ}\text{C}$ . Dunsmuir and Lamb (1945) and Lamb (1946) reported that the loss tangent of their ice samples varied from  $12 \times 10^{-4}$  at  $0^{\circ}\text{C}$  to  $1.9 \times 10^{-4}$  at  $-20^{\circ}\text{C}$ , and to nearly  $1.3 \times 10^{-4}$  at  $-40^{\circ}\text{C}$ .

Cumming (1952) later used a measuring technique employing a section of waveguide filled with ice to make permittivity and loss measurements at 3.2-cm wavelength. Cumming found a relative permittivity of 3.15 independent of temperature (over a temperature range of  $0^{\circ}$  to  $-20^{\circ}\text{C}$ ) at this wavelength. In terms of the imaginary part of the complex index of refraction, Cumming found loss tangent values about twice those of Lamb, with measurements of  $23 \times 10^{-4}$  at  $0^{\circ}\text{C}$ ,  $7.9 \times 10^{-4}$  at  $-10^{\circ}\text{C}$ , and  $5.5 \times 10^{-4}$  at  $-20^{\circ}\text{C}$ . His measurements have been considered to be the best, even though made only over a  $0^{\circ}$  to  $-20^{\circ}\text{C}$  temperature range and at 3.2-cm wavelength.

Perry and Straiton (1972) reported making complex permittivity measurements on slab ice at 35 and 94 GHz. These measurements were made using a quasi-optical free space technique. A discussion of this technique is deferred to a later section dealing with the theory of dielectric measurements as made on slab ice at 96 GHz. The results presented by Perry and Straiton for the relative dielectric constant, 1.91, are better than 30% below the low frequency value given by Lamb, etc. Since the temperature control exerted over these ice samples was poor, and since an error in the phase shift interpretation was found, these measurements were repeated in an environmental chamber. The results of these recent measurements are deferred to a later section.

Von Hippel (1954) reports measurements made by Westphal on ice at  $-12^{\circ}\text{C}$  over the frequency range 0.1 MHz to 10 GHz. His results, 3.20 at 3 GHz and 3.17 at 10 GHz, are in accord with the above results of Cumming. Between 1 MHz and 1 GHz his measured results were surprisingly high, being 4.8 at 0.1 MHz, 4.15 at 1 MHz, and 3.7 at 10 MHz. At these frequencies  $\tan \delta$  was found to be  $9 \times 10^{-4}$ ,  $7 \times 10^{-4}$ ,  $8000 \times 10^{-4}$ ,  $1200 \times 10^{-4}$  and  $180 \times 10^{-4}$ , respectively.

Yoshino (1961) made dielectric constant measurements between 1 MHz and 3 GHz on Antarctic ice core samples over the temperature range  $-18^{\circ}$  to  $-36^{\circ}\text{C}$ . His results are in accord with Von Hippel's measurements over this frequency range, being nearly 4.0 at 5 MHz, 3.8 at 10 MHz, 3.45 at 100 MHz and about 3.3 at 3 GHz.

These results in the intermediate (HF-UHF) frequency range of both Von Hippel (1954) and Yoshino (1961) are surprisingly high and in good agreement with each other in this interval.

More recently, Ragle, Blair and Persson (1964) reported on Westphal's dielectric measurements of glacier ice made from 150 MHz to 1 GHz and from  $1^{\circ}$  to  $-60^{\circ}\text{C}$  (Table I). These measurements are significantly below what Von Hippel (1954) and Yoshino (1961) had reported over this frequency range, and aside from the decrease in the second significant figure of the dielectric constant with increasing frequency, the dielectric constant is approximately constant at 2.9, both with temperature and frequency. The loss tangent, however, decreases both with decreasing temperature and increasing frequency, except at 1 GHz, where it is reported to be constant with decreasing temperature.

Ray (1971) made an empirical model of the complex refractive indices for ice and liquid water which is applicable from  $-20^{\circ}$  to  $0^{\circ}\text{C}$  for ice and from  $-20^{\circ}$  to  $50^{\circ}\text{C}$  for water. His model extends from  $2 \mu$  to several thousand kilometers in wavelength for ice. His expressions are of value in that they fit quite well the majority of the absorption bands in the infrared and optical parts of the spectrum. In the radio frequency part of the spectrum he adjusted his expressions to best fit the data of Cumming (1952), Lamb (1946) and Lamb and Turney (1949), and for a single relaxation time effect and no losses ( $\sigma = 0$ ) his model reduces to the classical Debye expression.

Worz and Cole (1969) made static dielectric constant measurements of redistilled water samples further purified by zone refining techniques to yield dc conductivities as low as  $4 \times 10^{-11}$  mho/cm at  $-10^{\circ}\text{C}$ . Their measurements were made over the temperature interval  $0^{\circ}$  to  $-80^{\circ}\text{C}$ . From their measured data, the equation best describing the static dielectric constant is of the form

**Table I. Complex permittivity of glacier ice core samples from 150 MHz to 1 GHz.**

(After measurements made by Westphal and reported by Ragle, Blair and Persson 1964.)

Temp (°C)	150 MHz	300 MHz	500 MHz	1000 MHz
<b>Dielectric constant</b>				
-1	2.95	2.94	2.93	2.93
-10	2.92	2.92	2.915	2.915
-20	2.91	2.91	2.91	2.91
-60	2.90	2.90	2.90	2.90
<b>Loss tangent</b>				
-1	0.00200	0.00108	0.00052	0.0004
-10	0.00110	0.00056	0.00028	0.0004
-20	0.00068	0.00034	0.00019	0.0004
-60	0.00005	0.00003	0.00003	0.0004

$$\epsilon_0 - \epsilon_\infty = \frac{20,715}{T - 38}$$

and  $\epsilon_\infty$  is taken to be 3.1. The relaxation time of the ice thus prepared was found to obey an Arrhenius rate equation of the form

$$\tau = Ae^{(E/RT)}$$

where  $A = 5.3 \times 10^{-16}$  sec

$E = 13.2$  kcal/mole =  $5.526576 \times 10^4$  J/mole

$R = 8.3143$  J/K - mole

and is in good agreement with the relaxation times measured by Auty and Cole (1952) in the temperature range above  $-50^\circ\text{C}$ . Worz and Cole (1969) give slightly higher values for the static dielectric constant of ice at very low temperatures, and their results are probably better than Auty and Cole's (1952) findings ( $0^\circ$  to  $-66^\circ\text{C}$ ) due to the care taken to reduce the dc conductivity of their water samples.

Perhaps the easiest way to understand what is meant by the relaxation time is to visualize the molecular dipoles as tiny spheres, as Debye (1929) did in his original theory. The rotation of these spheres in a viscous medium is opposed by forces related by Stoke's law to the macroscopic viscosity  $\eta$  of the surrounding medium, and Debye (1929) deduced that

$$\tau = \frac{4\pi\eta a^3}{kT}$$

where  $a$  = molecular radius.

6 COMPLEX REFRACTIVE INDEX OF ICE FOG AT A RADIO WAVELENGTH OF 3 MM

It is interesting to put some numbers, appropriate for water, into this simple expression for relaxation time. Water, at room temperature (about +20°C), has a viscosity of  $\eta = 0.01$ , and the "radius" of the water molecule is about  $2 \times 10^{-10}$  m, giving a  $\tau$  of  $0.25 \times 10^{-10}$  sec. The relaxation time of water is in fact associated with an absorption peak in the centimeter band. This "sphere" model of Debye's is really only important in that it postulates that the orientation of polar molecules in liquids and solids leads spectroscopically to a simple relaxation spectrum, which is indeed what is observed.

More recent approaches to the problem of dipole relaxation have involved the idea that the dipole activity rotates between two positions of equilibrium separated by a potential energy barrier. If the height of this energy barrier is written as  $D$ , then the relaxation time - which is a measure of the transition probability - is given by a relation of the form

$$\tau = \frac{C}{\omega} e^{D/kT} = \tau_0 e^{E/RT}$$

where  $R = k \times M$ ,  $C$  is only slightly temperature dependent, and  $\pi/\omega$  is the average time required by an excited molecule to turn from one equilibrium direction to the other (Saxton 1952).

The relaxation time of ice increases with decreasing temperature. Auty and Cole (1952) and Worz and Cole (1969) report  $\tau$  to range from about  $2 \times 10^{-5}$  sec at 0°C to  $2.5 \times 10^{-3}$  sec at -45°C. It is interesting to compare these relaxation times of ice with the relaxation times of water. Saxton (1952) has measured  $\tau$  of water to be  $1.87 \times 10^{-11}$  at 0°C to about  $6 \times 10^{-12}$  at 40°C. Thus water has a relaxation time about  $10^{-6}$  that of ice.

At least in a first approximation, both water and ice traverse a simple Debye relaxation spectrum since only one relaxation time has been found for each phase over the known radio wave spectrum (Eisenberg and Kouznamm 1969). Thus the relative dielectric constant  $\epsilon'/\epsilon_0$  and dielectric loss  $\epsilon''/\epsilon_0$  are given by the expressions

$$k' = \frac{\epsilon'}{\epsilon_0} = \frac{\epsilon'_\infty}{\epsilon_0} + \frac{\epsilon'_s - \epsilon'_\infty}{\epsilon_0(1 + \omega^2\tau^2)}$$

$$k'' = \frac{\epsilon''}{\epsilon_0} = \frac{(\epsilon'_s - \epsilon'_\infty)\omega\tau}{\epsilon_0(1 + \omega^2\tau^2)}$$

where  $\epsilon'_\infty/\epsilon_0$  is the limiting value of the high frequency dielectric constant and  $\epsilon'_s/\epsilon_0$  is the static (dc) dielectric constant.

The principal dielectric loss of water at low frequencies (frequencies below 100 MHz) is due primarily to free charge carriers, such as ions and other free radicals. This dielectric loss mechanism, caused by the dc conductivity of the water, decreases with increasing frequency according to the relationship

$$\frac{\epsilon''(\omega)}{\epsilon_0} = \frac{\sigma}{\epsilon_0\omega}$$

where  $\sigma$  is measured in mhos/meter.

At high frequencies, the dielectric loss of water is due primarily to viscous friction losses associated with the rotation of the polarized water molecules as they follow the incident electromagnetic radiation. Ions and other radicals cannot contribute significantly to the dielectric loss since they are just too massive to follow the incident electric field variations.

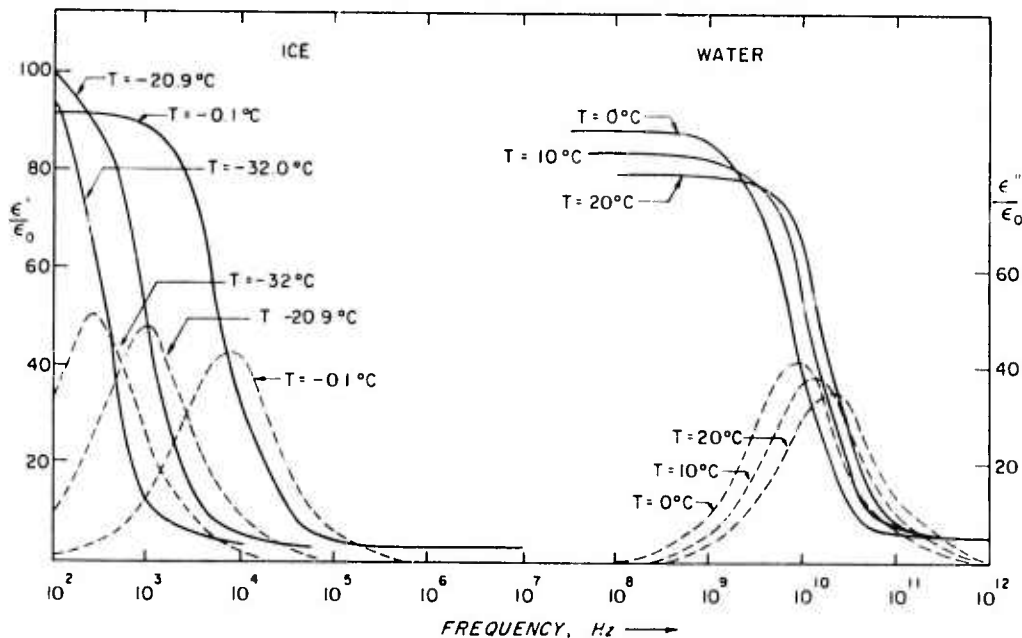


Figure 1. Complex dielectric spectrum of water and ice.

Figure 1 shows the dielectric spectrum of ice and water at various temperatures as calculated from the Debye equations with the appropriate relaxation times and static dielectric constants. For ice, the Worz-Cole expression for the static dielectric constant was used, and the relaxation times for each temperature were taken directly from Auty and Cole's paper. In the case of ice,  $\epsilon_\infty$  was taken to be 3.1. For water, the relaxation times and static dielectric constants appropriate for each temperature were obtained from a tabulation in Kerr's book (1951). The value for  $\epsilon_\infty$  for water appropriate for all temperatures was taken to be 5.5. In plotting these curves, the effect of the dc conductivity on dielectric loss was assumed to be negligible. The dielectric spectrum of water at  $0^\circ$ ,  $10^\circ$  and  $20^\circ\text{C}$  and ice at  $-0.1^\circ$ ,  $-20.9^\circ$  and  $-32^\circ\text{C}$  was plotted.

Table II summarizes the reported values of the complex permittivity for ice over the electromagnetic spectrum.

### Theory of dielectric measurements

For general nonmagnetic materials where  $\mu_m = \mu_0$ , two independent experimental quantities must be found to allow the analytic calculation for the simultaneous solution of  $\epsilon'$  and  $\epsilon''$ .

The propagation constant, defined for the field quantities  $E$  or  $H$ , can be expressed as

$$\Gamma = a + j\beta$$

where  $a$  is the attenuation in nepers/m and  $\beta$  is the phase constant in radians/m. The propagation constant of a material is also written

$$\Gamma = j\omega\sqrt{\mu\epsilon_c} = j\omega\sqrt{\mu\epsilon_0\left(\frac{\epsilon_c}{\epsilon_0}\right)}$$

where  $\epsilon_c$  is the complex permittivity and is written

Table II. Reported complex permittivity of ice.

$k'$	$k''$	$f$ (or $\lambda$ )	Remarks
1.69	$5.2 \times 10^{-6}$	1 micron $\lambda$	Irvine and Pollack (1968)
1.327	$9.2 \times 10^{-2}$	10 micron $\lambda$	Irvine and Pollack (1968)
2.72	$2.6 \times 10^{-1}$	100 micron $\lambda$	Irvine and Pollack (1968)
3.05	$< 3.66 \times 10^{-3}$	3 GHz	Dunsmuir and Lamb (1945) and Lamb (1946A); measured $\tan \delta$ over 0°C to 40°C range
3.17	-	10, 24 GHz	Lamb and Turney (1949)
3.15	$< 7.6 \times 10^{-3}$	9.375 GHz	Cumming (1952)
1.91	$< 6.0 \times 10^{-2}$	35, 94 GHz	Perry and Straiton (1972); poor control over temperature and an error in phase shift calculation
3.20	$2.88 \times 10^{-3}$	3 GHz	Von Hippel (1954) reporting some of Westphal's early measurements of ice at -12°C
3.17	$2.24 \times 10^{-3}$	10 GHz	Von Hippel (1954) reporting some of Westphal's early measurements of ice at -12°C
4.80	3.84	0.1 MHz	Von Hippel (1954) reporting some of Westphal's early measurements of ice at -12°C
4.15	0.498	1.0 MHz	Von Hippel (1954) reporting some of Westphal's early measurements of ice at -12°C
3.70	0.0667	10 MHz	Von Hippel (1954) reporting some of Westphal's early measurements of ice at -12°C
4.0	-	5 MHz	Yoshino (1961); Antarctic ice core samples
3.3	-	3 GHz	Yoshino (1961); Antarctic ice core samples
2.9 to 2.95	$2 \times 10 \times 10^{-3}$ $\text{to } 4 \times 10^{-4}$	0.15 to 1.0 GHz	Ragle, Blair, and Persson (1964) reporting measurements of Westphal on ice core samples over the temperature range -1°C to -60°C
91.5	-	dc	Worz and Cole (1969); Anty and Cole (1952), T = 0.1°C

$$\epsilon_c = \epsilon' - j\epsilon''$$

and thus

$$\frac{\epsilon_c}{\epsilon_0} = \frac{\epsilon'}{\epsilon_0} - j \frac{\epsilon''}{\epsilon_0}$$

$$= k' - jk''$$

and  $\epsilon_0$  is the permittivity of free space,  $8.854 \times 10^{-12}$  farads/m. The quantity  $k'$  is referred to as the relative permittivity or the dielectric constant of the material, and  $k''$  is associated with the dielectric loss of the material and is known as the relative dielectric loss factor.

By equating these expressions for the propagation constant  $\Gamma$ ,

$$a + j\beta = j\omega \sqrt{\mu\epsilon_0(k' - jk'')}$$

then

$$(a^2 - \beta^2) + j2a\beta = -\omega^2 \mu\epsilon_0(k' - jk'')$$

and equating the real and imaginary parts gives

$$k' = \frac{\beta^2 - a^2}{\omega^2 \mu \epsilon_0} = \left( \frac{\lambda_0}{2\pi} \right)^2 (\beta^2 - a^2)$$

$$k'' = \frac{2a\beta}{\omega^2 \mu \epsilon_0} = \frac{1}{2} \left( \frac{\lambda_0}{\pi} \right)^2 a\beta.$$

Thus the complex dielectric constant may be computed from a knowledge of the measured attenuation and phase shift of the material.

A wide variety of methods are used for obtaining an independent pair of these quantities. For low frequencies one technique places the dielectric material between the parallel plates of a capacitor in a resonant circuit. From a measure of the  $Q$  of the resonant circuit with and without the dielectric material between the capacitor plates, and from a measure of the frequency shift of the circuit, one can calculate  $k'$  and  $k''$ . As the frequency of measurement increases the cavity replaces the resonant lumped-parameter circuit. Other techniques, such as standing wave measurements made in conjunction with the null shift, have been successfully employed (see, for example, Von Hippel 1954).

One approach successfully used at X-band with long (in terms of wavelength) samples is to fill a section of waveguide with the dielectric material and to compare the phase shift and attenuation through the sample with that through an empty section of guide (Straiton and Tolbert 1948, Wiebe 1971). For yet higher frequencies, where the dimensions of the guide prove too small for practical applications of this technique, the wave is propagated through a free-space path and through a section of waveguide to a detector where the signals from each path are combined (Hertel, Straiton and Tolbert 1953, Montgomery 1947, Saxton et al. 1962). The amplitude change of the signal propagated through the free-space and material sample gives information about the attenuation constant, and the null shift at the detector gives a measure of the phase shift due to the sample. This particular technique was used to make the dielectric measurements of ice at 96.5 GHz, and a more thorough discussion of this approach is deferred to a following section.

In practice, a number of material sample thicknesses are used since in general a plot of attenuation versus sample length will not be a linear function due to variations in the wave impedance as the electrical length of the sample is changed. The attenuation and phase shift factor are obtained by plotting a large number of points and taking the slope of a straight line drawn as the average of the points. That this is true can be seen from the following argument. In Appendix A it is shown that for a plane electromagnetic wave normally incident upon a three-layer dielectric, with the bounding dielectric materials having a complex propagation constant  $\Gamma_g$ , and with the inner, sandwiched layer having a complex propagation constant  $\Gamma_3$ , then the ratio of the amplitudes of the advancing components of the electromagnetic field incident upon and leaving the layered dielectric are given by

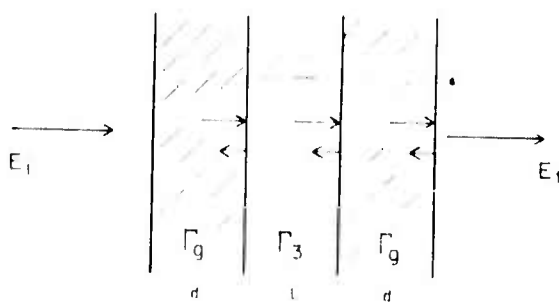
$$\frac{A_1}{A_5} = \frac{1}{16\eta_g^2\eta_3\eta_0} [(\eta_g + \eta_0)(\eta_e + \eta_g)(\eta_g + \eta_3)(\eta_0 + \eta_g) e^{(2\Gamma_g d + \Gamma_e L)} + (\eta_g + \eta_0)(\eta_3 + \eta_g)(\eta_g - \eta_3)(\eta_0 - \eta_g) e^{(\Gamma_e L)}$$

10 COMPLEX REFRACTIVE INDEX OF ICE FOG AT A RADIO WAVELENGTH OF 3 MM

$$\begin{aligned}
 & + (\eta_g + \eta_0)(\eta_3 - \eta_g)(\eta_g - \eta_3)(\eta_0 + \eta_g) e^{(2\Gamma_g d - \Gamma_3 L)} \\
 & + (\eta_g + \eta_0)(\eta_3 - \eta_g)(\eta_g + \eta_3)(\eta_0 - \eta_g) e^{-\Gamma_3 L} \\
 & + (\eta_g - \eta_0)(\eta_3 - \eta_g)(\eta_g + \eta_3)(\eta_0 + \eta_g) e^{\Gamma_3 L} \\
 & + (\eta_g - \eta_0)(\eta_3 - \eta_g)(\eta_g - \eta_3)(\eta_0 - \eta_g) e^{(-2\Gamma_g d + \Gamma_3 L)} \\
 & + (\eta_g - \eta_0)(\eta_3 + \eta_g)(\eta_g - \eta_3)(\eta_0 + \eta_g) e^{-\Gamma_3 L} \\
 & + (\eta_g - \eta_0)(\eta_3 + \eta_g)(\eta_g + \eta_3)(\eta_0 - \eta_g) e^{(-2\Gamma_g d - \Gamma_3 L)}
 \end{aligned}$$

- where  $\eta_0$  = intrinsic impedance of free space ( $\sqrt{\mu_0/\epsilon_0}$ )
- $\eta_g$  = impedance of bounding dielectric slabs
- $\eta_3$  = impedance of middle dielectric layer
- $\Gamma_g$  = complex propagation constant of bounding dielectric slabs
- $\Gamma_3$  = complex propagation constant of middle dielectric layer
- $d, L$  = layer thicknesses as defined in the sketch
- $A_1, A_5$  = amplitude coefficients of the advancing waves in media 1 and 5.

Figure 2 is a sketch of this layered dielectric.



For ice no "holding" dielectric slabs are necessary. Therefore,  $\eta_g = \eta_0$  and  $d = 0$  and the expression  $A_1/A_5$  collapses to

$$\frac{A_1}{A_5} = \frac{1}{4\eta_0\eta_d} [(\eta_d + \eta_0)^2 e^{-\Gamma_d L} - (\eta_0 - \eta_d)^2 e^{-\Gamma_d L}]$$

where  $\Gamma_d$  = propagation constant of the dielectric

$\eta_d$  = intrinsic wave impedance of the dielectric.

Since for a low loss dielectric  $\Gamma_d = j\beta_d$ , then

$$\frac{A_1}{A_5} = \frac{1}{4\eta_0\eta_d} [4\eta_0\eta_d \cos(\beta_d L) + j2(\eta_0^2 + \eta_d^2) \sin(\beta_d L)].$$

Let  $B e^{j\phi} = 4\eta_0\eta_d \cos(\beta_d L) + j2(\eta_0^2 + \eta_d^2) \sin(\beta_d L).$

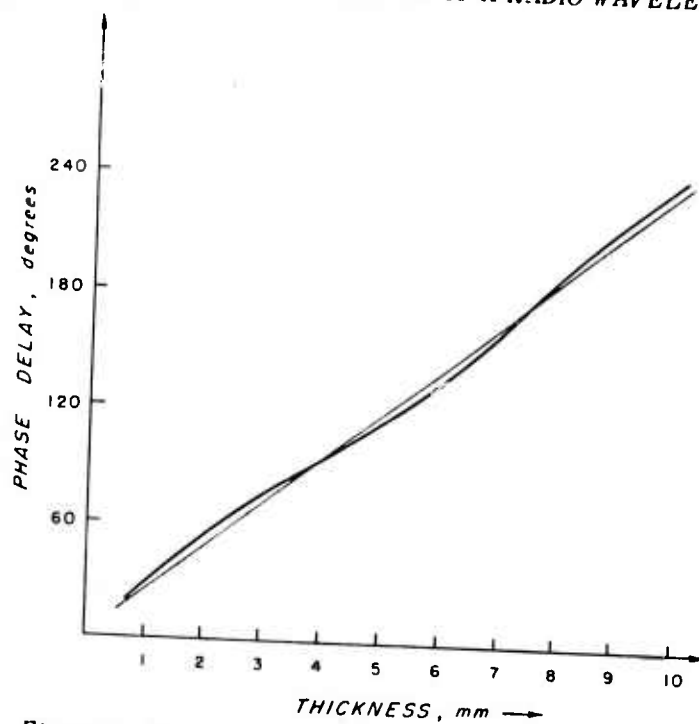


Figure 3. Phase relative delay as a function of dielectric thickness.

Thus

$$\tan \phi = \left( \frac{\eta_0^2 + \eta_d^2}{2\eta_0\eta_d} \right) \tan (\beta_d L)$$

and so

$$\frac{A_1}{A_3} = \frac{\beta e^{i\phi}}{4\eta_0\eta_d}$$

and the advancing component in medium 3 can be written as

$$E = A_3 e^{-j\beta(L+z)}$$

$$E = \frac{A_1 4\eta_0\eta_d}{B} e^{-i\phi} e^{-j\beta_1(L+z)}$$

where  $\phi$  is the phase delay due to the dielectric.  $\phi$  is not a linear function of  $L$ , as can be seen in Figure 3, which is a plot of the transcendental expression for  $\phi$  given above. Thus a measured plot of  $\alpha$  and  $\phi$ , in nepers/m and radians/m, respectively, will not be a linear function, but rather a slowly varying sinusoidal function about a straight line drawn as the average of the points. This is indeed the way that the observational data look. The effect of a material dielectric loss is to damp out this sinusoidal variation with increasing material thickness  $L$ . The maximum variation of the relative phase above or below the straight line fit of Figure 3 is about  $10^\circ$ , or nearly 0.028

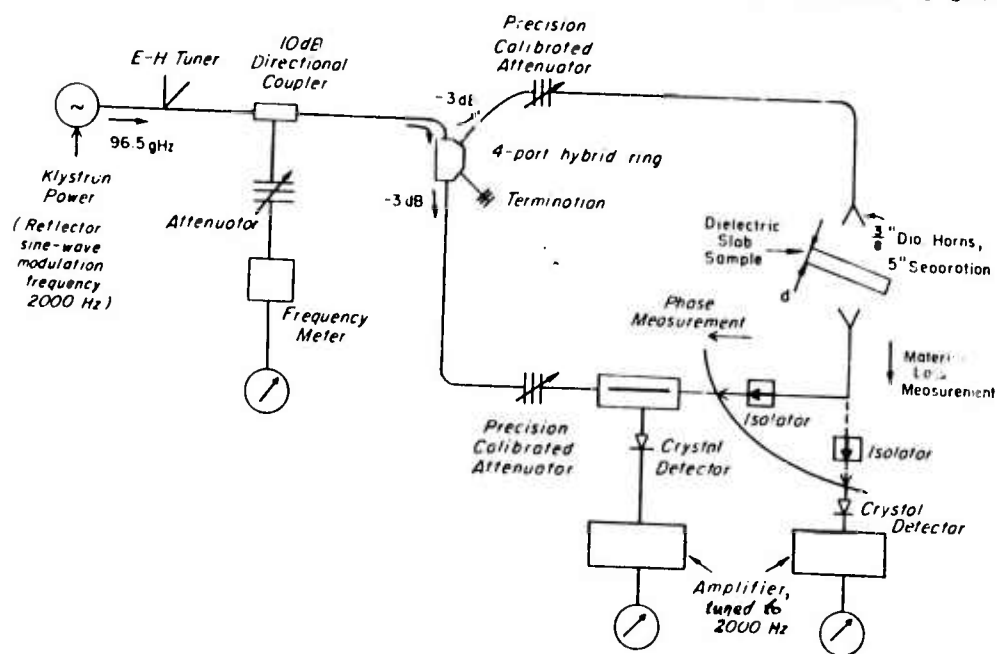


Figure 4. Quasi-optical free-space method of measuring complex permittivity,  $\epsilon'$  and  $\epsilon''$ .

wavelength. This is in agreement with the measured data for ice, which vary from 0.02 to about 0.06 wavelength above and below the straight line fit.

#### Instrumentation for ice dielectric measurements

For practical reasons, the best technique for making complex dielectric constant measurements at 96.5 GHz involves measuring the amplitude and phase change of a signal propagated through a free-space path containing varying thicknesses of the dielectric material. With this technique, a millimeter wave signal from a klystron source is split by a -3 dB coupler and travels over two waveguide propagation paths. Each path contains an attenuator, but only the attenuator in the path containing the dielectric sample between the two horns must be a precision attenuator. After passing over these two paths, the signals are recombined in a standing wave pattern in a section of precision slotted line. Figure 4 indicates this experimental measurement technique. The isolator is to prevent reflections from reentering the waveguide and causing anomalous phase and amplitude changes. In practice, the sample material is tilted at a very small angle to aid in eliminating these reflection effects.

The horns are made of electroformed copper, with an opening of about  $\frac{3}{8}$  in. The minimum horn separation distance is set by the Fraunhofer far field criterion,  $d = 2\lambda D_\lambda^2$ , where  $D_\lambda$  is the aperture opening in wavelengths and  $\lambda$  is the operating wavelength.

The system is initially balanced by removing the slotted line section and adjusting the attenuators for equal signal levels over each path. For phase measurements, the attenuators are not touched again, since it was discovered that changing the attenuator setting by several dB would shift the phase a small amount. The degree of balance was indicated by the sharpness of the null in the standing wave pattern. However, a high degree of balance is not really required, since the detection system was sensitive enough to follow a null shift even when more than 6 dB of imbalance existed. For ice and polystyrene, both low loss dielectrics, the signal loss, even through the thickest ice samples used, was under 2 dB. The measurements with water presented the greatest problem. The details of how this measurement was accomplished are delayed to a later section, but

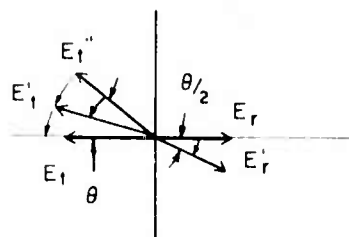


Figure 5. Phase relationship of transmitted and reference fields in the slotted line section for the null condition.

for water samples less than about 0.010 in. thick satisfactory attenuation and phase measurements were made.

For attenuation measurements, propagation only over the free space path is important. A power detector was mounted on the receiving horn, and the attenuation measurements were accomplished in either one of two ways. For moderate and high loss dielectrics, the dB change in the precision attenuator setting necessary to restore the same power level at the detector with the dielectric in the path as was present without the dielectric is a measure of the dielectric loss. For low loss dielectrics, where a change in the precision attenuator setting is hard to read, the dielectric loss was calculated from the change in the output meter reading on the high-gain tuned amplifier. This amplifier was

checked against various dB settings of the precision attenuator, and its output meter reading was very linear in power, thus indicating that the crystal detector was operating in its square-law region. With several hours warm-up, both the klystron and this amplifier proved to be quite stable, and over the course of the measurements the output level returned to its initial value on the output meter with the initial (reference) precision attenuator setting and no dielectric in the path.

To make phase shift measurements, each propagation path is connected up to one side of the slotted line section after having been balanced as well as possible, as described earlier. The probe in the slotted line section is adjusted for minimum penetration depth consistent with a workable signal level. This assures a minimum perturbation of the fields within the waveguide. With no dielectric material in the path, the probe position is adjusted for a null in the standing wave pattern. A dielectric sheet placed in this free space path causes this null to shift in position, and the amount of shift, in hundredths of a millimeter, can be read by the gauge attached to the carriage of the slotted line. This null shift, in millimeters or fractions thereof, can then be put in terms of fractional parts of a wavelength shift and plotted as a function of dielectric thickness, as is usually done.

With a slotted line technique of making phase measurements, the measured phase shift is actually half the true phase shift. Let  $E_r$  and  $E_t$  be the reference and the transmitted  $E$ -field vectors in the slotted line at the probe for no dielectric in the free-space path and for the probe positioned at a null in the field. With the introduction of the dielectric slab in the free-space path, the phase of the transmitted wave shifts  $E_t$  to  $E_t'$  (see Fig. 5) by an amount  $\theta$ . To reestablish a null, the probe is re-adjusted to shift the phase by  $\theta/2$ , since in moving  $E_t'$  to  $E_t''$  through an angle  $\theta/2$ ,  $E_r$  is moved  $\theta/2$  in the opposite direction to  $E_r'$ , thus making  $E_r'$  and  $E_t''$  again 180 degrees out of phase with each other.

For all dielectric measurements made, the klystron repeller was modulated at 2 kHz, and the high-gain amplifier used after the detector was sharply tuned to 2 kHz. This procedure is usually followed to avoid the problems of flicker noise (if noise) and drift associated with a high gain dc amplifier. There is no special reason to choose a 2-kHz modulation frequency, but in general the modulation frequency should be chosen to avoid the 60-Hz line frequency and its harmonics.

#### Calibrations with polystyrene and water samples

In order to establish the accuracy and to become familiar with this dielectric measurement technique, dielectric measurements were made on polystyrene and water prior to the ice measurements. The measurements were all made at room temperature.

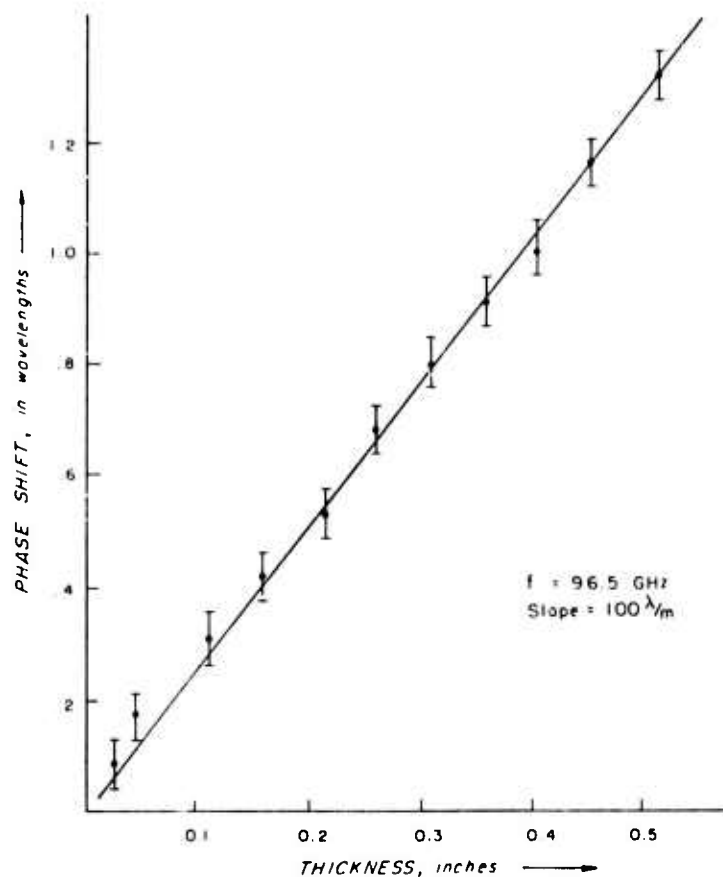


Figure 6. Polystyrene phase shift curve.

*Polystyrene.* Slabs of polystyrene were made by machining disks from a 2-in.-diam polystyrene rod. Eleven such disks were machined in thicknesses from 0.025 in. to over 0.5 in. Figure 6 is a plot of the phase shift curve for the polystyrene samples. The error bars were set by the uncertainty in measuring the null shift with the slotted line and in the variations of the observed data points from repeated measurements. Figure 7 is the attenuation curve measured for this polystyrene sample set. The error in these data is about  $\pm 0.1$  dB. This inaccuracy arises principally due to changes in the tilt angle of the dielectric slabs. Since it was impossible to orient the samples exactly the same each time, many repeated measurements were made to average out this effect.

Polystyrene was chosen for calibration purposes since its complex dielectric constant is well known and, except for its dielectric loss, essentially constant (*ITT Reference Data for Radio Engineers Handbook*, 1970). The measured and published complex dielectric constants for this material are given in Table III.

*Water.* Water was chosen for measurement purposes because its behavior is well described by the Debye expressions. In addition, measurements have been made of the complex dielectric constant at millimeter wave frequencies and reported in the literature (Zolotarev et al. 1969, Chamberlain et al. 1966, Collie et al. 1948 and Lane and Saxton 1952).

Water is a particularly difficult material to work with. Because of its great dielectric loss at this frequency (96.5 GHz) it is practical to make measurements only on very thin layers. It was determined that the upper limit to the water thickness was about 0.010 in. This limit is clearly set

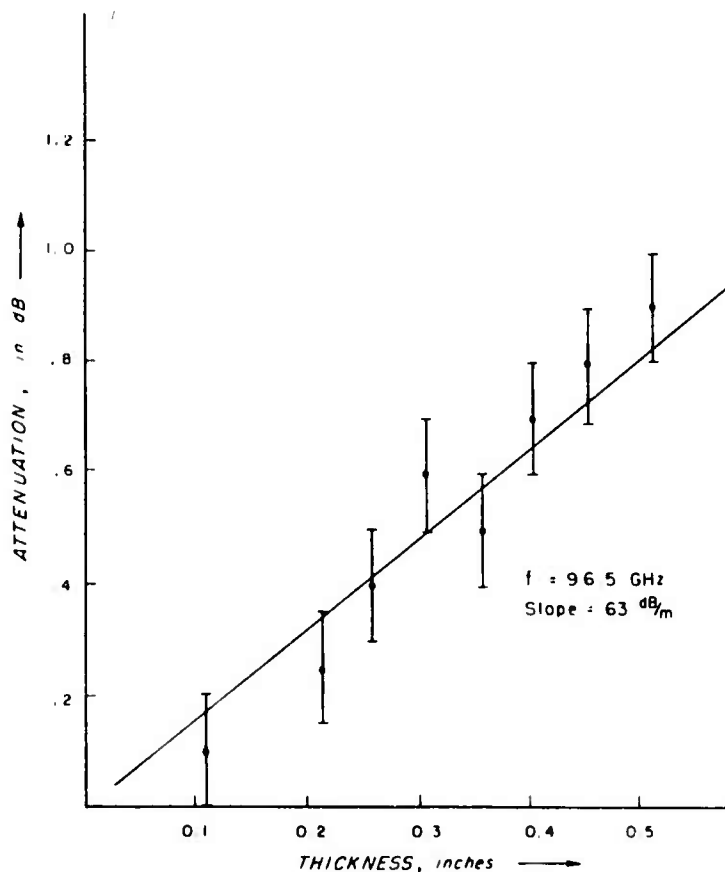


Figure 7. Polystyrene attenuation curve.

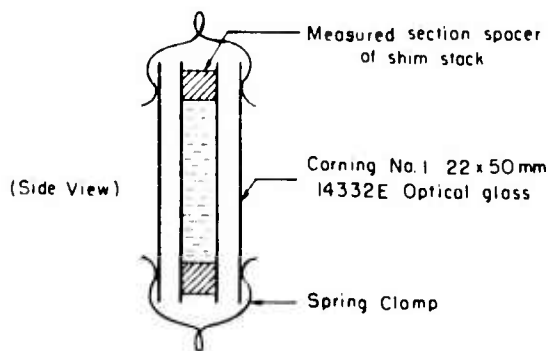


Figure 8. Holder arrangement for water samples.

by the available klystron power which in this case is about 100 mW, and which suffers about a 4-dB loss in just getting to the horns. Varying thicknesses of water were obtained by using two pieces of very thin slide glass separated by pieces of shim stock of a known thickness. A thin pipette was used to place the liquid between the bounding glass layers. Capillary action then drew the water into the enclosed space. Figure 8 diagrams this arrangement. With this arrangement, the slotted line was adjusted for a null with the holder present in the propagation path but with no water present. The null shift caused by the addition of water to the holder was then plotted as a function of water thickness.

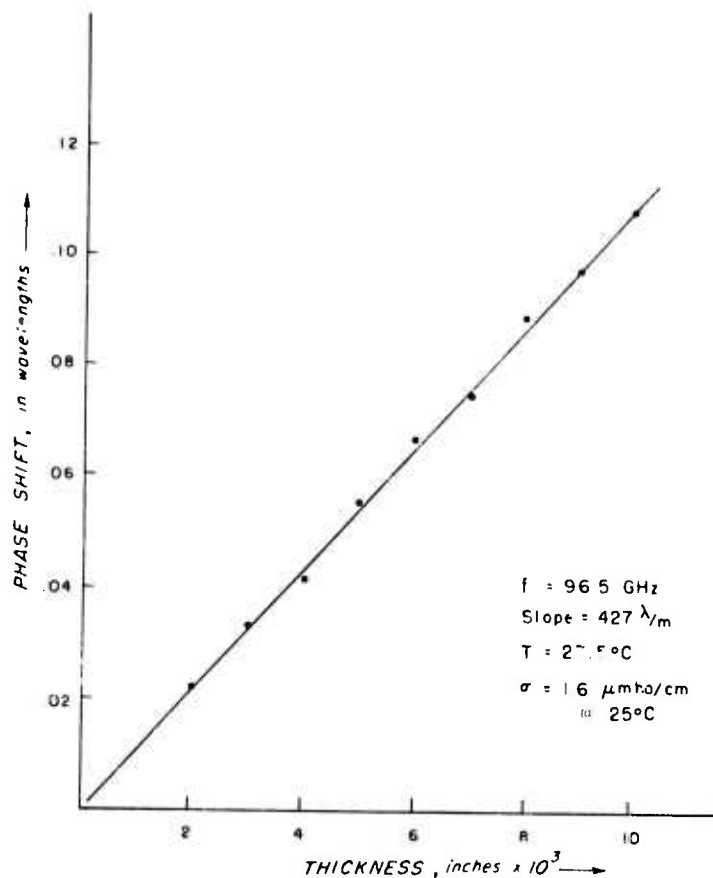


Figure 9. Phase shift curve for distilled water.

Attenuation measurements were made in essentially the same manner, that is, the signal level was recorded with and without water in the holder.

Figures 9 and 10 are two phase shift curves of distilled water and lake water, respectively. The measured dc conductivity of these two water samples was  $1.6 \mu\text{mho/cm}$  at  $25^\circ\text{C}$  and  $565 \mu\text{mho/cm}$  at  $25^\circ\text{C}$ , respectively. Figures 11-13 give the attenuation curves for distilled water, rainwater and lake water. The rainwater sample had a measured conductivity of  $33.6 \mu\text{mho/cm}$  at  $25^\circ\text{C}$ , but this sample was lost before a phase shift curve for it could be obtained.

Considering the practical problems involved in working with thin water samples, the agreement is surprisingly good between these measurements and values published in the literature. The major sources of error in this work were in determining the water thickness accurately and in reading the "bottom" of the null shift when water was introduced in the holder. The nulls tended to be somewhat flat, especially for thicknesses greater than about 0.006 in. In this case, the average value of two points of equal response on either side of the null was taken to be the true null point. The error bars shown in the following figures were found by assuming the measurement errors were essentially random, and thus the error shown is  $\sigma_i/\sqrt{N}$ , where  $\sigma_i$  refers to the error associated with an individual measurement and  $N$  is the number of individual measurements made for a given sample thickness.

Table III gives the complex permittivity values for polystyrene and water as derived from these measurements. The values of the appropriate published data are also listed for comparison purposes.

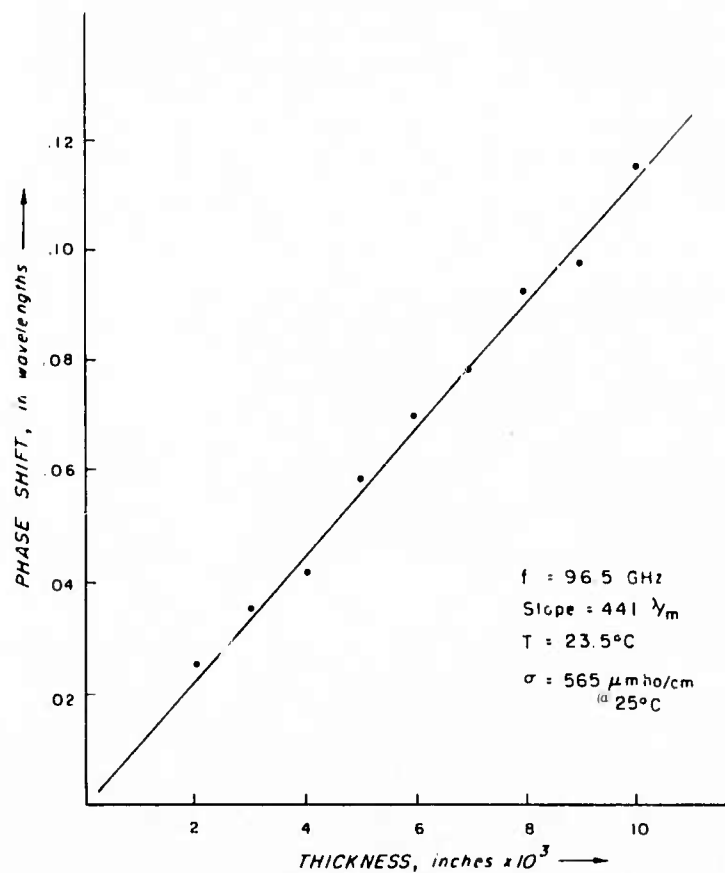


Figure 10. Phase shift curve for lake water.

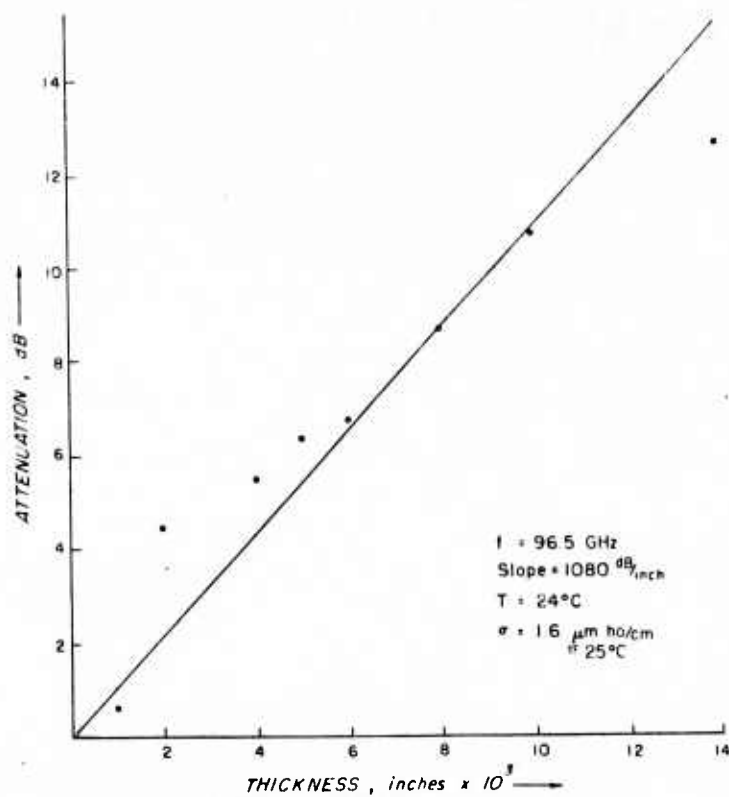


Figure 11. Attenuation curve for distilled water.

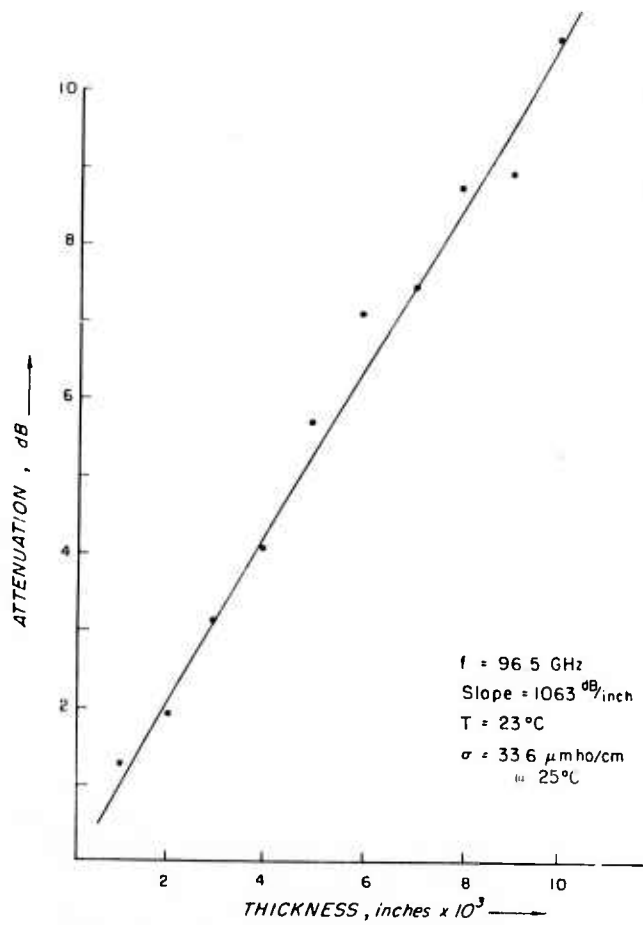


Figure 12. Attenuation curve for rain water.

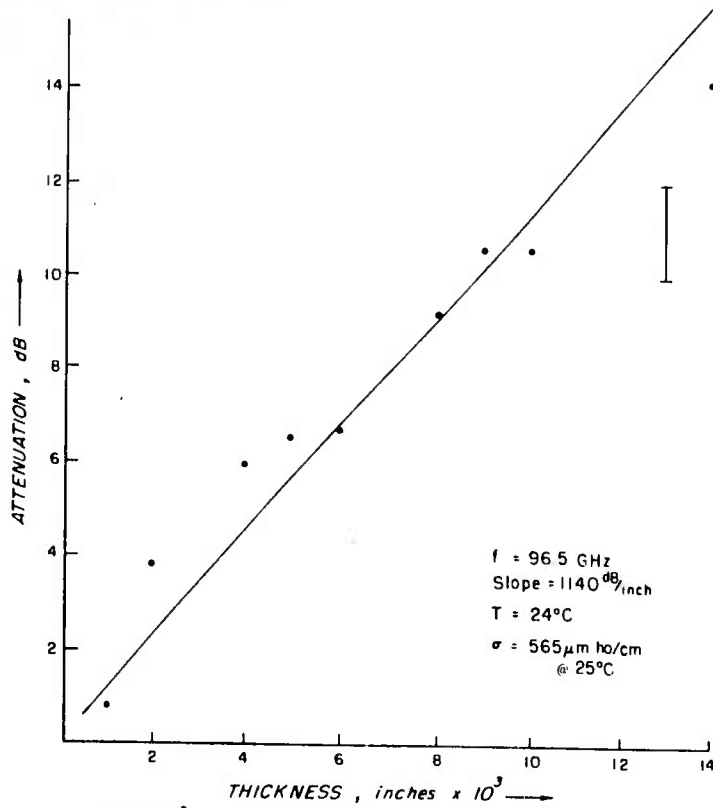


Figure 13. Attenuation curve for lake water.

Table III. Complex permittivity of polystyrene and water samples at 96.5 GHz.

Material	$\beta$ (rad/m)	$\alpha$ (nepers/m)	$k'$	$k''(10^3)$	Remarks
Polystyrene	3275 $\pm$ 55	7.25 $\pm$ 1.35	2.63 $\pm$ .09	11.74 $\pm$ 2.46	Perry, U.T., 1973
Distilled de-ionized water	7390 $\pm$ 1000	4900 $\pm$ 900	7.5 $\pm$ 1.54	17.9 $\pm$ 6.2	Perry, U.T., 1973; $\sigma = 1.6 \mu\text{mho/cm}$ at 25°C
Lake water	7740 $\pm$ 1000	5160 $\pm$ 900	8.45 $\pm$ 1.5	19.8 $\pm$ 6	Perry, U.T., 1973; $\sigma = 565 \mu\text{mho/cm}$ at 25°C
Rain water	—	4810 $\pm$ 300	—	—	Perry, U.T., 1973; $\sigma = 33.6 \mu\text{mho/cm}$ at 25°C
Polystyrene	—	—	2.54	3.05	Ref Data Radio Engrs (IT&T), for 25 GHz
Polystyrene	—	—	2.55	0.842	Ref Data Radio Engrs (IT&T), for 3 GHz
Polystyrene	—	—	3.4	5.78	Pate (1967), 94 GHz
"Pure" water	—	—	9.33	16.3	Calculated from Debye equations
Water	—	—	19.2	29.1	Collie et al. at 1.25 cm
Water	—	—	$n^2 = 4.44 \pm .08$	—	Chamberlain et al., $\lambda = .3$ mm
Water	—	—	$n^2 = 4.30 \pm .08$	—	Chamberlain et al., $\lambda = 0.118$ mm
Water	—	—	$n = 3.55$	—	Zolotarev et al., $\lambda = 3.1$ mm
Water	—	—	13	23	Lane and Saxton, $\lambda = 6.2$ mm at 20°C
Water	—	—	7.84	14.1	Lane and Saxton, $\lambda = 6.2$ mm at 0°C

Since the measured  $\beta$  is the difference between the phase shift in 1 m of air and 1 m of the sample, then the true  $\beta_d$  is obtained by adding  $2\pi/\lambda_0$ , or 2020 rad/m, to twice the measured  $\beta$ . It is this value that is given in Table III.

The values for  $k'$  and  $k''$  measured here for polystyrene agree well with the published values for this material. Water is well described by a Debye expression for the complex permittivity, at least in this part of the millimeter wave spectrum. The values of  $k'$  and  $k''$  measured for distilled, deionized water agree well with the Debye predictions, and are close to other reported measurements in the millimeter wave spectrum. From these measurements it appears that the water samples with the higher amounts of impurity had a slightly higher dielectric loss and dielectric constant. However, the error bars are overlapping, so one cannot draw any strong conclusions.

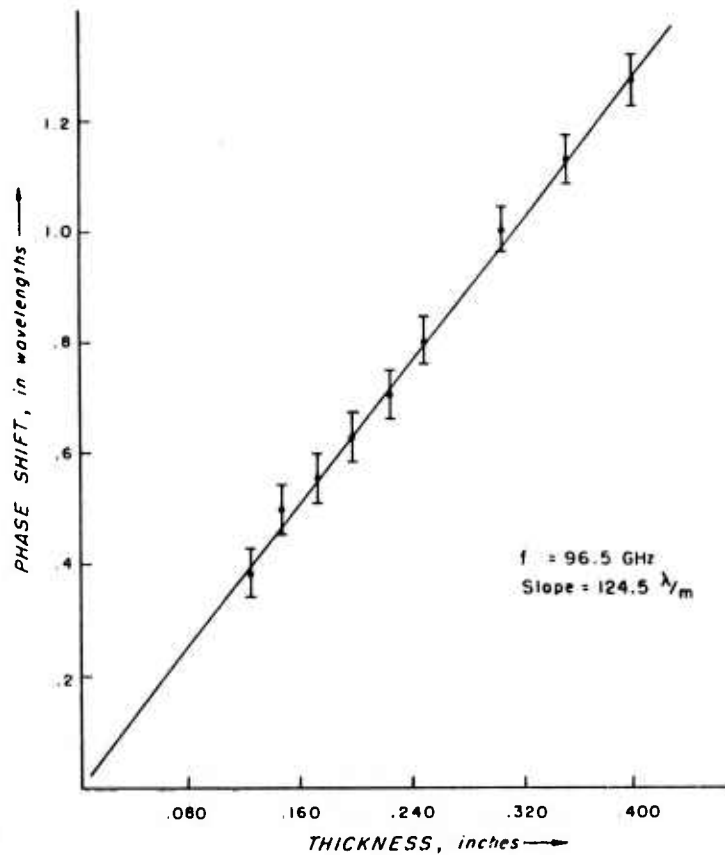


Figure 14. Phase shift curve, ice made from distilled water,  $T = -28^{\circ}\text{C}$ .

#### Results for ice

The ice samples used in making these measurements were prepared from two different water samples: lake water and distilled, deionized water. These water samples had the measured dc conductivities given in the previous section. All ice samples were prepared in specially machined aluminum holders of prescribed thickness. Once the samples were frozen, the holder sides could be removed to release them. Ice samples were made in thicknesses from 0.125 to 0.404 in. The advantage of preparing ice in this manner is that the frozen samples had flat, parallel sides. In order to make ice samples as free from internal stress cracks as possible, freezing was accomplished in two stages. The water was slowly frozen over a 12-hour period at about  $-1^{\circ}\text{C}$ , then transferred to the environmental chamber where it was chilled down to about  $-28^{\circ}\text{C}$  before the dielectric measurements were made.

Waveguide was run through the walls of the environmental chamber to the interior horn antennas where all measurements were made.

Several individual sets of measurements were made with ice prepared from each type of water. Figures 14-17 are representative of the phase shift curves obtained in this manner. The measured phase shifts varied between about 118 and 128.5 wavelengths/m. This phase shift is just half the true phase shift, as explained earlier. The ice made from the lower impurity level water showed a lower average phase shift (about 121.3 wavelengths/m), compared with about 129 wavelengths/m for the other ice samples. Figures 18 and 19 are attenuation curves for these ice types. All of these ice samples proved to be rather sensitive to the orientation angle, and it was necessary to

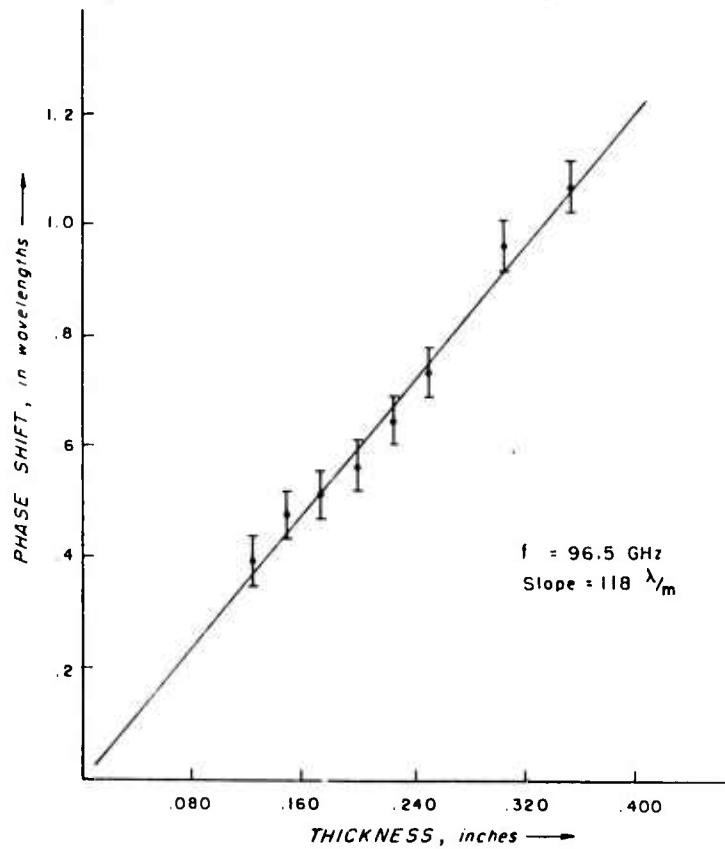


Figure 15. Phase shift curve, ice made from distilled water,  $T = -28^\circ\text{C}$ .

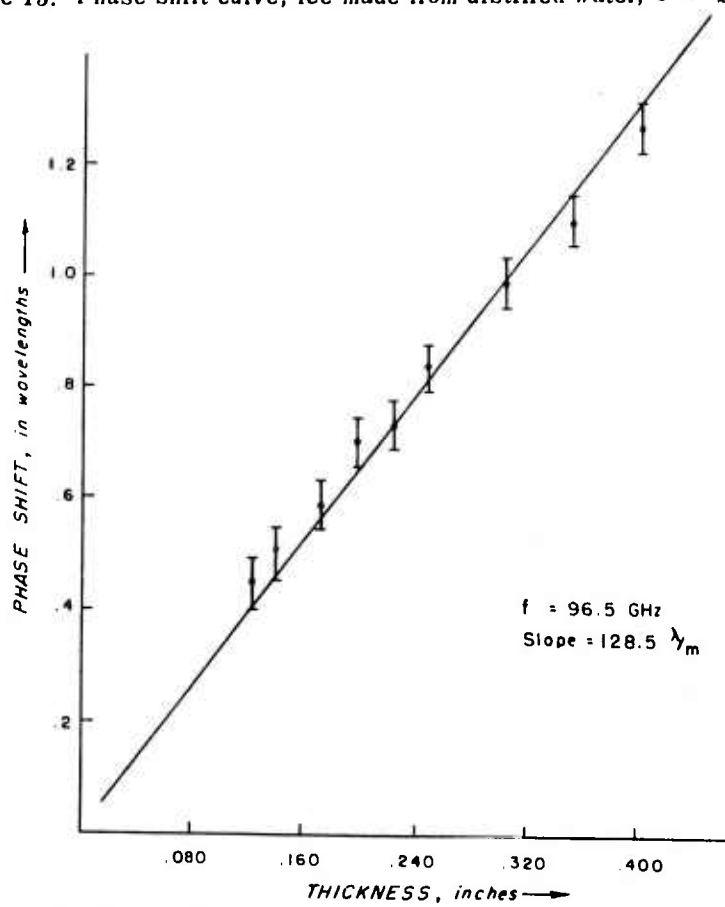


Figure 16. Phase shift curve, ice made from lake water,  $T = -28.5^\circ\text{C}$ .

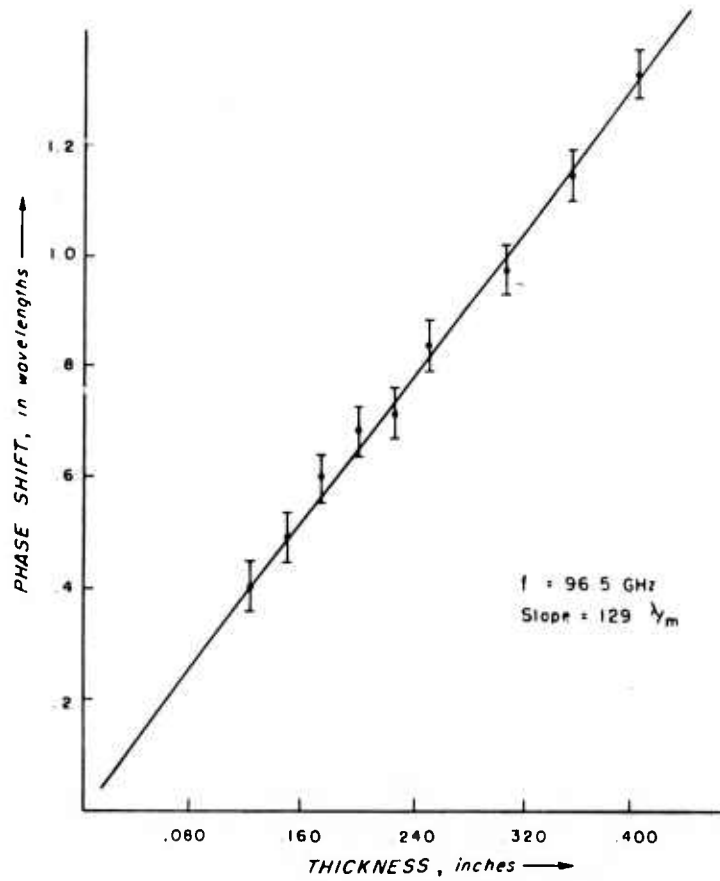


Figure 17. Phase shift curve, ice made from lake water,  $T = -30.5^\circ\text{C}$ .

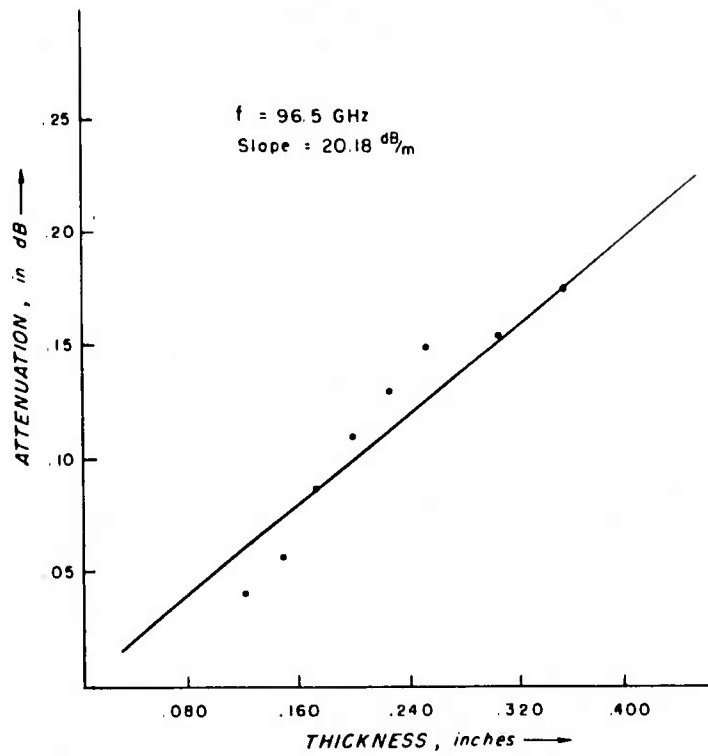


Figure 18. Attenuation curve, ice made from distilled water,  $T = -28^\circ\text{C}$ .

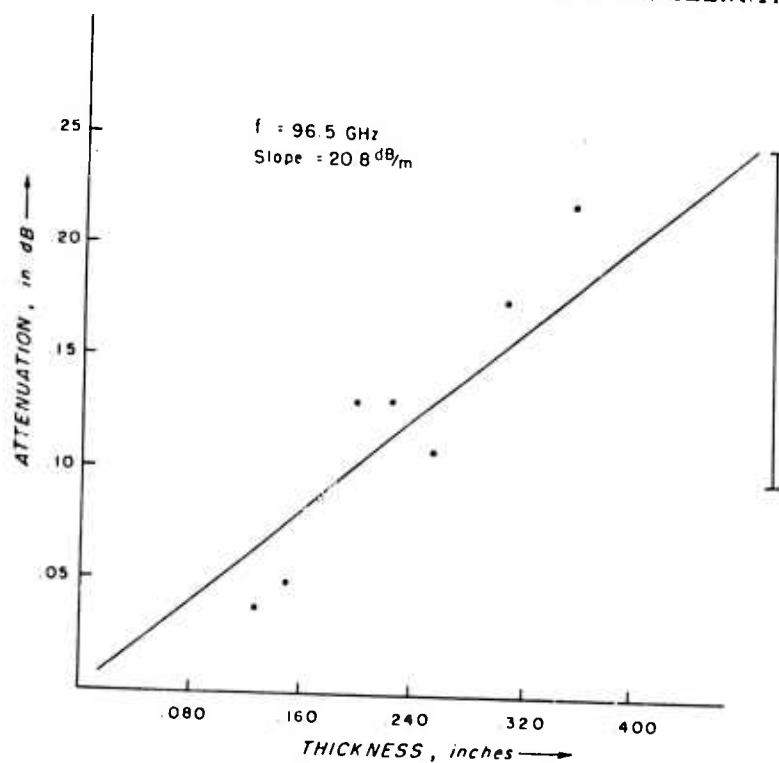


Figure 19. Attenuation curve, ice made from lake water,  $T = -28.5^\circ\text{C}$ .

Table IV. Measured complex permittivity of ice at 96.5 GHz.

$\alpha$ (nepers/m)	$\beta$ (rad/m)	$k'$	$k''(\times 10^3)$	Remarks
$2.27 \pm 0.8$	$3545 \pm 120$	$3.08 \pm 0.2$	$3.99 \pm 1.50$	Distilled, deionized water sample $-28^\circ\text{C} \leq T \leq -29^\circ\text{C}$
$2.32 \pm 0.8$	$3635 \pm 120$	$3.24 \pm 0.2$	$4.17 \pm 1.60$	Lake water sample $-28.5^\circ\text{C} \leq T \leq -31^\circ\text{C}$

average over many data points to obtain consistent results. The error bars shown apply to all points, and while the points plotted are the average of at least ten different measurements, the error bars are indicative of the uncertainty in the individual ice sample measurements. The possible error associated with the individual loss measurements was less than  $\pm 0.1$  dB. The attenuation, in dB, was calculated from relative changes in output meter level, and not changes in the precision attenuator setting.

Table IV gives the results obtained from these ice sample measurements. The  $\beta$  appearing in this table is twice the measured phase shift, in rad/m, plus the phase shift of free space,  $2\pi/\lambda_0$ .

### III. THE METEOROLOGY OF ICE FOG

#### Introduction

Fog is a common arctic sight. Polar ocean meteorological stations report a frequency of 100 days per year of fog occurrences, and Greenland coastal reporting stations observe 50 to 60 days a year of fog occurrence (Orvig 1970). Summer fogs in the Arctic are generally caused by advection of relatively warm and moist air over melting ice or cold water. This fog is patchy and of short duration, and does not occur for wind speeds over 10 m/sec. During winter, steam fog forms over open water leads in the ice pack where the sea water may be near 0°C and the air temperature may be at -40°C, thus setting up a strong thermal gradient over a relatively short distance. Such a fog is generally known as an ice fog since it is composed largely of minute ice crystals. This fog, also known as "arctic sea smoke," develops when very cold air flows over open ocean, causing a rapid discharge of moisture and heat to the air.

One of the principal requirements for fog formation is the existence of a stable atmospheric condition. It is well known that the most stable atmospheric conditions occur under and within temperature inversions. There are three main causes of temperature inversions.

1. When a warm air mass flows over a cooler surface, a temperature inversion may form in the boundary layer between the two. Here, the temperature is relatively constant from the ground up to the boundary layer, then increases sharply upon entering the upper air mass. This type of inversion is responsible for entrapment and intensification of the infamous Los Angeles smog.
2. When there is a net loss of energy from the earth's surface (by outgoing long wave radiation) a temperature inversion forms at ground level. These inversions become especially well developed over snow and ice surfaces and are quite common both day and night in the Arctic and Antarctic.
3. Subsidence is generally associated with high pressure areas where there is a descent and warming of deep layers of air. This effect causes a decreasing of the temperature gradient and is a frequent cause of temperature inversions of the lower troposphere.

The type of inversion described by 2. is especially common in the Fairbanks area, and has been responsible for producing some of the strongest temperature gradients in the world, with values of 10° to 30°/100 m (Benson 1965, 1970). These inversions rarely extend over 50 or 100 m in height, but within this ground-based inversion layer dense ice fog can form. Not only are these some of the severest inversions known, but they are also the most persistent, sometimes lasting for weeks at a time (Ball 1959, Benson 1965, 1970). Surface winds within these inversions are ideal nurseries for the development and intensification of ice fogs where conditions are right for their production.

Ice fog is not restricted to coastal and ice pack areas, and commonly occurs as an inland form of low-temperature air pollution. Aside from local sources of water vapor in an inland area such as hot springs and caribou herds, ice fog is restricted to populated areas. It is produced by the water vapor output from automobile exhausts, power plant stacks, household chimneys, cooling water discharge areas of electric generating plants, and other sources associated with urban development. Since air pollution, i.e. the presence of unwanted material in the air, varies in specific detail from one locality to the next, ice fog can qualify as an air pollution material in the Fairbanks Ft. Wainwright area of interior Alaska. For this reason this literature, which treats ice fog as a low temperature form of air pollution, has been consulted for details concerning ice fog crystal measurements and the mechanisms for ice fog formation.

In arctic and subarctic regions where sufficient volumes of moisture or open water exist, and where temperatures go down to about  $-30^{\circ}\text{C}$ , a fog composed of minute ice crystals appears. Because of its close association to human activities (such as automobiles, home heating, power plant exhausts) as well as its obvious adverse effects on traffic and airport visibility, Oliver and Oliver (1949) suggested that ice fog be studied as an air pollution problem. Accordingly, Robinson et al. (1955), Benson (1965, 1970) and Ohtake (1970) have shown that ice fog does qualify as a low temperature form of air pollution and have published detailed characteristics of the ice fog particles and of the meteorological conditions occurring during ice fog events.

#### **Physical distinguishing characteristics and optical properties**

The optical properties and ice crystal types occurring in an ice fog are different from those of other concentrations of ice crystals in the atmosphere such as cirrus clouds or "diamond dust" displays. Ice crystals which have well formed hexagonal plates and columns are called "diamond dust" because of the way they twinkle under a low sun or nighttime illumination. "Diamond dust" ice crystals in the atmosphere are responsible for the interesting halo effects sometimes seen when cirrostratus clouds come between the observer and the sun or moon. This halo takes the form of a bright ring having a radius of about 22 degrees, and besides this halo there may be numbers of "light-bows" and concentrations of light in spots, each with a name of its own, which combine to form the halo phenomena. Minnaert (1954) describes in detail each of these halo phenomena, as well as the physical cause underlying the display. All clouds giving rise to halos are composed of small ice crystals, and the regularity of the shapes of these crystals is responsible for the beautiful symmetry of the light phenomena. The small halo phenomenon is caused by ice crystals in the shape of a prism, with the crystals generally between 30 and 300  $\mu$  in diameter. Vertical pillars of light, appearing at night above automobile headlights, and above and below the rising or setting sun, are caused by ice flakes inclined nearly to the horizontal in the air. Crosses, halos, light pillars, double suns, and parhelia or mock suns at the same altitude as the sun are all optical phenomena associated with the passage of light through ensembles of geometrically configured euhedral crystals. However, halo effects are entirely absent in ice fogs. The optical properties of an ice fog are similar to those of a water droplet fog, yet water droplets are not present in ice fogs (Robinson, Thuman and Wiggins 1957). In addition, visibility is much lower in an ice fog than in a "diamond dust" shower. These differences are explainable in terms of the crystal sizes involved. Smaller particles tend to have a more pronounced scattering effect than larger particles. The similarity in the optical properties of ice fogs and liquid water droplet fogs is shown by Kumai and Russell (1969). This optical similarity between water and ice fogs is due to their optical values of the complex index of refraction, which are very nearly the same. They calculated the extinction coefficients of both water and ice spheres (for an assumed particle density distribution) at wavelengths of 2.2, 2.7, 4.5, 5.75, 9.7 and 10.9 microns. The attenuation coefficients and backscattering functions of ice fog and water fog were within the same order of magnitude for the same fog concentrations and wavelengths. Recent measurements of laser extinction in an ice fog were made by Munis and Delaney (1972). They made measurements of laser extinction at 0.6382, 1.15 and 3.39 microns, and compared these measurements with the theoretically calculated values given by the Mie extinction coefficients for the measured particle distributions involved. In general, the measured extinction coefficients were within about a factor of 5 of the Mie extinction coefficients, with the best agreement between theory and experimental measurements being at 1.15 microns. Their experimental finds at 0.6328  $\mu$  are of special interest to this research work in that a helium-neon laser, operating at this same wavelength, was used to obtain additional insight into the fog statistics.

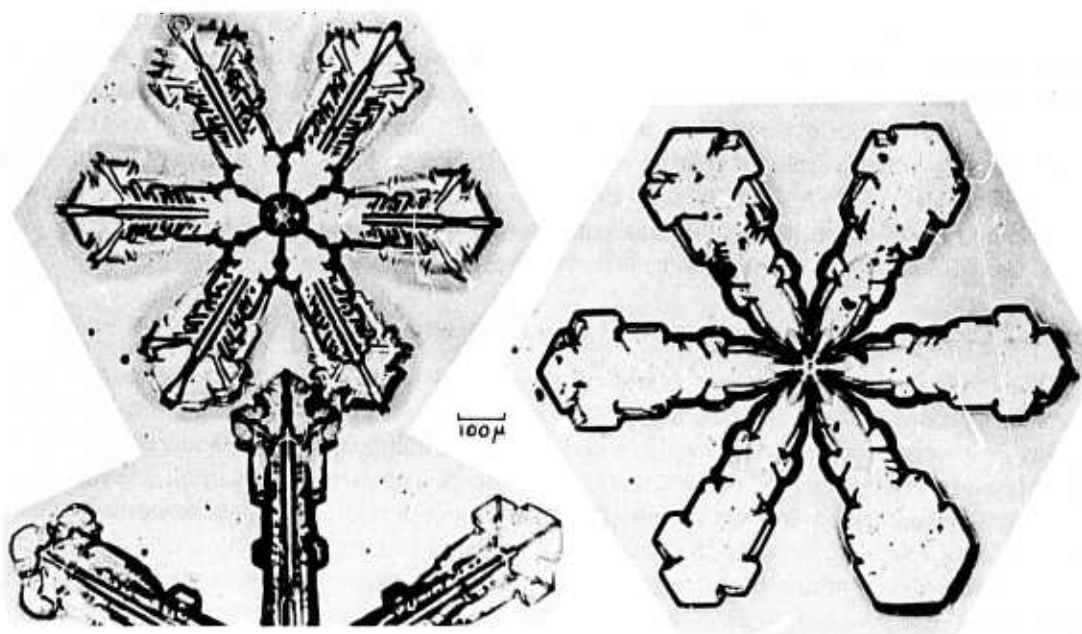


Figure 20. Small (1 mm) snow crystals.

#### Ice fog crystal size and formation

Ice fog crystals range between 2 and 20  $\mu$  in diameter (Robinson, Thuman and Wiggins 1957, Kumai 1964). Ice crystals larger than 30  $\mu$  can occur, and in general they are more euhedral. Many of the small crystals tend to lack a definite crystalline form. Because of this Thuman and Robinson (1954) coined the term *droxtal* in reference to these ice fog particles. According to them, a droxtal is a small, poorly formed ice crystal. It is an equant solid particle with rudimentary crystal faces which seems to have the characteristics of both droplets and crystals. The term *droxtal* appearing in the literature does not mean that ice fog particles are not crystals. When a supercooled droplet freezes, it becomes crystalline ice regardless of its shape and the presence or absence of any crystalline faces. There has been no evidence of amorphous ice existing in ice fog particles. This is not to say that only poorly defined geometric forms exist for ice fog particles. Ohtake (1970) has found 14- and 20-face polyhedral crystals in ice fog at  $-47^{\circ}\text{C}$ , although it is true that the vast majority of the droxtals are "spherical" ice crystals.

Figures 20-22, from Benson's (1965) report, show the difference between small 1-mm snow crystals, diamond dust crystals (from 1 to about 300  $\mu$  in diameter), and ice fog crystals with diameters of 25  $\mu$  or less. In general, ice fog particles are an order of magnitude smaller than diamond dust crystals which in turn are an order of magnitude smaller than snow crystals. The differences in size and shape of the ice fog droxtals and the cirrus cloud or diamond dust crystals are due to the different rates of cooling and growth. Gotaas and Benson (1965) measured cooling rates as high as  $4^{\circ}\text{C}$  per 12-hour period for the arctic free atmosphere, with typical cooling rates on the order of one-half to one-third this value. However, such low cooling rates in a very low temperature environment cause water vapor to precipitate out of clear air (the typical diamond dust shower) in the form of well developed large crystals. Where the atmosphere and the water vapor contained in it cool simultaneously the ice crystals formed grow in a saturated air volume as long as the cooling continues. The size of the crystals increases with both the original moisture content of the air and the length of the cooling period involved, the ultimate result being a snowstorm containing large and well formed ice crystals.

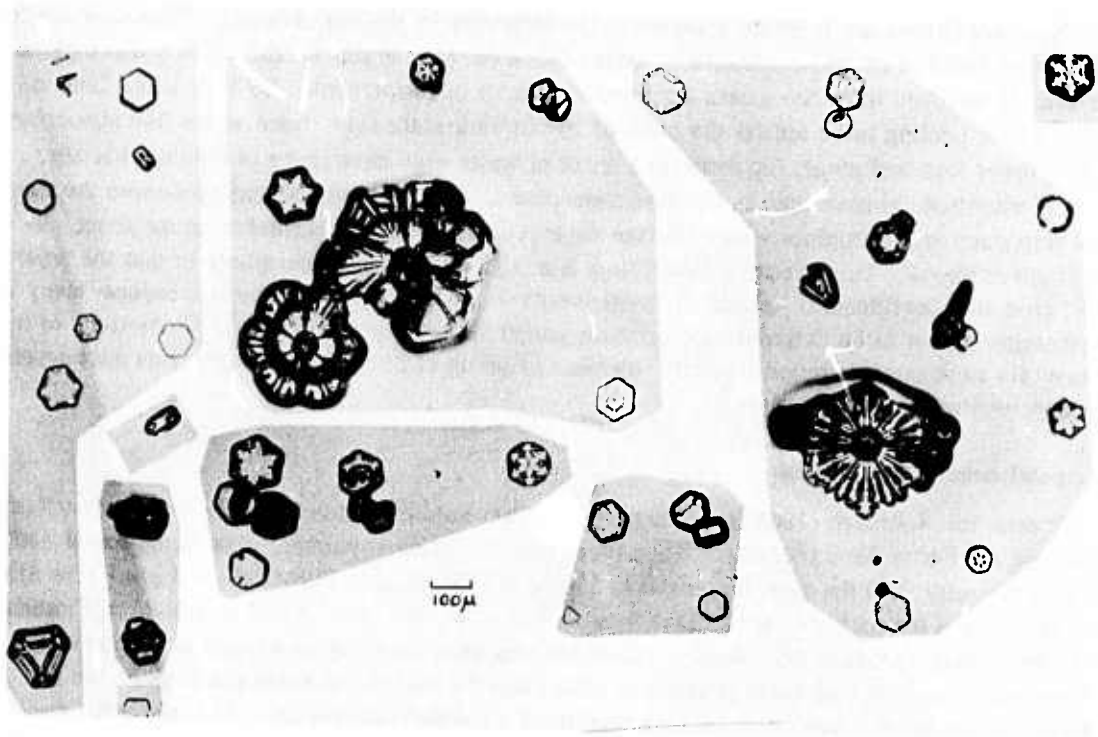


Figure 21. "Diamond dust" crystals of about 0.1 mm diameter.

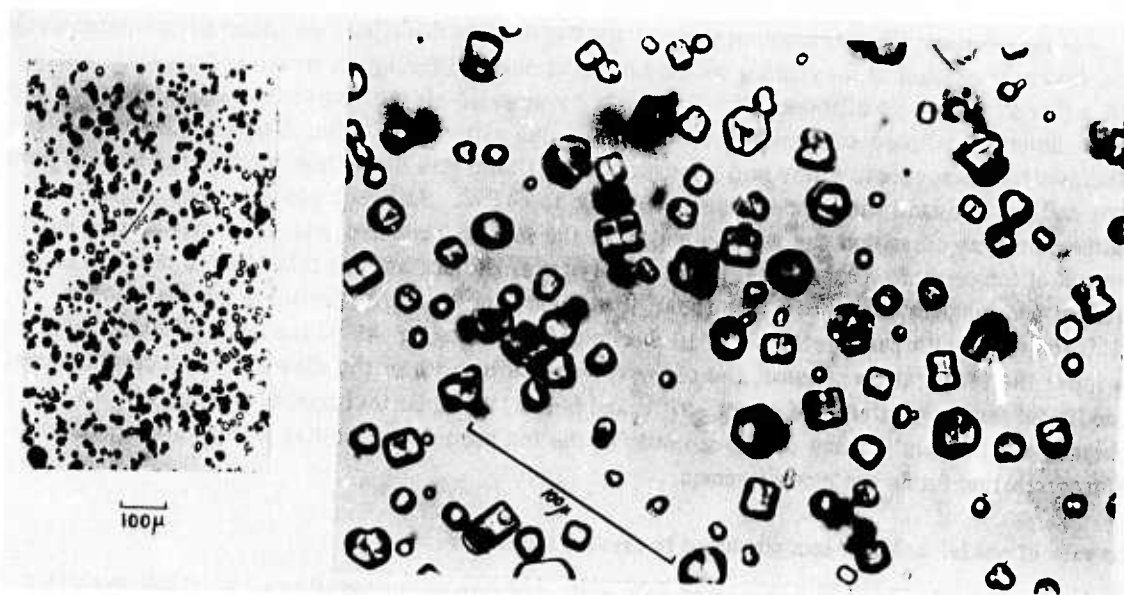


Figure 22. Ice fog crystals collected from a dense ice fog in a Fairbanks, Alaska, supermarket parking lot. Average droxtal diameter is in the 10-20  $\mu$  range.

These conditions are in sharp contrast to the formation of ice fog crystals. When droxtals form from cooling exhaust gases, originally at temperatures exceeding  $100^{\circ}\text{C}$ , the cooling takes place in less than 10 seconds when the gases are ejected into air of temperature  $-35^{\circ}\text{C}$  or less (Benson 1965). These cooling rates are on the order of  $10^6$  times greater than those in the free atmosphere. Cooling tower fogs and steam fog from open areas of water also have rates of cooling that are orders of magnitude greater than in the free atmosphere. Such a rapid cooling condenses the water vapor into many small droplets which become supercooled, and at temperatures below about  $-30^{\circ}\text{C}$  they begin to freeze. This process also differs from that in the free atmosphere in that the crystals do not grow in a continuously saturated environment. When studied under the microscope, many ice fog particles appear to be twinned (two crystals joined along a common plane). Collections of ice fog crystals show many twinned crystals, whereas twinning of cirrus cloud or diamond dust crystals and snow crystals is not prevalent.

#### Ice crystal density distribution

Thuman and Robinson (1954) made some of the first studies of ice fog size density distributions at Eielson Air Force Base (Alaska). They found that the average particle size in ice fog at  $-40^{\circ}\text{C}$  was  $13\ \mu$  diameter, and the size increased to  $16\ \mu$  at  $-30^{\circ}\text{C}$ . Kumai (1964) showed some size distributions for ice fog particles with sizes from  $4$  to  $12\ \mu$  for  $-30^{\circ}$  and  $-41^{\circ}\text{C}$  in downtown Fairbanks and at the airport, respectively. Kumai's distributions were based upon a count of the crystals precipitated on a collection surface (a glass slide) and are subject to some doubt since the fall speed of the ice fog particles may be less than local turbulent air updrafts. Ohtake (1970) made calculations of the terminal velocity versus particle size using Stokes' law for spherical particles. For  $33\text{-}\mu$  particles, the terminal velocity is  $3.47\ \text{cm/sec}$ , while for  $9\text{-}\mu$  particles the terminal velocity is only  $2.7\ \text{mm/sec}$ . Thus only slight air motion can cause considerable uncertainty in any statistical properties deduced from ice fog precipitation studies.

For this reason, Ohtake made studies of ice fog density distributions using an impaction device. This device consisted of a cylinder with a nozzle at one end facing an interior glass slide coated with a thin film such as silicone oil. A measured volume of air was drawn through the nozzle, and the ice crystals collided with and were captured on the silicone oil film. The slide could then be withdrawn for microscopic study and photographing. Using this technique, samples of ice fog were taken and studied over the temperature range  $-30^{\circ}$  to  $-41^{\circ}\text{C}$ . Although his data were somewhat scattered, it was clear that the mean diameter of the ice fog particles was a linearly increasing function of temperature. Figure 23, taken from Ohtake, illustrates this relationship between mean diameter and temperature. From this figure it is clear that  $30\text{-}\mu$  size particles are the rule for  $-31^{\circ}\text{C}$  ice fogs, with particle sizes of  $10\ \mu$  or less dominating in  $-40^{\circ}\text{C}$  ice fogs. Ohtake found that the lower the temperature became, the narrower was the breadth of the distribution in crystal sizes. In addition, for temperatures of about  $-37^{\circ}\text{C}$  and below, the spherical particles (Thuman and Robinson's "droxtals") make up the majority of the fog particles, whereas at higher temperatures other crystalline forms are more common.

#### The role of nuclei and low temperatures in crystal formation

Ice fog is a phenomenon associated only with subfreezing temperatures. Naturally occurring ice fog has always been observed to disappear when the temperature rose above  $-30^{\circ}\text{C}$  (Benson 1965). The occurrence of liquid water droplets in subfreezing temperatures is the commonly observed phenomenon of supercooling which occurs in fogs above about  $-30^{\circ}\text{C}$ . The only condition necessary for producing supercooled water is that no ice be present when the water is cooled down to and below  $0^{\circ}\text{C}$ . That is, the melt must not be "seeded" with the solid phase. Furthermore, supercooling always takes place in unseeded melts before freezing occurs. This is also true for

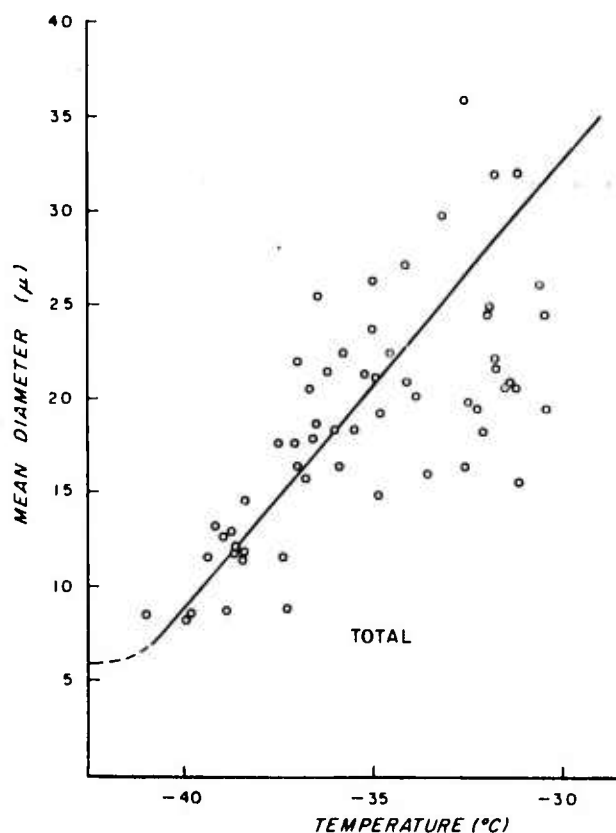


Figure 23. Relationship between mean diameters of total ice-fog crystals and temperatures. (From Ohtake 1970.)

supersaturated solutions prior to crystallization and precipitation of one of the components of the solution. In a cloud, freezing starts either when the cloud is cooled below a certain temperature or when the cloud is seeded or nucleated with some suitable foreign substance.

Many observers have reported that at a temperature of  $-40 \pm 1.5^\circ\text{C}$  clouds are always composed of ice crystals (Civilong 1945, 1947a, b, Schaefer 1946, 1948, D'Albe 1948, Oliver and Oliver 1949, Mason 1950). Civilong used a Wilson cloud chamber in his study, and he found that when the temperature was greater than  $-35^\circ\text{C}$  at the end of expansion progress, when condensation had just started to occur, no ice crystals were to be observed. However, when the temperature was below  $-35^\circ\text{C}$ , then a few ice crystals formed in the fog. Larger numbers of ice crystals began to appear as the temperature was lowered, and at about  $-41^\circ\text{C}$  the fog was composed entirely of ice crystals. Civilong found that below this temperature,  $-41^\circ\text{C}$ , sublimation was involved where ice crystals and no water droplets formed. This "threshold temperature" was found to increase with an increasing nucleating impurity added to the air.

Schaefer (1946, 1948) made supercooled fog by blowing moist air into a cold chamber. He found that ice crystals did not form until the temperature was lowered below about  $-39^\circ\text{C}$ , or upon the introduction of an appropriate nucleating substance. Vonnegut, in a series of papers (1947, 1949a, b), investigated the effects of silver iodide, potassium iodide, and several lead oxide compounds as nucleating agents for ice crystal formation in clouds. He found silver iodide (AgI) to be the most effective nucleating agent, and attributed its effect to its close crystalline similarity with ice crystals.

thus allowing water vapor in the air to sublime directly onto the silver iodide crystals. In urban areas, combustion byproducts of sizes generally less than about  $0.1 \mu$  diameter can also be effective ice fog nucleating agents (Ohtake 1967, Kumai and O'Brien 1965). The role that foreign impurities, of all types, play as nucleating agents in "clean" air is well documented, especially since the advent of the electron microscope (Ohtec 1949, Mason 1950, Kuroiwa 1957, Kumai 1951). That these "condensation nuclei" play an important role in ice fog formation is undoubted, since ample photographic evidence of ice fog particles with an enclosed nucleus exist (Kumai and O'Brien 1965, Ohtake 1967, 1970). Benson (1965) reports that in the Fairbanks-Ft. Wainwright area of Alaska ice fog begins to set in at about  $-35^{\circ}\text{C}$  and is always well developed at  $-40^{\circ}\text{C}$  and lower. In the "polluted" air of this area droplet freezing may set in at air temperatures as high as  $-30^{\circ}\text{C}$ , and the pollutants need be of no special type in order to be effective.

All of this is not to say that condensing and freezing nuclei are indispensable to ice fog formation. While Kumai reported that all of the ice fog crystals he collected had nuclei, Ohtake (personal communication, 1972) reported that ice fog can be formed without active nuclei provided the temperature is  $-37^{\circ}\text{C}$  or lower. Ohtake (1970) also reported that 71 out of 713 crystals from Chena and Manley Hot Springs inspected under the electron microscope did not have any nuclei. Most of these were found at temperatures below about  $-40^{\circ}\text{C}$ . Furthermore, at the center of Fairbanks 1.7% of 236 crystals examined from an ice fog at  $-39^{\circ}\text{C}$  had no nuclei.

#### Phase change effects on development of ice fog

While the size of the ice fog particles is a linearly increasing function of atmospheric temperature, the concentration of the crystals is determined in part by the amount of moisture vapor injected into the cold atmosphere. Typical concentrations for Fairbanks, as reported by Ohtake (1970), are around  $200/\text{cm}^3$ , to  $1000/\text{cm}^3$ . And although Ohtake reports finding only about 300 condensation nuclei per cubic centimeter at Chena Hot Springs under ice fog conditions, he found about twice that concentration of ice crystals. Other observers (Kumai 1964, Benson 1965) are substantially in agreement with these measured concentrations.

In addition to the available moisture, from whatever sources, the role of atmospheric temperature and the effect of the change in phase from water to ice in an ice fog event need to be examined. It has been observed that air containing high concentrations of combustion byproducts can furnish ample condensation and freezing nuclei for the onset of an ice fog event at temperatures as high as  $-30^{\circ}$  or  $-35^{\circ}\text{C}$ . The phase change from water droplets to ice crystals at this temperature has a strong effect on fog formation. If the air near the ground is cooling rapidly, and some supercooled water droplet fogs are forming, such as over open water areas, then the low level air will be saturated or close to saturation with respect to water.

For example,  $-34^{\circ}\text{C}$ , the capacity of the air to hold water vapor decreases with decreasing temperature at about  $-0.0279 \text{ g/m}^3 \text{ }^{\circ}\text{C}$  (over water). Thus, if the air is saturated, cooling the air one degree from  $-34^{\circ}$  to  $-35^{\circ}\text{C}$  would provide about  $0.0279 \text{ g/m}^3$  of condensed moisture. Now suppose the droplets freeze at  $-34^{\circ}\text{C}$ . There is now an additional reduction in the air's capability to hold moisture because the saturation vapor pressure must be found with respect to ice. The saturation vapor density over ice at  $-34^{\circ}\text{C}$  is  $0.2254 \text{ g/m}^3$ , while over water the vapor density is only  $0.3138 \text{ g/m}^3$ . Thus, the excess water vapor produced simply by freezing droplets at  $-34^{\circ}\text{C}$  is  $0.0884 \text{ g/m}^3$ , which gives a total of about  $0.1163 \text{ g/cm}^3$  in going from  $-34^{\circ}\text{C}$  to  $-35^{\circ}\text{C}$ , whereas only about  $0.0279 \text{ g/m}^3$  water was condensed in going from  $-33^{\circ}$  to  $-34^{\circ}\text{C}$ . Thus, the excess moisture produced by freezing at  $-34^{\circ}\text{C}$  is 3.16 times as great as the moisture condensed by one degree of cooling at  $-34^{\circ}\text{C}$ . Now suppose that freezing is postponed (for whatever reason) until  $-44^{\circ}\text{C}$ . The excess moisture produced by freezing at  $-44^{\circ}\text{C}$  is now 3.36 times as much as is produced by one degree of cooling at  $-44^{\circ}\text{C}$ . Therefore the relative contribution of water vapor due to freezing increases with a decreasing freezing point.

This argument is meant to emphasize and substantiate two observational facts about ice fogs: they have been observed to appear suddenly over widespread areas, and denser fogs have been observed at low temperatures than at higher temperatures. The above calculations were based upon the densities of water vapor at saturation over water and over ice (List 1966, Tables 108 and 109).

#### IV. DIELECTRIC BEHAVIOR OF A MEDIUM WITH HOMOGENEOUSLY DISTRIBUTED PARTICLES

##### Dielectric behavior of a medium of small particles

Van de Hulst (1957) derived an expression for the complex refractive index of a medium containing many small scatterers. His expression for  $m_m = n' - jn''$  is

$$n' = 1 + \frac{2\pi N}{k^3} \text{Im}[S(0)]$$

$$n'' = \frac{2\pi N}{k^3} \text{Re}[S(0)]$$

where  $k = 2\pi/\lambda_0 = \omega \sqrt{\mu_0 \epsilon_0}$

$N$  = scatterer number density

$S(0)$  = complex amplitude coefficient for forward scattering

$$= \frac{1}{2} \sum_{n=1}^{\infty} (2n+1)(a_n^S + b_n^S)$$

and where  $a_n^S$  and  $b_n^S$  are the complex amplitude coefficients for the  $n$ th magnetic and electric modes, respectively.

This expression was derived to apply to the case where the distance between particles is large compared with both the wavelength and the size of the particles. Dense packing of particles is thus excluded. Scattering contributions from the small particles which affect the phase of the transmitted wave come not from particles on all sides, but only from particles that are nearly directly behind the point of observation. This expression is accurate for the complex refractive index of the medium close to 1.

An alternate expression for the opposite case is the expression derived by Lorentz-Lorenz (Jackson 1963):

$$4\pi a N = \frac{3(m_m^2 - 1)}{m_m^2 + 2}$$

where  $a$  = polarization of the particle

$p = aE_0$ , the induced dipole moment due to the incident electric field  $E_0$ .

This expression, derived as a part of the theory of molecular optics, is clearly not the same as the Van de Hulst expression, yet both expressions give the complex refractive index of a medium as a whole in terms of the scattering properties of the individual particles.

The Lorentz-Lorenz expression is derived for the conditions that the mutual distances of the particles are small compared with the wavelength, which of course means that the particles are much smaller than a wavelength. The field at a given point of observation is due to the scattered fields of a fairly large number of nearby particles on all sides of the point of interest. These fields are nearly in phase with the incident field, and it is the statistical effect of these fields which gives rise to the Lorentz-Lorenz formula.

However, the Lorentz-Lorenz formula can give the Van de Hulst expression for the case of a dilute gas of small scatterers where  $m_m \approx 1$ . Here,

$$4\pi a N = \frac{3(m_m^2 - 1)}{m_m^2 + 2} = \frac{3[2(m_m - 1)]}{3} = 2(m_m - 1)$$

$$\therefore m_m = 1 + 2\pi a N$$

and  $m_m$  refers to the complex dielectric constant of the medium as a whole. For scatterers small in terms of a wavelength

$$S(0) = jk^3 a$$

since for spheres of radius  $a$

$$a = \left( \frac{m^2 - 1}{m^2 + 2} \right) a^3$$

where  $m$  is the complex refractive index of the sphere material. So

$$j \frac{2}{3} \left( \frac{m^2 - 1}{m^2 + 2} \right) (ka)^3$$

is the coefficient for the first electric mode of a dielectric sphere, which is just the familiar expression for the case of Rayleigh scattering. Thus,

$$m_m = 1 + 2\pi N S(0)$$

which is just Van de Hulst's expression.

This expression is appropriate to use to model the complex refractive index of an ice fog since an ice fog is composed of a dilute assemblage of ice particles that are small in terms of the incident electromagnetic wave.

Sample calculations using the Van de Hulst expression for the index of refraction of the ice fog medium are delayed to a later section pending the fog impactor measurements and a discussion of the results. However, it is clear that this expression predicts a refractive index which is sensitive to the total volume of ice per unit volume. Thus, on a per ice sphere basis, an ice particle 30  $\mu$  in diameter has nine times the effect of one 10  $\mu$  in diameter. A relatively small number of large particles can strongly influence the measured refractive index. Thus, in order to accurately apply Van de Hulst's formula you must know not only the numbers involved but also the particle sizes.

### Radio wave energy loss mechanisms

When a plane electromagnetic wave is incident upon a dilute cloud of small particles, energy is extracted from the incident wave in proportion to the absorption and scattering cross sections presented by the small particles. For the case where the incident electromagnetic wave has a wavelength much larger than the circumferential size of the aerosol particles, the Rayleigh approximations for the scattering and absorption cross sections (Stratton 1941) are valid and are given by the expressions

$$Q_s = \frac{2\pi^5}{3} \lambda^2 |K|^2 D_\lambda^6$$

$$Q_a = \pi^2 \operatorname{Im}(-K) \lambda^2 D_\lambda^3$$

where  $\operatorname{Im}$  = imaginary part of argument

$D_\lambda$  = particle diameter in wavelengths

$$K = \frac{m^2 - 1}{m^2 + 2}$$

and  $m$  is the complex refractive index of the aerosol dielectric material.

A computer program was used to determine the extinction, scattering and absorption cross sections for ice spheres from 1 to 35  $\mu$  in size. This computer routine was used since it had already been written for use at optical frequencies to calculate 6328 Å helium-neon laser extinction due to a fog. This routine calculates the complex amplitudes of the  $n$ th electric and magnetic modes set up in each dielectric sphere by the incident wave. These amplitude coefficients,  $a_n$  and  $b_n$  (Stratton 1941), were in turn used to calculate the following parameters appropriate for each fog particle size from the following expressions:

#### Scattering cross section

$$Q_s = \frac{\text{total power scattered over } 4\pi \text{ steradians}}{\text{incident power density}}$$

$$= \frac{\lambda^2}{2\pi} \sum_{n=1}^{\infty} (2n + 1) (|a_n|^2 + |b_n|^2) \quad (1)$$

#### Extinction cross section

$$Q_E = \frac{\text{total power extracted from the wave}}{\text{incident power density}}$$

$$= \frac{\lambda^2}{2\pi} \operatorname{Re} \left[ \sum_{n=1}^{\infty} (2n + 1) (a_n + b_n) \right] \quad (2)$$

#### Absorption cross section

$$Q_A = Q_E - Q_s \quad (3)$$

An equivalent expression for the extinction cross section is given by

$$Q_E = 2kn''$$

where  $n''$  is the imaginary part of the Van de Hulst expression for the complex index of refraction given earlier, and  $k = 2\pi/\lambda$ .

While the Van de Hulst expression gives an extinction coefficient, it does not give separate expressions for scattering and absorption. Since these quantities may be of interest, expressions 1-3 were used to determine these parameters with the aid of a previously written computer program. In computing the scattering, absorption and extinction cross sections in the manner defined above, five terms were taken in the summation indicated. However, this is not necessary as all terms greater than the first are orders of magnitude smaller.

Table V lists the dominant Rayleigh parameters and the attenuation and scattering cross sections for ice fog particles at 96.5 GHz for a complex dielectric constant of  $3.08 - j(0.004)$  which is appropriate for the actual measured complex dielectric constant at this frequency. It is clear that at 3 mm wavelength absorption is the dominant extinction mechanism.

For a wave passing through such a dissipative medium, the extinction coefficient per meter thickness of the fog,  $\tau$ , is found from

$$\tau = \sum_{\substack{\text{all} \\ \text{particles}}} \frac{\pi D^2}{4} N(D) Q_N(m, D) \text{ meters}^{-1}$$

where  $D$  = particle diameter, meters

$N(D)$  = number of particles of diameter  $D$  per cubic meter

$Q_N(m, D)$  = normalized extinction coefficient

$$= Q_E / (\pi D^2 / 4).$$

It is clear that this implies that

$$P = P_0 e^{-\tau x}$$

where  $P$  = received power density

$P_0$  = initial power density

$x$  = absorption path length.

The application of these expressions to the electromagnetic measurements is deferred to a later chapter pending the actual fog impactor and electromagnetic measurements. However, it can be said here that this model is in reasonably good accord with the EM measurements considering the uncertainty which is shown to exist in the fog impactor measurements.

**Table V. Complex scattering coefficients and attenuation cross sections for ice particles at 96.5 GHz.**

Particle diam ( $\mu$ )	Complex first electric mode coeff		Absorption cross section ( $m^2$ )	Scattering cross section ( $m^2$ )	Normalized extinction cross section [ $Q_E/(\pi D^2/4)$ ]
	$b_1^{re}$	$b_1^{im}$			
1	$3.25 \times 10^{-13}$	$2.87 \times 10^{-10}$	$1.48 \times 10^{-18}$	$5.75 \times 10^{-25}$	$1.88 \times 10^{-6}$
2	$2.61 \times 10^{-12}$	$2.30 \times 10^{-9}$	$1.19 \times 10^{-17}$	$2.40 \times 10^{-23}$	$5.78 \times 10^{-6}$
3	$8.80 \times 10^{-12}$	$7.75 \times 10^{-9}$	$4.01 \times 10^{-17}$	$2.73 \times 10^{-23}$	$5.67 \times 10^{-6}$
4	$2.09 \times 10^{-11}$	$1.84 \times 10^{-8}$	$9.50 \times 10^{-17}$	$1.54 \times 10^{-21}$	$7.56 \times 10^{-6}$
5	$4.07 \times 10^{-11}$	$3.59 \times 10^{-8}$	$1.86 \times 10^{-16}$	$5.86 \times 10^{-21}$	$9.46 \times 10^{-6}$
6	$7.04 \times 10^{-11}$	$6.20 \times 10^{-8}$	$3.21 \times 10^{-16}$	$1.75 \times 10^{-20}$	$1.13 \times 10^{-5}$
7	$1.12 \times 10^{-10}$	$9.84 \times 10^{-8}$	$5.09 \times 10^{-16}$	$4.41 \times 10^{-20}$	$1.32 \times 10^{-5}$
8	$1.67 \times 10^{-10}$	$1.47 \times 10^{-7}$	$7.60 \times 10^{-16}$	$9.83 \times 10^{-20}$	$1.51 \times 10^{-5}$
9	$2.38 \times 10^{-10}$	$2.09 \times 10^{-7}$	$1.08 \times 10^{-15}$	$1.99 \times 10^{-19}$	$1.70 \times 10^{-5}$
10	$3.26 \times 10^{-10}$	$2.87 \times 10^{-7}$	$1.49 \times 10^{-15}$	$3.75 \times 10^{-19}$	$1.89 \times 10^{-5}$
11	$4.34 \times 10^{-10}$	$3.82 \times 10^{-7}$	$1.98 \times 10^{-15}$	$6.65 \times 10^{-19}$	$2.08 \times 10^{-5}$
12	$5.63 \times 10^{-10}$	$4.96 \times 10^{-7}$	$2.57 \times 10^{-15}$	$1.12 \times 10^{-18}$	$2.27 \times 10^{-5}$
13	$7.16 \times 10^{-10}$	$6.30 \times 10^{-7}$	$3.26 \times 10^{-15}$	$1.81 \times 10^{-18}$	$2.46 \times 10^{-5}$
14	$8.95 \times 10^{-10}$	$7.87 \times 10^{-7}$	$4.08 \times 10^{-15}$	$2.82 \times 10^{-18}$	$2.65 \times 10^{-5}$
15	$1.10 \times 10^{-9}$	$9.68 \times 10^{-7}$	$5.01 \times 10^{-15}$	$4.27 \times 10^{-18}$	$2.84 \times 10^{-5}$
16	$1.34 \times 10^{-9}$	$1.18 \times 10^{-6}$	$6.08 \times 10^{-15}$	$6.29 \times 10^{-18}$	$3.03 \times 10^{-5}$
17	$1.60 \times 10^{-9}$	$1.41 \times 10^{-6}$	$7.30 \times 10^{-15}$	$9.06 \times 10^{-18}$	$3.22 \times 10^{-5}$
18	$1.90 \times 10^{-9}$	$1.67 \times 10^{-6}$	$8.66 \times 10^{-15}$	$1.28 \times 10^{-17}$	$3.41 \times 10^{-5}$
19	$2.24 \times 10^{-9}$	$1.97 \times 10^{-6}$	$1.02 \times 10^{-14}$	$1.77 \times 10^{-17}$	$3.60 \times 10^{-5}$
20	$2.61 \times 10^{-9}$	$2.30 \times 10^{-6}$	$1.19 \times 10^{-14}$	$2.40 \times 10^{-17}$	$3.79 \times 10^{-5}$
21	$3.02 \times 10^{-9}$	$2.66 \times 10^{-6}$	$1.38 \times 10^{-14}$	$3.22 \times 10^{-17}$	$3.98 \times 10^{-5}$
22	$3.48 \times 10^{-9}$	$3.05 \times 10^{-6}$	$1.58 \times 10^{-14}$	$4.25 \times 10^{-17}$	$4.17 \times 10^{-5}$
23	$3.98 \times 10^{-9}$	$3.49 \times 10^{-6}$	$1.81 \times 10^{-14}$	$5.55 \times 10^{-17}$	$4.36 \times 10^{-5}$
24	$4.52 \times 10^{-9}$	$3.97 \times 10^{-6}$	$2.05 \times 10^{-14}$	$7.17 \times 10^{-17}$	$4.56 \times 10^{-5}$
25	$5.11 \times 10^{-9}$	$4.48 \times 10^{-6}$	$2.32 \times 10^{-14}$	$9.16 \times 10^{-17}$	$4.75 \times 10^{-5}$
26	$5.75 \times 10^{-9}$	$5.04 \times 10^{-6}$	$2.61 \times 10^{-14}$	$1.16 \times 10^{-16}$	$4.94 \times 10^{-5}$
27	$6.45 \times 10^{-9}$	$5.65 \times 10^{-6}$	$2.93 \times 10^{-14}$	$1.45 \times 10^{-16}$	$5.13 \times 10^{-5}$
28	$7.19 \times 10^{-9}$	$6.30 \times 10^{-6}$	$3.26 \times 10^{-14}$	$1.81 \times 10^{-16}$	$5.33 \times 10^{-5}$
29	$8.00 \times 10^{-9}$	$7.00 \times 10^{-6}$	$3.62 \times 10^{-14}$	$2.23 \times 10^{-16}$	$5.52 \times 10^{-5}$
30	$8.86 \times 10^{-9}$	$7.75 \times 10^{-6}$	$4.01 \times 10^{-14}$	$2.74 \times 10^{-16}$	$5.72 \times 10^{-5}$
31	$9.78 \times 10^{-9}$	$8.55 \times 10^{-6}$	$4.43 \times 10^{-14}$	$3.33 \times 10^{-16}$	$5.91 \times 10^{-5}$
32	$1.08 \times 10^{-8}$	$9.40 \times 10^{-6}$	$4.87 \times 10^{-14}$	$4.03 \times 10^{-16}$	$6.11 \times 10^{-5}$
33	$1.18 \times 10^{-8}$	$1.03 \times 10^{-5}$	$5.34 \times 10^{-14}$	$4.85 \times 10^{-16}$	$6.30 \times 10^{-5}$
34	$1.29 \times 10^{-8}$	$1.13 \times 10^{-5}$	$5.84 \times 10^{-14}$	$5.80 \times 10^{-16}$	$6.50 \times 10^{-5}$
35	$1.41 \times 10^{-8}$	$1.23 \times 10^{-5}$	$6.37 \times 10^{-14}$	$6.90 \times 10^{-16}$	$6.70 \times 10^{-5}$

## V. METHOD FOR MAKING COMPLEX PERMITTIVITY MEASUREMENTS OF A FOG

### Literature review of millimeter wave Fabry-Perot interferometry

If a cavity is used to measure low losses and refractive index changes of ten  $N$ -units or less ( $1 N$ -unit =  $(n - 1) \times 10^6$ , where  $n$  is the index of refraction), it must have a high  $Q$ . Using a cavity with a  $Q$  of  $10^5$  one can easily detect a  $1 N$ -unit change (97 kHz at 97 GHz). One type of high  $Q$  cavity successfully used at millimeter wave frequencies is the spherical mirror Fabry-Perot interferometer (FPS). The FPS is widely used in maser and laser technology because of its inherently high resolving power and its relative ease of adjustment. This cavity has a much higher  $Q$  than the quarter-wave coaxial cavity more commonly used in the microwave spectrum (which may have unloaded  $Q$ 's of up to 10,000). An extensive body of literature exists on the Fabry-Perot cavity, and some good tutorial papers are those of Fox and Li (1961), Schawlow and Townes (1958), Boyd and Gordon (1961), and Boyd and Kogelnik (1962). The paper by Kogelnik and Li (1966) is an excellent review of open-sided resonators and contains much material of a tutorial nature. Culshaw, in a series of papers (1959, 1960, 1961, 1962), discussed the application and design of Fabry-Perot interferometers for the millimeter wave spectrum. Much of Culshaw's emphasis was placed upon the theory and design of the parallel-plate Fabry-Perot, and methods of coupling the electromagnetic energy into and out of this type of structure. His 1960 paper describes one such plane-parallel resonator built for operation at a wavelength of 6 mm which had a  $Q$  of about 100,000. Zimmerer, Anderson, Strine and Beers (1963) discussed the construction of both plane-parallel and spherical Fabry-Perot resonators and considered the problem of obtaining efficient power transfer into the resonant structures. A separate paper by Zimmerer (1963) considered measurements of the transverse E-field variations of a spherical mirror Fabry-Perot resonator as a function of reflector size and spacing. Valkenburg and Derr (1966), Culshaw and Anderson (1962), Frenkel and Woods (1966), Degenford and Coleman (1966), and French and Arnold (1967) are among some who have built and used the FPS to make measurements of gas absorption and permittivity in the millimeter wave spectrum. Dees and Sheppard (1965) reported on the construction of a semi-confocal FPS with a  $Q$  of 88,000 at 168 GHz. Zimmerer (1962) reports the construction of a novel high precision wave-meter covering the 50 to 75 GHz band. Zimmerer mounted his confocal resonator on a precision screw thread, and took advantage of the fact that cavity resonances occur at intervals of  $\lambda/2$  to measure the operating frequency to a high degree of accuracy.

There are two basic geometric forms for the Fabry-Perot interferometer: the parallel flat plate type and the confocal type. The parallel-plate version is the form of the original optical resonator as constructed by Fabry and Perot, and is perhaps the most widely known version of the two. This type uses very highly reflective plane parallel plates whose surfaces must both be flat to within about  $1/1000\lambda$  and parallel to a very high degree to minimize diffraction losses in order to attain a high operating  $Q$ . The millimeter analog of this type has been built (Culshaw 1961, for example), but plate alignment is a nontrivial problem and in general relatively large plates are required to reduce diffraction losses, even for relatively close plate separations. Both Culshaw in his series of papers (op. cit.) and Zimmerer et al. (1963) have treated the problem of coupling energy into and out of these flat-plate resonators.

The confocal type of the Fabry-Perot interferometer has all of the advantages and few of the disadvantages of the flat plate type of interferometer. The spherical mirrors eliminate the critical alignment problem, and the focusing action of these mirrors decreases the diffraction loss significantly. The confocal FPS has two mirrors of equal radius of curvature, with the radius of curvature of each mirror coincident with the surface of the other (see Fig. 21a). The semi-confocal FPS is a version of the confocal type, with one spherical mirror imaged by the flat plate. The semi-confocal

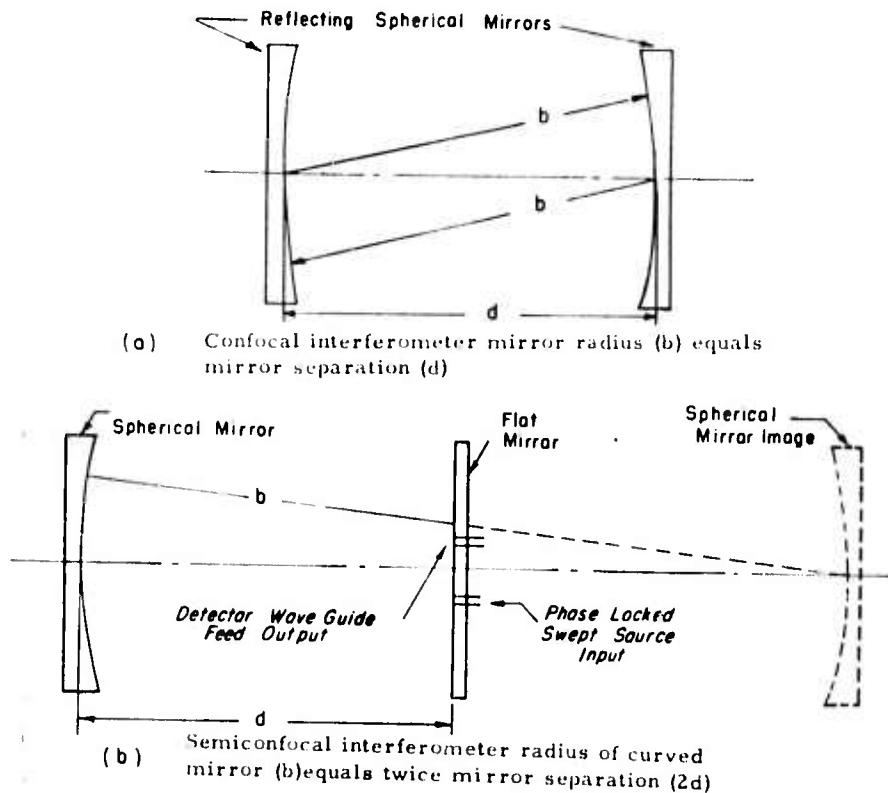


Figure 24. Confocal and semi-confocal Fabry-Perot interferometers.

FPS is quite practical and easily built, and the coupling problem is simplified in that waveguide feeds may be brought through the back of the flat and located symmetrically about the center line of the cavity. The separation of the flat and the spherical mirror is at a distance of half the radius of curvature of the spherical mirror (Fig. 24b). The field and mode distribution for semi-confocal and confocal FPS are identical for equal mirror sizes and equal radii of curvature. However, the  $Q$  of a semi-confocal FPS is half that of the confocal FPS since energy has to travel only half as far in the semi-confocal case.

**Theoretical considerations**

In order to discuss the relationship between cavity  $Q$ , mode structure and mirror size, it is necessary to discuss briefly the basic theoretical development behind these resonators. In this sense, the approach of Fox and Li (1961) will be followed. Their approach to the open resonator problem was to consider a propagating wave which was reflected back and forth between two plane mirrors. By assuming an arbitrary initial field distribution at the first mirror, the field at the second mirror was calculated using the scalar formulation of Huygen's principle. This field was used to calculate the field back at the first mirror on the second transit, etc. Only after several hundred iterations did the field approach a steady state, differing only by a complex constant from mirror to mirror. Without further derivation, their iterative equation for confocal spherical mirrors of circular cross section is

$$u_{q+1}(r_2, \phi_2) = \frac{i}{2\lambda} \int_0^a \int_0^{2\pi} u_q(r_1, \phi_1) \frac{e^{-jkR}}{R} \left(1 + \frac{b_1}{R}\right) r_1 d\phi_1 dr_1$$

with

$$R = [b_1^2 + r_1^2 + r_2^2 - 2r_1r_2 \cos(\phi_1 - \phi_2)]^{1/2}$$

and

$$b_1 = b - \Lambda_1 - \Lambda_2,$$

$$\Lambda_i = b - (b^2 - r_i^2)^{1/2}, \quad i = 1, 2$$

$$= \frac{r_i^2}{2b}, \quad i = 1, 2 \quad \text{for large } b/a.$$

Using this simplification,  $u_{q+1}(r_2, \phi_2)$  simplifies to

$$u_{q+1}(r_2, \phi_2) = \frac{je^{-jkb}}{\lambda b} \int_0^a \int_0^{2\pi} u_q(r_1, \phi_1) \exp[jk(r_1r_2/b) \cos(\phi_1 - \phi_2)] r_1 d\phi_1 dr_1$$

which is strictly valid for  $(a^2/b\lambda) \ll (b/a)^2$ .

Figure 25 defines the terms appropriate for the above terminology. In this equation, the single most important parameter is  $(a^2/b\lambda)$ . This parameter, called the Fresnel number, is approximately the number of Fresnel zones seen in one mirror from the center of the other, and determines the numbers of ripples in the amplitude and phase distribution of the electric field of each mirror.

Calculations by Fox and Li made using the iterative procedure and the above equations indicate that of all the  $TEM_{m,n,q}$  modes, those with higher order of radial variation ( $m \geq 1$ ) and angular variation ( $n \geq 1$ ) have higher losses and phase shift than does the  $TEM_{00,q}$  mode. Higher order mode losses decrease sharply with increasing Fresnel number ( $N = a^2/b\lambda$ ). To decrease both the level and the number of undesired higher-order mode frequency responses, the Fresnel number of the millimeter wave FPS is made as small as possible, with the minimum  $N$  set by the mirror diffraction losses. This effect is well shown by Figure 15 of Fox and Li, reproduced here as Figure 26. From this figure it is clear that the power loss is 20 times greater for the  $TEM_{01,q}$  mode than for the  $TEM_{00,q}$  mode. From this figure it is also clear how the power loss of the mirror (diffraction loss) varies as a function of the Fresnel number  $N$ . At  $N = 1.0$ , this loss (in percent) is about 0.05, and for  $N = 0.5$ , the loss is about 10. Thus, for a factor of two change in  $N$ , the loss increases 200 times. It is clear that the optimum range for  $N$  is closely restricted to a narrow range about 1.0 for there to be a minimum diffraction loss together with good higher order mode suppression. Kogelnik and Li (1966) calculated the phase shift per transit for both  $TEM_{01,q}$  and  $TEM_{00,q}$  modes in a confocal resonator. For  $N = 1.0$ , the phase shift for the  $TEM_{00,q}$  mode is about  $95^\circ$ , while for the  $TEM_{01,q}$  mode it is  $190^\circ$ . This phase shift difference of  $95^\circ$  implies that the two modes will resonate at different mirror separations. This separation should be about  $\lambda/4$ , and in fact the higher order mode for the cavity built for this experiment had this higher order mode displaced  $0.26\lambda$  from the  $TEM_{00,q}$  mode, in good agreement with the above prediction.

Both Boyd and Gordon and Fox and Li give as the  $Q$ -factor for a multimode confocal resonator:

$$Q = \frac{2\pi b}{a\lambda_g} \cdot \left(\frac{\lambda_g}{\lambda}\right)^2 = \frac{2\pi b}{a\lambda}$$

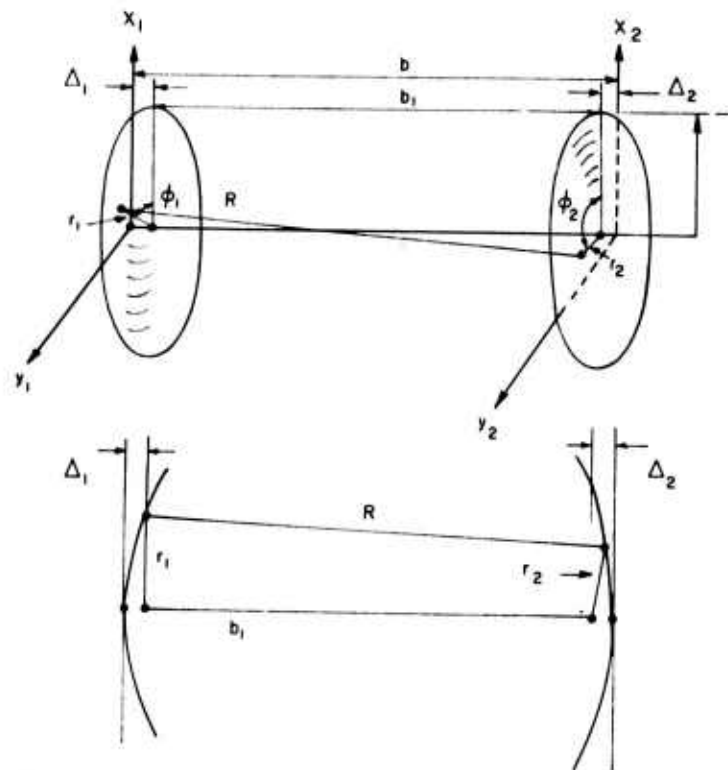


Figure 25. Terminology appropriate to theoretical treatment of FPS.

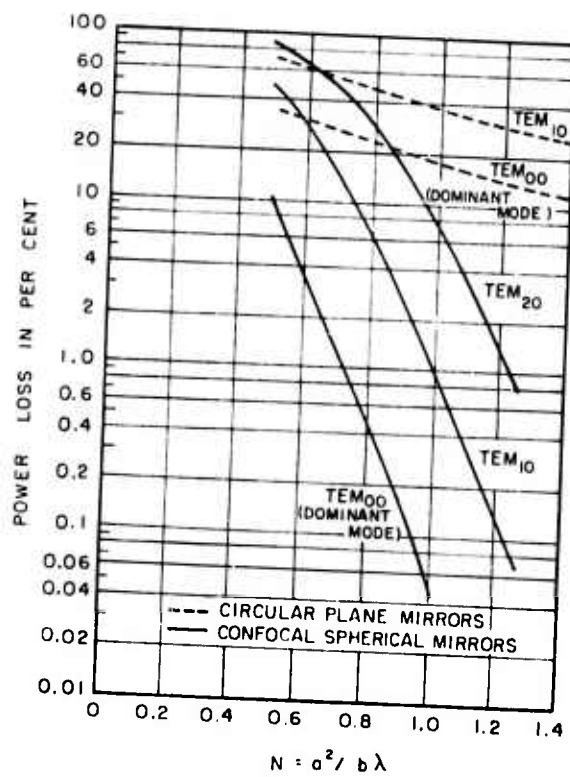


Figure 26. Power loss per transit vs  $N = a^2/b\lambda$  for confocal spherical mirrors. Dashed curves for circular plane are shown for comparison. (After Fox and Li 1961.)

since  $\lambda_g = \lambda[1 + \lambda/2\pi b] = \lambda$

$b$  = mirror-to-mirror separation

$a$  = losses of cavity, per transit

$\lambda$  = wavelength.

This relationship would seem to indicate that the cavity  $Q$ -factor increases directly with mirror separation. This is true up to the point where mirror diffraction effects increase the losses as fast as the separation increases, even allowing for the increasing mirror size (as dictated by the Fresnel criterion) with separation. Cavity  $Q$ -factors greater than  $10^6$  at 150 GHz have been reported by French and Arnold (1967). Depending upon the construction, coupling technique, and the precision with which the FPS is made and aligned,  $Q$ 's of 50,000 and greater are not difficult to achieve at millimeter wavelengths.

In order to calculate, at least to first order, the required separation of the mirrors for a given  $Q$ , some estimate of the losses must be obtained. This loss estimate will be made from summing the expected reflection, diffraction and coupling losses.

Mirror reflection loss is given by

$$a_R = 1 - |\Gamma|^2$$

where  $\Gamma = \frac{1+j}{g} - 1$

$g$  = reflection coefficient of the metal surface

and where

$$g = \left( \frac{\sigma}{4\pi\epsilon_0 f} \right)^{1/2}$$

and all other symbols have their standard meaning. For the aluminum spherical mirror

$$\sigma_{al} = 3.72 \times 10^7 \text{ mho/m}$$

and the copper flat plate

$$\sigma_{cu} = 5.80 \times 10^7 \text{ mho/m}$$

and since  $f = 9.7 \times 10^{10}$  c/s, then

$$g_{al} = 1.857 \times 10^3$$

$$g_{cu} = 2.32 \times 10^3.$$

Thus

$$1 - |\Gamma|^2 = \frac{2}{g} = 1.08 \times 10^{-3}, \text{ for aluminum}$$

$$= 8.62 \times 10^{-4}, \text{ for copper.}$$

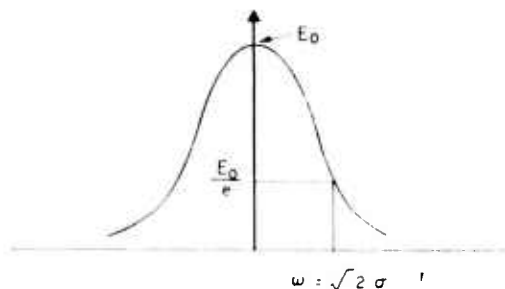


Figure 27. Amplitude distribution of  $TEM_{00q}$  mode (at any beam cross section).

The spherical mirror was made of aluminum since a suitable piece of round stock was available for cutting, grinding and polishing. Time and the lack of a large enough piece of copper did not permit this mirror to be made of copper. The initial flat was turned from aluminum, but the later availability of a piece of copper plate allowed this piece to be made from copper. This operation was not time consuming, since the face of the flat was lathe turned within half a day's time.

The coupling loss into and out of the cavity is the ratio of the total waveguide cross sectional area to the beam waist area on the flat mirror. The amplitude distribution for the fundamental mode ( $TEM_{00q}$ ) across the waist (in a radial direction) is Gaussian in form. The parameter  $\omega_0$  of the beam waist is the radial distance from the center one must move for the amplitude to fall to  $1/e$  of its maximum value. Figure 27 is a sketch of the radial beam amplitude distribution.  $\omega_0$ , often called the beam radius or spot size, is given by the relationship

$$\omega_0^2 = \frac{b\lambda}{2\pi},$$

where  $b$  is the radius of curvature of the spherical mirror and  $\lambda$  is the operating wavelength.  $\omega_0$  designates beam radius at the beam waist where  $d = b/2$ .

For a mirror of 72-in. radius of curvature and an operating wavelength of 3.09 mm, the spot size is of 30-mm radius. In assuming a spot size of 30-mm radius, this means that the majority of the power is concentrated in a spot with this radius on the flat mirror. This power within the spot size, as a fraction of the total power on the flat mirror, may easily be found as follows.

For  $F(x)$  = cumulative distribution function of standardized normal random variable

$$= \int_{-\infty}^x \frac{1}{\sqrt{2\pi}} e^{-2t^2} dt$$

then  $2(1 - F(x))$  = area in wings of the Gaussian function for  $|x| \geq \sqrt{2}$ . From a table of the normal distribution function  $1 - F(x) = 0.0793$ , and hence the fractional power enclosed by the spot size is 0.84 of the total power on the flat mirror.

For a type RG-09 waveguide, the area enclosed by the guide walls is  $4.802 \text{ mm}^2$ . Thus, the coupling loss is approximately

$$\frac{9.604 \text{ mm}^2}{2.82 \times 10^3 \text{ mm}^2} = 3.4 \times 10^{-3}.$$

Mirror diffraction losses are not so easily obtained. However, Fox and Li indicate that a diffraction loss on the order of  $5 \times 10^{-4}$  may be expected for a Fresnel number  $N = 1.0$ .

Thus, the total losses (per transit) for a Fabry-Perot cavity operating in the dominant mode with the mirrors constructed of copper and aluminum and fed with two type 99 waveguides located symmetrically about the center of the flat plate are the sum of the  $I^2R$  mirror losses, the coupling losses, and the diffraction loss. This comes to  $\alpha_T = 5.84 \times 10^{-3}$ , but since further losses must

42 COMPLEX REFRACTIVE INDEX OF ICE FOG AT A RADIO WAVELENGTH OF 3 MM

arise in practice due to mirror alignment errors and surface irregularities in the metal optics due to machining and grinding a more reasonable total loss is taken to be  $1.0 \times 10^{-2}$ .

For this experiment, a "practical" FPS size would be a mirror-to-mirror separation of 72 in. (corresponding to a semi-confocal mirror-to-flat separation of 36 in.). For these data, the design  $Q$  can be calculated. Thus,

$$Q = \frac{2\pi b}{a_T \lambda} = 186,000.$$

A  $Q$  of 186,000 implies an effective path length of

$$\frac{Q\lambda}{2\pi} = 91.5 \text{ m.}$$

It is obvious from this relationship why a high  $Q$  is desirable for increased measurement sensitivity.

With a mirror-to-mirror separation of 72 in. (confocal), the optimum mirror radius for  $N = 1.0$  is found from the relationship

$$\frac{a^2}{b\lambda} = 1.0.$$

Thus  $a = 75.15 \text{ mm}$

or a diameter of 5.92 in.

This completes the theoretical considerations appropriate to the design of the semi-confocal FPS for an operating wavelength of 3.09 mm.

The spherical mirror, as previously indicated, was made from a 6-in.-diam section of aluminum rolled stock. Initial forming and shaping of the mirror was done on a lathe, with final grinding and polishing done in an optical laboratory. Since facilities and equipment existed for grinding and polishing telescope mirrors for a 72-in. radius of curvature (36-in. focal length), this was set as the design parameter.

Deviation from a true spherical surface is measured by an optical fringe pattern test known as a Ronchi test (Ingalls 1970). A true spherical surface gives a fringe pattern consisting of alternating straight light and dark bands across the visual surface of the mirror. Bowed bands indicate varying degrees of parabolism and hyperbolism of the surface. This mirror was found to give a nearly perfect straight fringe pattern, with only a slight tendency toward parabolism.

The flat plate was machined on the lathe from a 1/2-in.-thick copper sheet to a tolerance of  $\pm 0.005$  in. The final diameter of the flat was about 8.5 in., which is certainly much larger than required by the beam waist diameter. RG-99 waveguide coupling feeds were brought through the back of the flat mirror and located symmetrically about the center line of the cavity, with a guide-to-guide separation of 1.5 in.

Figure 28 shows the completed cavity mounted on an optical bench and installed in the environmental chamber.

Details of the cavity  $Q$  measurements and response are delayed to Chapter VII, pending details of the electronic phase locking and frequency sweeping technique described in the following chapter.

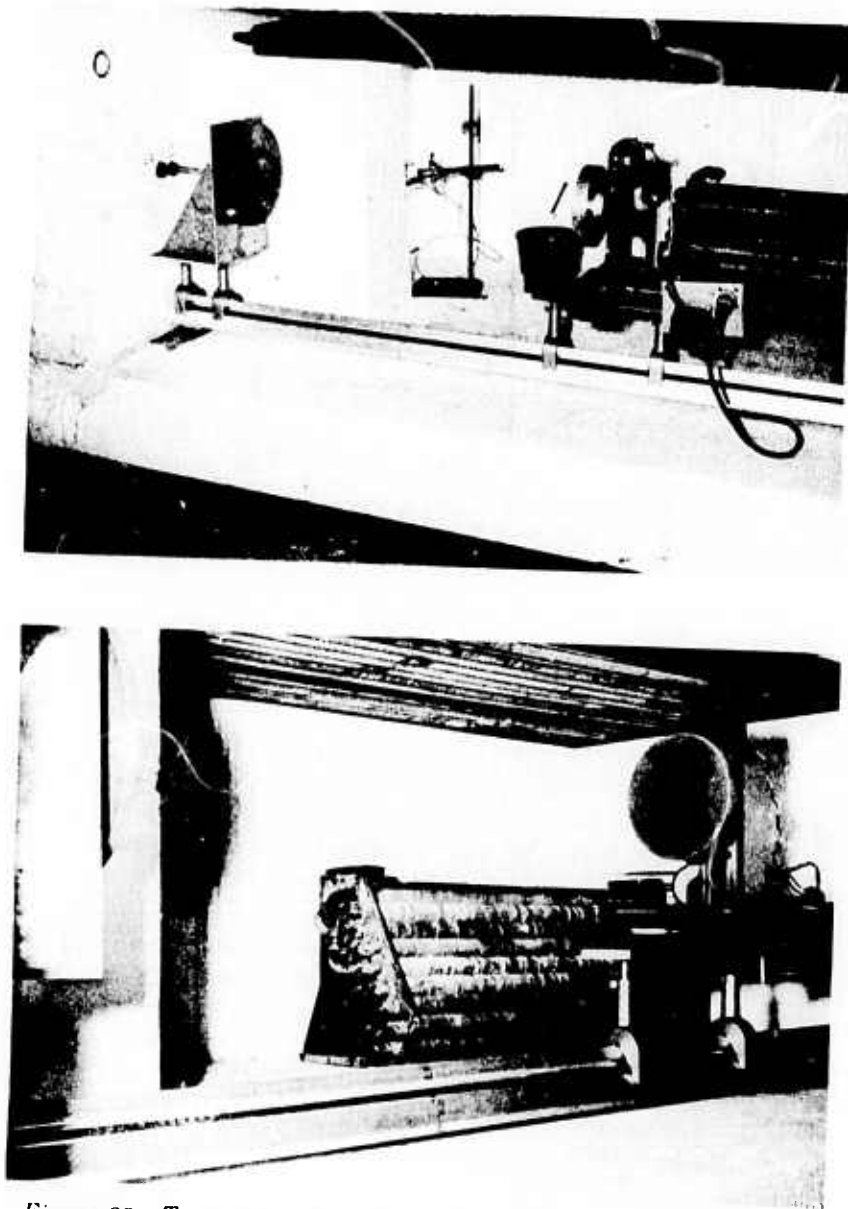


Figure 28. Two views of cold chamber interior, showing details of evaporator mounting and FPS placement.

## VI. INSTRUMENTATION

### Electronic frequency locking system

In order to extract information about the complex permittivity of the cavity medium, two fundamental measurements of the cavity response are necessary: the frequency shift and amplitude (or  $Q$ ) change.

The task of making frequency shift measurements as small as a few kilohertz at 97 GHz is not a trivial one. The classic solution to accurate frequency measurements in the millimeter spectrum is to sweep the klystron reflector with a linear sawtooth voltage of sufficient amplitude to change the klystron operating frequency by several megahertz. A sample of the klystron output is taken

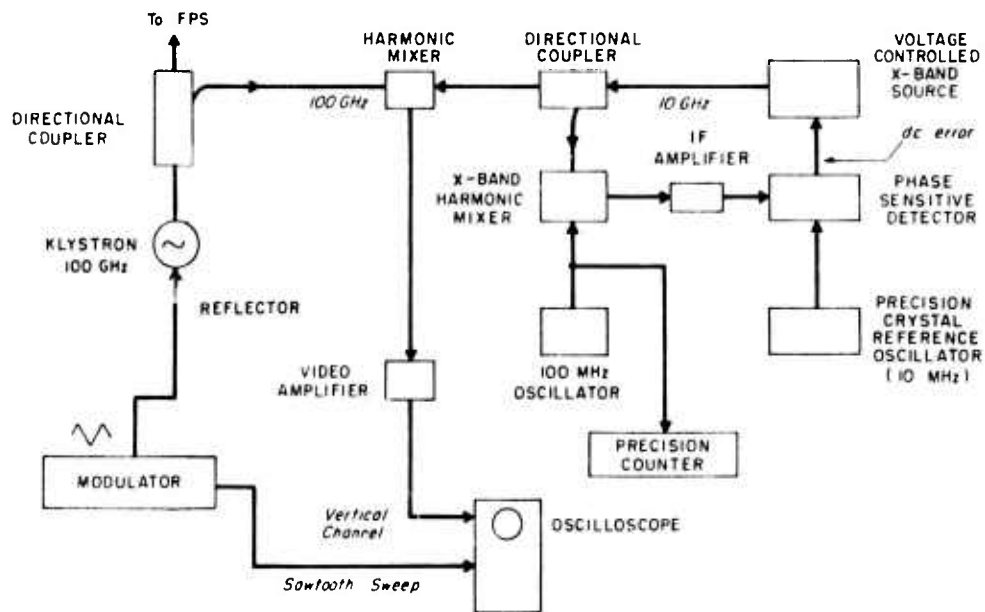


Figure 29. Block diagram of classical millimeter-wave frequency measuring system using variable-frequency markers.

from a directional coupler and routed to a harmonic mixer. The other input to the harmonic mixer is typically an accurately known submultiple of a frequency in the range of the klystron. This lower frequency signal is usually established by an X-band phase-locked source referenced to a free running oscillator near 100 MHz. Since the 100-MHz oscillator frequency can be measured with a high degree of precision, the frequency of the X-band source can be established with the same degree of precision. Beats between the swept klystron and multiples of the X-band source establish frequency "bench marks" appropriate for calibration and measurement of the high frequency klystron source. Varying the frequency of the 100-MHz oscillator "moves" the marker on the oscilloscope, thus establishing a calibration of the frequency scale. This system is diagrammed in Figure 29. The principal disadvantage of this system lies with the stability of the essentially free-running high frequency klystron. Modulator amplitude stability, klystron filament temperature, and klystron beam and reflector voltage changes all contribute to drift in the  $Q$ -curve displayed on the oscilloscope.

Another technique for phase-locking klystrons employs a fixed low frequency oscillator whose signal is harmonically multiplied up to the klystron frequency. This harmonic multiple is then mixed with the klystron signal to produce an IF, which is in turn used to phase lock to a reference signal at the same intermediate frequency. The reference oscillator itself may be linearly swept  $\pm \Delta f$  about  $f_0$ . The function of harmonically multiplying the fixed low frequency oscillator signal up to the klystron operating frequency and simultaneously mixing this signal with a portion of the klystron output can be accomplished by one diode. This is no trivial feat, since the low frequency fixed oscillator may run near 2 GHz, and thus this harmonic generator/mixer crystal must generate a significant amount of harmonic energy at the 50th or so multiple and mix this with the klystron output to provide an IF signal. Recent advances in high-performance harmonic mixer diodes have made possible the phase-locking of klystrons to well above 100 GHz. The principal application of this phase-locking system to data has been in the area of millimeter wave radio astronomy for the study of extraterrestrial molecular line spectra (Weinreb 1970). A phase-locking system using this special type of mixer diode was built to take advantage of the extreme stability, simplicity, and precision frequency measurement offered by this technique. The following discussion refers to the block diagram of this instrumentation shown in Figure 30.

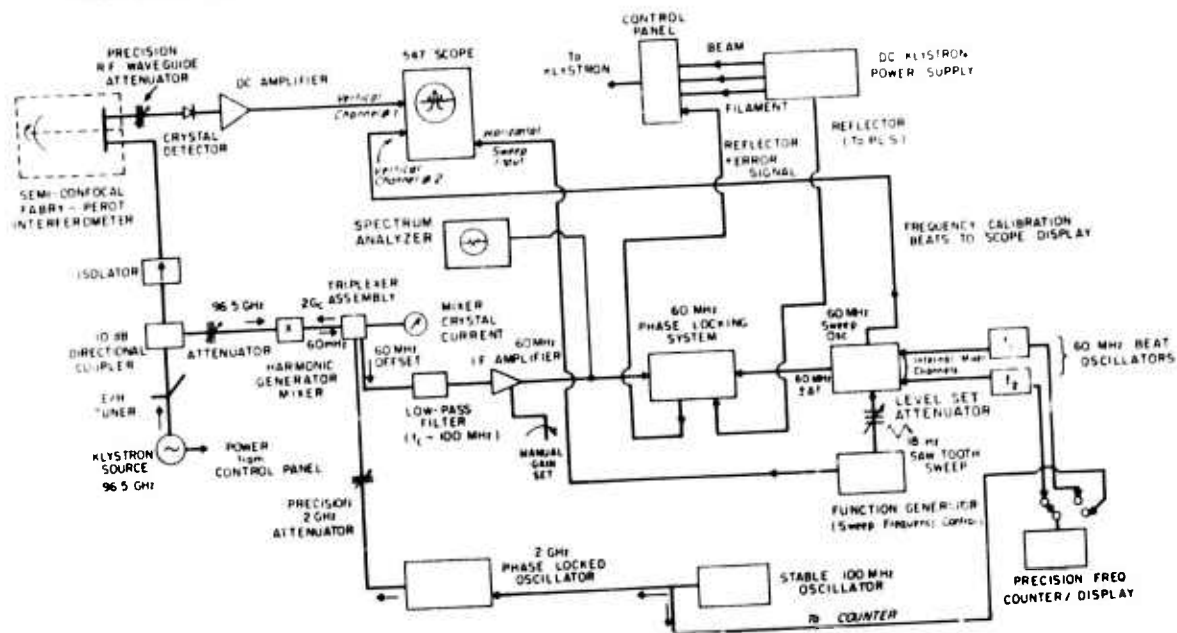


Figure 30. Instrumentation for phase locking and sweeping of FPS cavity at 96.5 GHz.

The output from the Varian VC-713H klystron is sampled by the 10-dB directional coupler and fed, via an attenuator, to the harmonic mixer. An isolator between the directional coupler and the FPS cavity prevents reflections from the cavity from entering the harmonic mixer and causing the system to become unlocked. This harmonic mixer is also coupled by a triplexer assembly to the 2-GHz IF system and a 2-GHz frequency locked oscillator. Precision frequency determination at 2 GHz is no problem since fairly high power ( $\geq 200$  mw) oscillators exist which "lock" to a high multiple of a stabilized 100-MHz source. Since the frequency of a 100-MHz oscillator can be directly counted to six or more significant figures, the 2-GHz locked oscillator output is known with equal precision.

A multiple of this known 2-GHz frequency is generated by the harmonic mixer/generator crystal to mix with the klystron signal. In practice there is no problem in determining which multiple of the 2-GHz oscillator is being mixed since the frequency of the klystron is resolvable to within  $\pm 0.5$  GHz or better by an absorption type wavemeter. The difference between the klystron signal frequency and the frequency generated within the harmonic mixer is the IF. Phase locking is done at the IF frequency since mixers translate amplitude and frequency relationships without distortion to lower frequencies for ease in further processing. A 60-MHz IF amplifier and phase locking system proved convenient for use with this system.

It is the purpose of the triplexer assembly to separate the 2-GHz locked oscillator input frequency from the 60-MHz output IF frequency from the harmonic mixer crystal bias current. Since considerable time was spent in building and optimizing this component for a 60-MHz IF, its circuit details and electrical performance are indicated in Figure 31.

The 60-MHz IF output is first low pass filtered (filter critical frequency = 100 MHz) to further isolate the high power 2-GHz reference oscillator from the IF system, then amplified prior to introduction into the phase locking system.

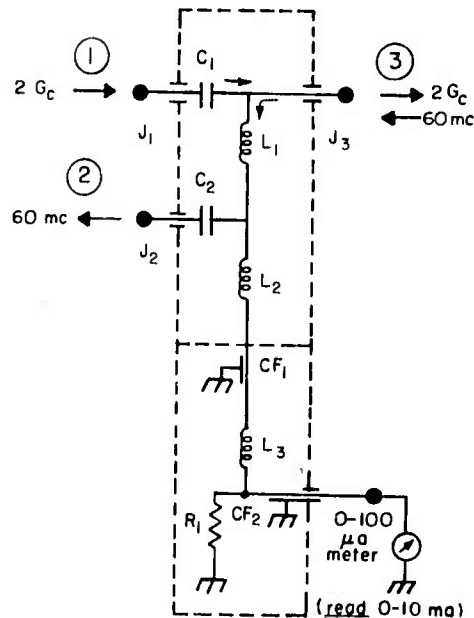
The second reference input frequency to the phase locking system is a 60-MHz signal from a sweep oscillator. The sweep oscillator frequency is  $60 \pm \Delta f$  MHz, and is linearly swept by an

46 COMPLEX REFRACTIVE INDEX OF ICE FOG AT A RADIO WAVELENGTH OF 3 MM

Port (2) - (3) 0.40 dB @ 60 MHz  
 Port (1) - (3) 3.3 dB @ 2.17 GHz  
 measured with HP432A power meter.

Insertion Loss  
 Port (1) - (3) 3.35 dB @ 2.17 GHz  
 Port (2) - (3) 0.514 dB @ 60 MHz

(measured with HP8551B/851B spectrum analyzer)



$C_1 = 2.7$  pf (low ind. cap.) (JFD 2R7C) in parallel with 3.3 pf ceramic

$C_2 = 43$  pf/1000v mica

$CF_1, CF_2 = .001$  mfd feed through capacitors

$L_1 = 10$  turns #24 nyclad wire on 1500 $\Omega$ , 1/2 watt carbon resistor

$L_2 = 180$   $\mu$ h peaking coil

$L_3 = 1$  mh coil

$R_1 =$  meter shunt resistor, 10 $\Omega$  to give 0-10 ma full scale reading

$J_1, J_2 =$  TNC female connectors

$J_3 =$  American #26805

Components mounted in 2-chamber milled aluminum box with interior compartment sizes 1.2" wide x 1.55" long x 0.68" deep.

Figure 31. Triplexer assembly.

external sawtooth function generator. This sawtooth voltage is also used to control the sweep of the horizontal time base of the oscilloscope. The sweep oscillator has an internal mixer and provisions for external input sources to be added to the mixer. Thus marker pips are generated by the sweep oscillator frequency at frequencies corresponding to the external oscillator frequencies. These pips are displayed on one of the vertical channels of the oscilloscope and, by adjusting these pips to correspond to the half-power points of the cavity response and to the peak of the  $Q$ -curve, the cavity  $Q$  and frequency shift can be accurately measured by the difference in frequency of these 60-MHz reference oscillators. In practice, frequency measurement to within a few hundred cycles precision is possible at an operating frequency of 97 GHz.

Since the output of the phase-sensitive detector is a dc error voltage which is added to the klystron reflector voltage, the klystron frequency is electrically tuned in a direction to minimize this dc error signal. The effect of this is to phase lock the klystron in such a way that it is swept  $\Delta f$  in frequency by the 60-MHz sweep oscillator.

Whether the klystron frequency is above or below the reference frequency by the IF frequency can be resolved by observing the lock points as the klystron reflector voltage is increased and/or decreased.

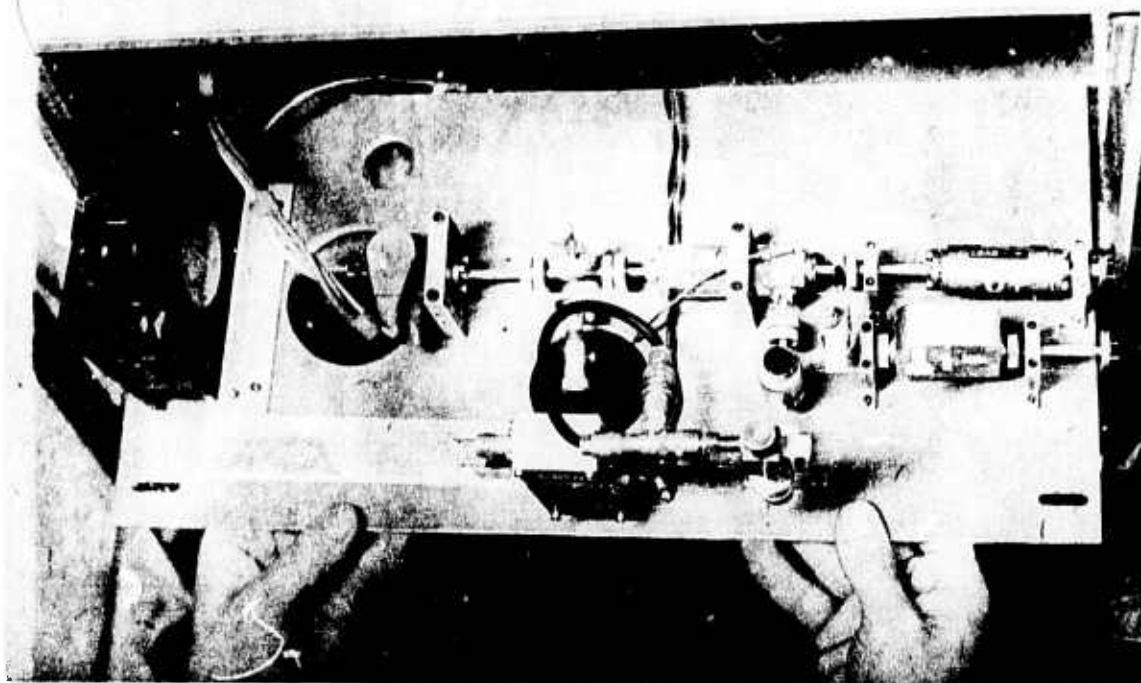


Figure 32. View of electronic hardware associated with klystron phase locking system.

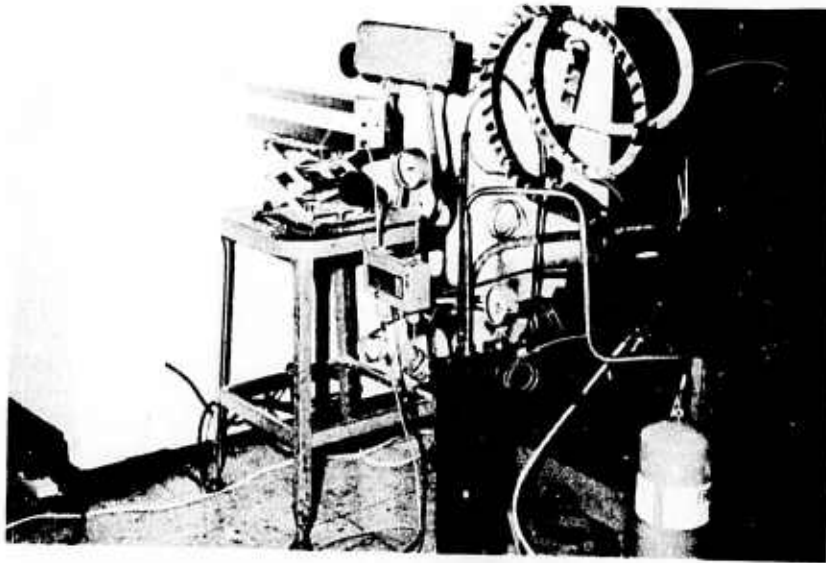
A waveguide feed couples the cavity to an ordinary millimeter wave crystal video detector to sample the cavity response. This signal is coupled to one of the vertical channels for visual presentation and measurement of cavity response. Between the crystal detector and the flat plate a precision RF power attenuator is located for calibration and test purposes. Figure 32 is a view of the microwave plumbing, including the triplexer and harmonic mixer assembly.

#### **Environmental chamber and refrigeration system**

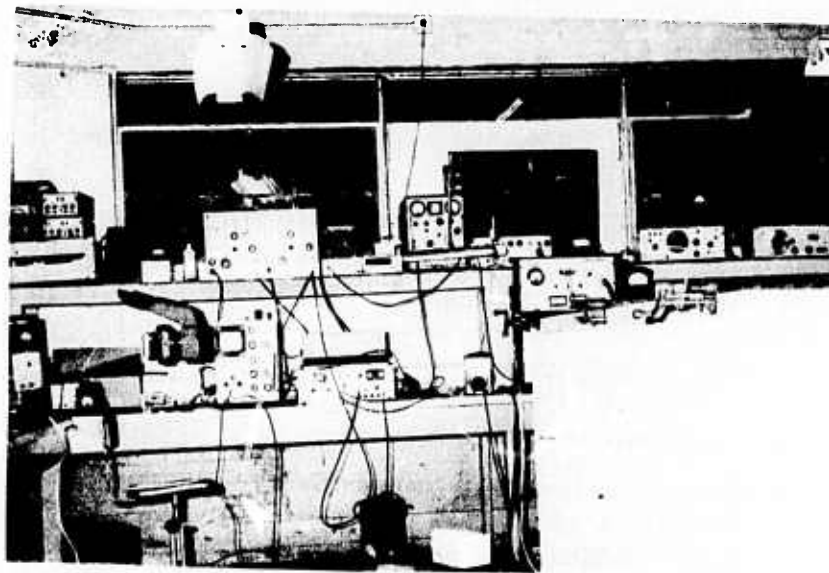
The environmental system consists of a Styrofoam chamber of interior dimensions 6 ft 8 in.  $\times$  4 ft  $\times$  21.8 in. The wall thickness of this chamber is 8 in., and access to the interior is gained through the front side which is held to the chamber by six screw-type extension clamps. This method of securing the door provides a maximum access area, quick entry, and a minimum amount of heat leakage.

The refrigerant evaporator system consists of two parallel evaporators, each with its own independent evaporator control valve. Each evaporator consists of approximately 72 ft of  $\frac{5}{8}$ -in.-diam copper pipe with aluminum "disk" fins  $1\frac{1}{4}$  in. in diameter and a fin radiator density of 8/in. One evaporator is 6 ft 5 in. long by 3 ft wide and is mounted on Styrofoam support blocks which hold it near the chamber roof. The other evaporator is more compact, consisting of three stacked coils surrounded by a fan shroud, and is mounted at one end of the chamber. The fan, a 600-cfm squirrel cage type, draws air over this set of coils and discharges this air upwards and over the roof evaporator coils. This fan provides a considerable amount of air circulation within the chamber.

The optical bench, containing the Fabry-Perot cavity, sits on the floor of the chamber with the flat mirror mounted near one end wall. Waveguide runs through the chamber walls to connect the



a. View of refrigeration system. Laser is seen mounted on chair.



b. Partial view of chamber and electronics.

Figure 33. Further details of environmental chamber and peripheral equipment.

millimeter wave electronic components to the Fabry-Perot. Figure 28 is a front view of the chamber looking in on the system. Figure 33 is an overall view of the chamber and a partial view of the electronics. The access port, visible in the door, is shown in this photo. Figure 34 is a sketch of the interior floor plan of the chamber. Note that in this sketch the laser beam is shot through the chamber in parallel with the door and alongside the FPS cavity. Entrance to and from the chamber by the laser beam is obtained by 1½-in.-diam Lucite tubes sealed at each end with clear slide cover glass and containing several ounces of calcium sulfate, a good dessicant. Thus no moisture will condense on the interior glass covers as the temperature is lowered, and there is no scattering or diffraction of the beam except by the ice fog aerosols. A photocell detector and dc amplifier drive

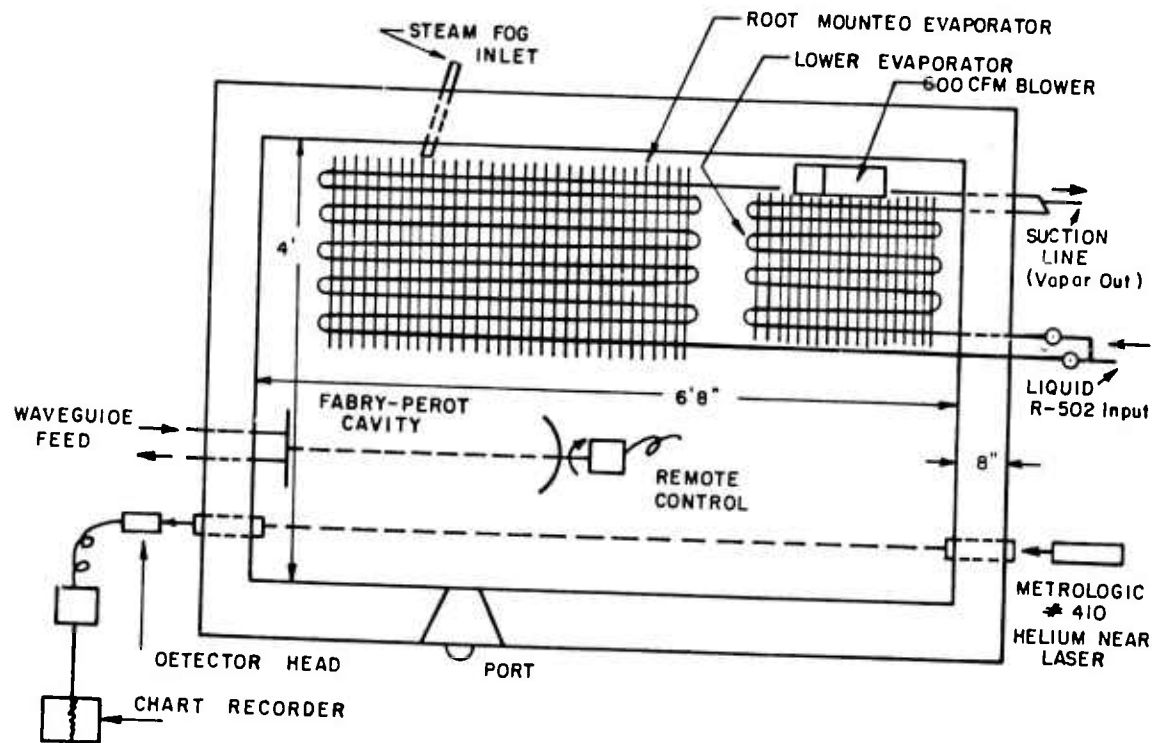


Figure 34. Environmental chamber floor plan and equipment layout.

a chart recorder which is used to continuously monitor the  $6328 \text{ \AA}$  laser amplitude level. The optical detector output current is proportional to input power, hence the laser extinction may be found from

$$\text{dB loss} = -10 \log \frac{I_0}{I}$$

$I_0$  = no-fog quiescent output current as shown on chart paper

$I$  = reduced output current due to fog scattering and absorption effects.

Figure 35 shows the change in output current due to a 3-dB change in path absorption. From this figure, it is clear that the optical detector is indeed "square law," and hence the above relation is true. This 3-dB calibration check was accomplished by passing the laser beam through a 0.3 normal density optical filter borrowed for this purpose.

The refrigeration equipment consists of a single-stage 3-hp Copeland condensing unit (Model 94-A) which drives the paralleled evaporators within the chamber. Each evaporator is fed through its own separate expansion valve, as each expansion valve has its own separate thermostatic bulb thermometer attached for continuous temperature readout. Thus each evaporator may be "balanced" by adjusting the valves to give the same or nearly the same refrigerant evaporation temperature.

Optimum system capability is achieved (empirically) by adjusting these valves in combination until the suction line input pressure is -5 in. of mercury (vacuum). Refrigerant 502 was chosen as the working fluid for this system as the best compromise between low-temperature capability, system compatibility (the original compressor was designed for R-22 use), and economy.

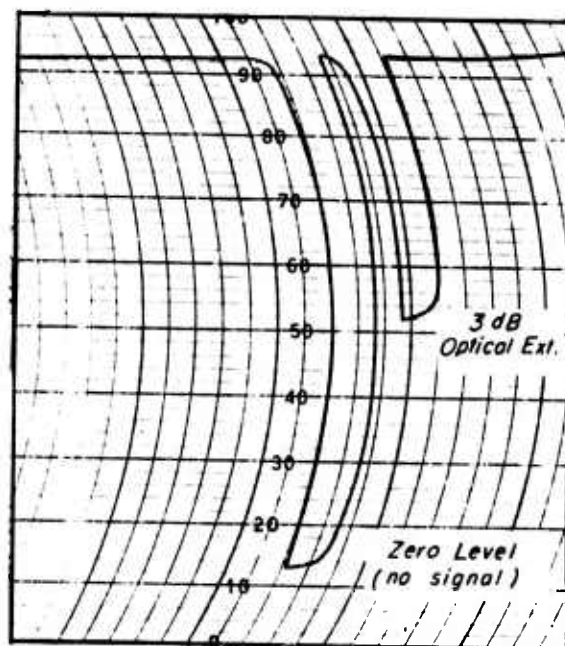


Figure 35. Laser extinction due to 0.3 normal density optical filter.

Temperature control of the chamber was achieved by adjustment of the pressure-sensitive switches on the inlet and outlet lines of the compressor. While not designed to function as a thermostat, these limit switches in fact work quite well for this since there is an explicit relationship between evaporator temperature and evaporator pressure for each type of refrigerant used. This system does not allow for rapid changes in setting the chamber temperature, but after the appropriate pressure settings for each desired chamber temperature were experimentally found, this technique would hold the temperature constant within  $\pm 1^\circ\text{C}$  for all settings used.

Warm fog was admitted in controlled amounts to the chamber through a slim glass pipe in one wall. This fog was generated in a teapot on an electric heater (Fig. 36), and seemed to produce a much steadier, more uniform fog than earlier techniques which were tried. Fog was added to the chamber only after electrical and temperature stabilization was achieved (meaning, generally, only after several hours of operation), and in measured amounts. A crude measurement was achieved by timing the fog admission time with a stopwatch. Five to ten seconds would be sufficient to produce a very dense fog, which was mixed and dissipated by operating the internal chamber fan. Generally this mixing/dissipation was done until the laser level returned to within  $-3$  dB of its initial level. This level of operation was chosen since this fog density provided for an easily observed cavity frequency shift and satisfactory impactor measurements, and compared with a known calibrated extinction point (the 0.3 ND optical filter) of the laser on the chart record.

Once the desired fog density was reached (by observing the chart-recorded laser level) both fan and compressor were shut off to minimize vibrational effects on the cavity operation. All mechanical operations were stopped whenever a photographic record and/or frequency measurement was made. At this level, an oscilloscope picture was made of the cavity response to compare with the no-fog cavity response. Interestingly enough, for the small amount of steam fog admitted, the chamber temperature changed very little from its no-fog condition. This change was at most  $2^\circ\text{C}$  and typically  $1^\circ\text{C}$  or less, which is an adequate testimonial to the low temperature capacity of this system.

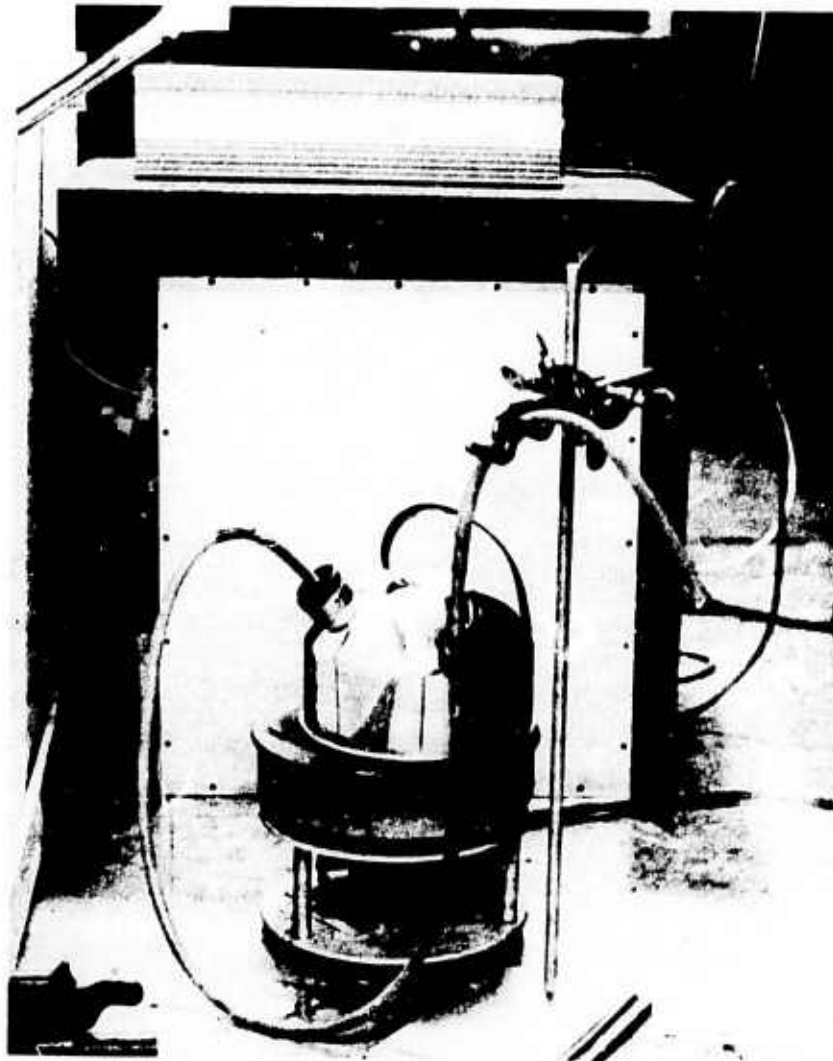


Figure 36. Teapot mode of steam fog production.

## VII. MEASUREMENTS

### FPS operation

Prior to all operations and measurements the klystron and klystron power supply were thoroughly warmed up. All low frequency oscillators, including the 97-MHz reference oscillators and the 60-MHz beat (marker) oscillators were run continuously during the data taking operations. Prior to data taking and measurements in the cold chamber it is necessary to run for several hours at the desired temperature to assure that adequate thermalization in the mechanical parts of the cavity has taken place.

Longitudinal mirror movement was remotely controlled by a motor suitably geared down so as to move the spherical mirror very slowly. Thus, as the air was cooled down and dried out the index of refraction decreased, and hence the resonant frequency of the cavity increased. For air saturated with water vapor at room temperature there is a change of over 100 N-mits as the air is cooled to  $-35^{\circ}\text{C}$  and becomes saturated with respect to ice at this temperature. Rather than disturb the

reference 2-GHz oscillator setting to track the cavity frequency, the spherical mirror was moved by the remote controlled motor to keep the  $Q$ -curve on the oscilloscope.

The reference oscillator frequency controlling the 2-GHz locked oscillator was kept near 97.9213 MHz, and the locked oscillator output was 1762.5834 MHz (corresponding to the 18th multiple of the 97-MHz input). A spectrum analyzer check indicated 1760 MHz. For a multiplicative factor of 55, the klystron frequency is therefore 96,942.087 MHz  $\pm$  1F. An absorption wavemeter check indicated 97 GHz.

The purpose of including the RF waveguide-type calibrated attenuator in the crystal detector waveguide from the FP cavity was to check the square-law characteristic of the detector diode. For a square-law detector, the output voltage of the detector,  $y$ , goes as

$$y = k \cdot v^2$$

where  $k$  = constant, characterized by the amplitude of the sine wave signal divided by the RMS noise amplitude

$v$  = voltage impressed upon the crystal by the input waveform prior to detection.

Since input power is proportional to  $v^2$ , the linear measure of  $y$  is a measurement of the input signal power to the crystal detector.

The square-law character of the video crystal was checked by changing the attenuator setting -3 dB and observing the response on the oscilloscope. The detector law is in fact square-law since the peak of the curve dropped by one-half.

Figure 37 shows two measurements of the cavity  $Q$  made in the open laboratory environment. During this measurement the relative humidity was 35% and the temperature 74°F. The  $Q$  is found from the relation

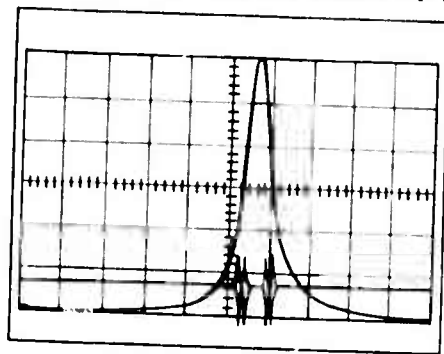
$$Q = \frac{f}{\Delta f}$$

where  $f$  = klystron center frequency,  $\sim$  97 GHz

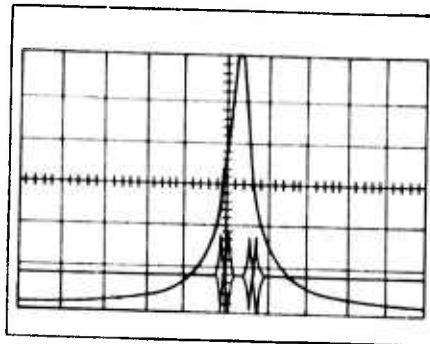
$\Delta f$  = half-power frequency separation.

The beat markers, visible at the bottom of the photographs, were set to correspond to the right- and left-half power points of the  $Q$ -curve by adjusting the frequencies of the two 60-MHz marker oscillators. The variation in the  $Q$  between these two curves is attributed to the difficulty of setting these marker oscillators exactly at the half-power points.

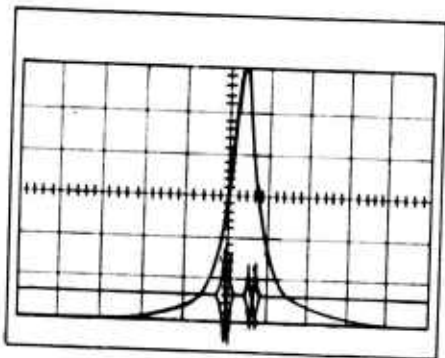
Figure 38 shows the cavity response curves in the cold chamber at a temperature of  $-35^\circ\text{C}$ . The video amplifier gain and the horizontal sweep width (the  $\Delta f$  of the 60-MHz sweep generator) were reduced to bring the curve down to full scale on the oscilloscope and spread the curve out for increased  $Q$  measurement accuracy, respectively. Still, it is difficult to accurately measure the cavity  $Q$  because of this difficulty in determining the marker separation. However, the cavity  $Q$  in a cold, dry environment was taken to be 140,000, in good agreement with the theoretical cavity  $Q$  of 186,000. Undoubtedly this measured  $Q$  would have been higher but the mirror vertical travel slide hit the upper stop before the amplitude of the  $Q$  curve peaked. No effort was made to remount the mirror so as to increase the available travel because of the time limitations placed upon some of the borrowed equipment.



$Q = 100,500 \quad \Delta f = 0.9660 \text{ MHz}$

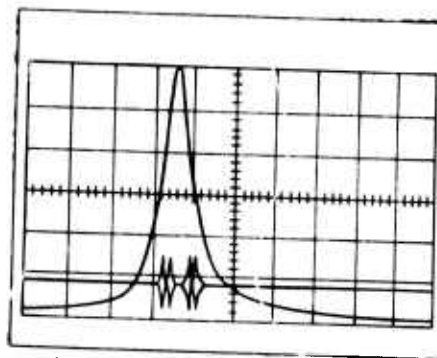


Cavity response in dry, cold chamber ( $-35^\circ\text{C}$ ),  $\Delta f = 0.6619 \text{ MHz}$   $Q = 146,500$



$Q = 107,000 \quad \Delta f = 9081 \text{ MHz}$

Figure 37. Fabry-Perot response curves in laboratory environment (relative humidity 35%, temperature  $74^\circ\text{F}$ ).



Cavity response in dry, cold chamber ( $-35^\circ\text{C}$ ),  $\Delta f = 0.7205 \text{ MHz}$   $Q = 135,000$

Figure 38. Cavity response curves in dry, cold chamber with no fog.

The extinction coefficient, in  $\text{cm}^{-1}$ , due to the scattering and absorption loss of the dielectric medium, is given by

$$X = \frac{2\pi}{\lambda} \left[ \frac{1}{Q_1} - \frac{1}{Q_0} \right]$$

where  $Q_0$  = cavity  $Q$  in a cold, dry, fogless chamber

$Q_1$  = cavity  $Q$  after introduction of fog

$\lambda$  = operating wavelength, in cm

with a loosely coupled square-law detector,

$$\frac{Q_0}{Q_1} = \sqrt{\frac{A_0}{A_1}}$$

therefore

$$X = \frac{2\pi}{\lambda Q_0} \left[ \sqrt{\frac{A_0}{A_1}} - 1 \right] \text{cm}^{-1}$$

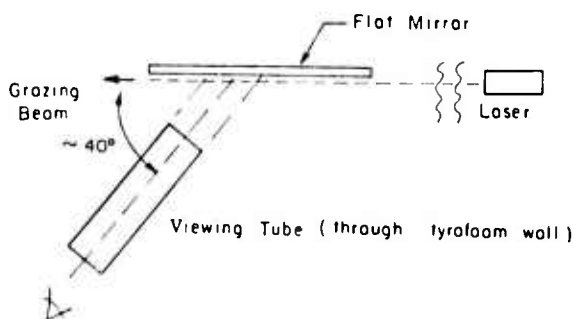


Figure 39. Method for photographing ice particle accumulations on mirrors.

Changes in amplitude are far more accurately and easily measured than changes in  $Q$ . Therefore, loss coefficient measurements are best found in this manner where the amplitudes are directly scaled from the oscilloscope photographs taken.

Since it is possible to read the amplitude of the cavity  $Q$ -response curve on the oscilloscope photographs to about 0.3%, the minimum detectable loss will be about

$$\begin{aligned} \chi_{\min} &= 1.45 \times 10^{-4} \left[ \left( \frac{100.3}{100} \right)^{1/2} - 1 \right] \\ &= 2 \cdot 10^{-7} \text{ cm}^{-1}. \end{aligned}$$

#### FPS mirror effects

The effects of ice accumulation on the cold mirrors was investigated in an empirical manner. Several schemes were attempted and discarded in an effort to measure mirror ice accumulation. Direct photography of the mirror surfaces invariably was inconclusive for any viewing condition with white light. However, a technique whereby red-sensitive film was used to photograph laser scattering due to small particles on the mirror surface worked surprisingly well for accumulation and documentation studies.

With this technique, a laser beam is directed tangentially across the flat mirror and so adjusted that there is only the barest grazing contact with the mirror. When so adjusted the beam itself leaves no visible trace across the mirror. However, dust particles on the mirror surface too small to see directly with the unaided eye cause a distinct and highly visible amount of light scattering. Photographic exposures of this light scattering effect are made through a 2-in.-diam Lucite tube penetrating through the Styrofoam wall and sealed at each end with clear slide glass. Frost formation on the interior glass cover is prevented by the addition of a small amount of drying compound,  $\text{Ca}_2\text{SO}_4$ . The viewing tube is so positioned that about a 3½-in. length of the grazing beam on the mirror is visible, and the scattered light to the viewer is at an angle of about 40° from the forward direction. Figure 39 is a sketch of this arrangement.

With this viewing technique it is easy to see that dust in the air is amazingly abundant. A clean mirror surface does not stay that way for long. Any passing air current carries with it dust which builds up a rapid accumulation, and in a short period of time these dust particles sticking to the mirror "paint in" a solid red line.

A relative size calibration can be had by dusting the mirror surface with a 3- $\mu$  polystyrene dust and photographing the scattered light. Figure 40a shows a clean mirror surface. Several dust grains



Clean, dust-free mirror.



3 $\mu$  polystyrene "sphere" dust on mirror.



Chamber temp -48°C, no fog, about 10 dust particles visible.



Chamber temp -46.5°C, picture made 4 minutes after steam fog introduced in chamber—about 43 particles visible.

Figure 40. Photographs made from 6328 Å light scattered by particles on mirror surface.

are visible in the right center. Figure 40b is a photograph of this same surface very lightly dusted with the 3- $\mu$  polystyrene dust. This dusting was accomplished by putting a small amount of the polystyrene dust on a piece of clean tissue and shaking the tissue about 6 in. in front of the mirror. While it was strikingly visible in the photograph, this amount of dust was almost undetectable to the eye over other parts of the mirror. Some clumping is evident, as seen by the larger areas of scattered light, but it is clear that this technique is quite sensitive to detecting light scattering from small particles. The mirror was then cleaned as well as possible, and the chamber temperature lowered to -47°C. Figure 40c is a picture of the mirror taken at this temperature with no fog having been admitted to the chamber. Dust from the interior of the chamber, stirred up by the evaporator fan, is clearly seen. Figure 40d was made about four minutes after a dense ice fog was formed in the chamber. The accumulation seen here formed very quickly after the admission of the warm steam fog, and no further accumulation was noted as time went on, even though the fog remained optically quite dense for better than eight minutes. It is clear that the fog, while still in the liquid state, will adhere to the mirror and freeze, but once frozen the ice fog crystals bounce off the cold surface. This effect was noted as the fog particles became visible in the beam, recoiled from the surface, and disappeared out of the beam. The freezing time for these small droplets at this temperature is apparently quite rapid. If a measure of the freezing time can be had by measuring the accumulation time during which the particles will adhere to the mirror, then the steam fog is largely crystallized within 5 seconds of admission.

The cavity response was undisturbed by a thick polystyrene dust coat on the mirror. Polystyrene dust was applied to the mirror until a thin white coat covered the surface. Figure 41 is the FPS response curve made before and after this dust was applied. There is no visible change in the  $Q$ -curve. The same sort of effect was later noted with a thin film of frost on the mirrors. This frost, brought on by applying warm, moist air directly to the cold mirrors, had no discernible effect on the cavity response. However, any degree of liquification of the frost caused the cavity amplitude response to die out dramatically. This same effect was previously demonstrated during some early experimentation with this cavity (Fig. 42).

#### Ice fog particle measurements

Physical measurements of the ice fog were made separately from the electromagnetic measurements. These measurements of the particle sizes and densities were made at the same temperatures

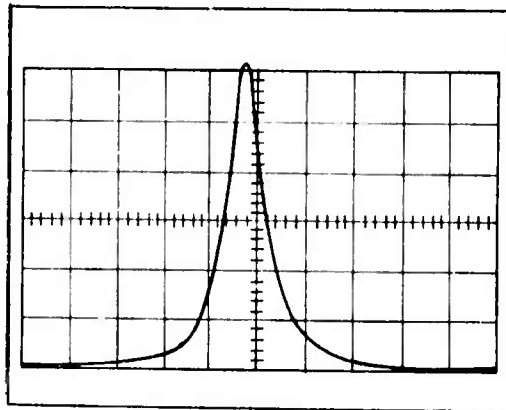


Figure 41. Liberally dusting mirror with 3- $\mu$  polystyrene dust produces almost no effect.

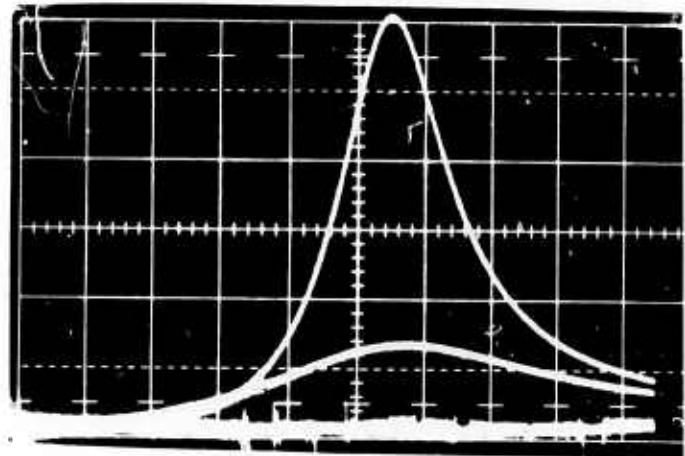


Figure 42.  $Q$ -perturbation due to a thin film of water on mirror surface (expanded  $s'$  sep).

as electromagnetic measurements of the fog were made, i.e.  $-30^\circ$ ,  $-35^\circ$ ,  $-39^\circ$ ,  $-43^\circ$  and  $-47^\circ\text{C}$ . These fog measurements were made at or near the  $-3\text{-dB}$  extinction level which was taken to be the standard operating point for each fog and electromagnetic measurement. Thus all measurements over the temperature interval above are referenced by the common laser extinction level. This laser level, as mentioned earlier, was chosen because of the calibration established by the known transmission of an optical filter, as well as its effect in producing a visible change of the cavity response.

A UNICO four-stage cascade impactor was used to collect fog samples for study. This impactor uses two glass slides, coated with magnesium oxide, as impact areas for the ice fog particles. The magnesium oxide slide coating is formed by holding the clean slide over a burning magnesium ribbon (Rothman and Ledbetter 1968). This impactor is so constructed that it contains a sequence of four internal knife edges over which the sample volume of air containing the aerosol is drawn. These knife edges are seriesed, and each edge is closer to the slide than the preceding knife edge. In theory, the most massive aerosol particles have too great a momentum to make the turn with the airstream around the first sharp edge. Their momentum sends them crashing into the magnesium oxide layer to leave a crater, the size of which is a measure of the size of the ice fog particle. The aerosol particles are "sized" stage by stage in this manner, with the fourth stage collecting the smallest particles. A rotometer and stop watch are used to determine the volume of air drawn through the impactor, and from a count of the number and sizes of the impact craters a number-density distribution can be found.

While in theory this measurement technique sounds simple, in practice it is subject to many errors which make these counts unreliable. Since this device is hand-controlled and -operated, it is clear that each individual's technique and skill directly affects the final count. The average of a limited number of samples was considered as the "best estimate" of the actual fog number-density. The second major limitation of this method centered around the very poor contrast of these fog particle craters in the magnesium oxide film. Figure 43 shows a photomicroscopic picture made of a given impact area. Fatigue after several hours of close study was undoubtedly responsible for some error. The third area for measurement error involves the collection efficiency of the impactor. No published data were found which attempted to answer this question. The collection efficiency,

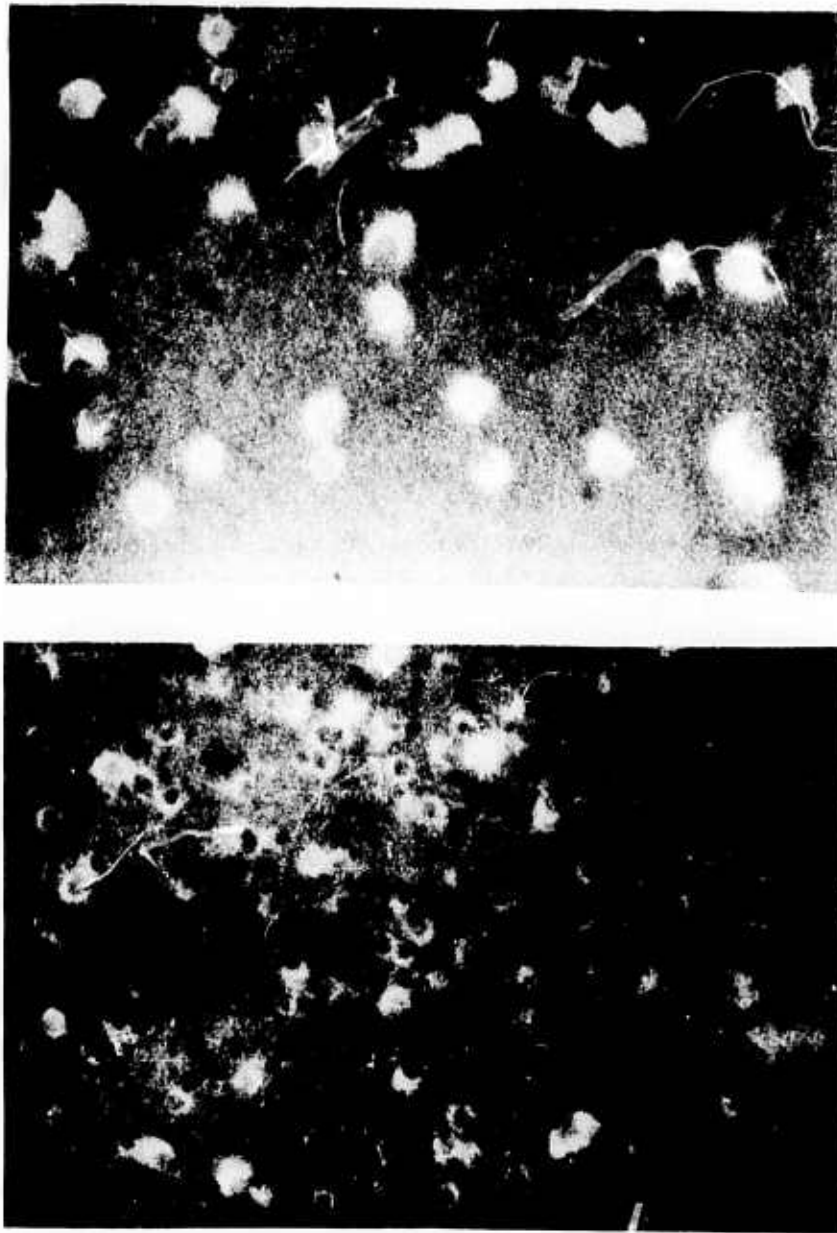


Figure 43. Photomicrographs of  $10\ \mu$  (upper) and  $7\ \mu$  (lower) craters left by ice fog particles on a magnesium oxide slide.

especially for the smallest particles, must certainly be poor since on several slides there were definitely traces of craters smaller than about  $4\ \mu$  diameter which were of too poor a contrast to count. Attempts to improve their readability by depositing thicker and thinner magnesium oxide coats did not help, nor did efforts at staining the slide. The meteorology group at the U.S. Army Cold Regions Research and Engineering Laboratory uses a single-stage impactor which samples  $10\ \text{cm}^3$  of volume and causes the aerosol particles to impact upon a small area on a glass slide containing a drop of silicon oil. A photomicroscopic picture thus "sees" the entire particle collection, and can later be enlarged for counting. However, this technique requires that the ambient temperature be below freezing before and during the time the particles are being photographed to prevent particle evaporation. This was clearly not possible for this experiment, thus ruling out this technique.

Table VI. Measured particle diameter (number/cm<sup>3</sup>).

Experiment no.	<7 $\mu$	7-12 $\mu$	12-19 $\mu$	19-26 $\mu$	>26 $\mu$	N total	Laser extinction (6328 Å)(dB/m)
<b>T = -47 ± 0.5°C</b>							
1	-	121	13	3.73	1.12	189	1.33
2	-	155	4.15	0.218	-	159	1.16
3	29.50	164	8.62	0.144	0.088	202	1.20
Avg	10	164	8.6	1.4	.406	183	1.23
% N <sub>T</sub>	5.5	89.5	4.7		.3	183	-
<b>T = -43<sup>+</sup><sub>-1.0</sub> °C</b>							
10		167*	12.2			179	1.42
11		162*	6.35			168	1.50
Avg		165*	9			174	1.46
% N <sub>T</sub>		94.8*	5.2				
<b>T = -39 ± .5°C</b>							
8		151.2*	12.7			163.9	1.46
9		174.5*	1.52			176.0	1.42
Avg		163*	7.1			170	1.44
% N <sub>T</sub>		96*	4			-	
<b>T = -35 ± .5°C</b>							
4	-	85.5	17.2	0.58	1.26	104.6	1.37
5	-	164	76.4	3.25	0.8	244.5	1.33
6	-	117	48	.58	1.2	166.8	1.14
7	10.7	74	10.2	4.6	.59	100.1	1.04
Avg	2.68	110	38	2.25	.96	154.2	1.24
% N <sub>T</sub>	1.68	71.3	24.7	1.46	.624		
<b>T = -30°C</b>							
	18	96.2	15	4		133.2	1.45
	<6 $\mu$	6-12 $\mu$	12-20 $\mu$	>20 $\mu$			
	216	37	32	32		317	1.50

\*5-12 $\mu$ 

The number densities reported in Table VI are therefore lower limits, particularly regarding the smaller sizes. Table VII is a distillation of the raw numbers appearing in Table VI. Particle diameters reported here were made by comparison of the crater sizes with a microscopic scale (in the microscope eyepiece) calibrated from a stage micrometer.

Several conclusions can be drawn from this work. From these tables it is clear that the large-size ice fog particles are associated with the warmer fogs; the majority (95% or better) of the particles associated with fogs -39°C or lower have diameters less than about 12  $\mu$ . For the same laser extinction, the total number densities of these fogs at all temperatures are comparable. The lowest total number density (100/cm<sup>3</sup>) and the highest number density (317/cm<sup>3</sup>) are for the warmer reported fogs, and the lower temperature fogs had intermediate number densities.

Table VII. Gross statistics.

Temp (°C)	$N/cm^3/dB/m$ 6328 Å	$N_{total}/cm^3$	Particle size distribution (%)		
			5-12 $\mu$	12-19 $\mu$	>19 $\mu$
-30 ± .5	149	217	54	38	8
-35 ± .5	124	154	73	25	2
-39 ± .5	118	170	96	4	—
-43 + .5 - 1.0	119	174	94.8	5.2	—
-47 ± 1.0	149	183	95	4.7	.3

Perhaps the most significant finding of all is the reproducibility of these fogs. For fogs  $-39^\circ\text{C}$  and colder, the measured number densities repeated with excellent agreement from experiment to experiment. What measurement difficulties there were arose with the warmer fogs. In the four experimental measurements made on the  $-35^\circ\text{C}$  fog the number densities varied by as much as a factor of 2.5. The characters of the  $-30^\circ$  and  $-35^\circ\text{C}$  fogs were much different than those of the colder fogs. These fogs would dissipate more rapidly and generally required the admission of more steam fog for formation and mixing. While measured amounts of steam fog at the colder temperatures would generally give a reproducible effect, such was not always the case here. These effects were even more pronounced at  $-30^\circ\text{C}$ , but due to the critical nature of ice fog formation in this temperature interval, no great efforts were made to describe fogs at  $-30^\circ\text{C}$ . However, electromagnetic measurements were made at this temperature at the same laser extinction level as were the lower temperature measurements.

These measured number densities were used as a basis for calculating the laser extinction to compare with the measured extinction. The calculations were made by assuming the ice fog particles were spherical and applying Mie's theory to calculating the absorption and scattering cross sections of each particle size. This procedure, as well as the optical depth calculation, was outlined in Chapter IV. Figure 44 shows five number-density distributions used in these calculations. Curves A and B are more nearly representative of the actual impactor measurements made of these fogs, while C, D and E weight the small particle sizes quite heavily. Table VIII lists the calculated and measured optical properties of these fogs. Table IX tabulates the extinction cross sections for ice spheres from 1 to 35  $\mu$  diameter for 6328 Å laser light.

These calculations indicate several interesting things. First, the small particles are more effective scatterers than the larger particles (not surprisingly). However, a relatively small number of larger particles can contribute significantly to the total extinction (distribution B, Table VII). Secondly, there is a factor of between 3 and 5 difference in the measured and calculated attenuation. Recently other investigators have reported similar results (Munis and Delaney 1972, J. Albertine of the Johns Hopkins Applied Physics Laboratory, private communication). This discrepancy is being studied, but as yet there is no proven explanation.

The principal point here is the obvious difference between the measured and calculated optical attenuation. Three things come to mind as possible explanations: 1) the refractive index for ice at this wavelength is inaccurate, 2) the measured number-densities are wrong, and 3) Mie theory cannot be applied, since these particles may be mostly geometric figures with flat, prismatic faces. While it is certainly true that improved measurements of the complex index of refraction of ice at 6328 Å

Table VIII. Calculated and measured 6328 Å optical properties of ice fog.

Distribution	Total $N/cm^3$	Percentage of particles of diameters (%)			$\tau$ , extinction, $m^{-1}$	Calculated loss, dB/m	Measured loss, dB/m, where appropriate
		<6 $\mu$	6-12 $\mu$	>12 $\mu$			
A	183	6	94	-	.0271	.239	1.23
B	170	29.4	41.2	29.4	.0431	.380	1.24
C	1125	37.8	62.2	-	.0926	.816	-
D	480	64.2	35.8	-	.0296	.261	-
E	4368	87	13	-	.1071	.931	-

Table IX. Optical extinction cross section for ice spheres at 6328 Å  
( $M_{ice} = 1.302 - j 1.9 \times 10^{-6}$ ).

Diam	Total extinction cross section, $Q_{EXT}$	$\frac{Q_{EXT}}{\pi r^2}$	Diam	Total extinction cross section, $Q_{EXT}$	$\frac{Q_{EXT}}{\pi r^2}$
1	$2.56 \times 10^{-12}$	3.26	19	$5.80 \times 10^{-10}$	2.05
2	$8.32 \times 10^{-12}$	2.65	20	$6.64 \times 10^{-10}$	2.12
3	$1.50 \times 10^{-11}$	2.12	21	$7.21 \times 10^{-10}$	2.08
4	$3.02 \times 10^{-11}$	2.41	22	$7.98 \times 10^{-10}$	2.10
5	$3.89 \times 10^{-11}$	1.98	23	$8.76 \times 10^{-10}$	2.11
6	$6.79 \times 10^{-11}$	2.40	24	$9.40 \times 10^{-10}$	2.03
7	$7.72 \times 10^{-11}$	2.01	25	$1.04 \times 10^{-9}$	2.12
8	$1.21 \times 10^{-10}$	2.40	26	$1.08 \times 10^{-9}$	2.04
9	$1.27 \times 10^{-10}$	2.00	27	$1.21 \times 10^{-9}$	2.12
10	$1.81 \times 10^{-10}$	2.30	28	$1.25 \times 10^{-9}$	2.03
11	$1.86 \times 10^{-10}$	1.95	29	$1.40 \times 10^{-9}$	2.12
12	$2.55 \times 10^{-10}$	2.25	30	$1.43 \times 10^{-9}$	2.03
13	$2.64 \times 10^{-10}$	1.99	31	$1.60 \times 10^{-9}$	2.12
14	$3.43 \times 10^{-10}$	2.23	32	$1.61 \times 10^{-9}$	2.01
15	$3.57 \times 10^{-10}$	2.02	33	$1.81 \times 10^{-9}$	2.12
16	$4.41 \times 10^{-10}$	2.20	34	$1.83 \times 10^{-9}$	2.02
17	$4.60 \times 10^{-10}$	2.03	35	$2.03 \times 10^{-9}$	2.12
18	$5.43 \times 10^{-10}$	2.13			

can be made, it is not likely that these new measurements would be radically different from what was reported by Irvine and Pollack (1968) for ice at 1.0  $\mu$ .

In regard to the problem of making accurate fog number-density-measurements, it is worthwhile to quote some of the remarks of Rinehart (1969), who made a study of the methods of measurement for fog drop size distributions. She studied capture and/or replication media which included polyvinyl alcohol, gelatin, oil and magnesium oxide, and concluded that fog drop size distributions were method-dependent and none of the above media was sensitive to or retained for lengthy periods the impressions of small drops. Furthermore, she noted that "lack of correlation between number of captured droplets and visibility was present in even the most careful determinations employing impaction methods."

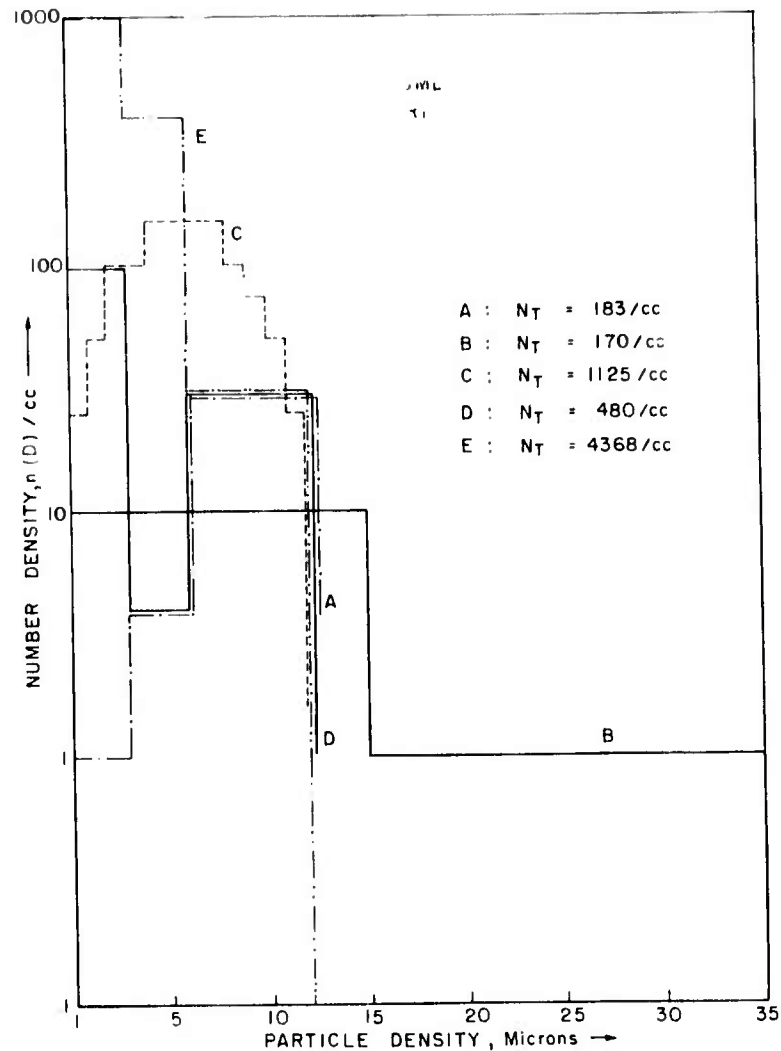


Figure 44. Assumed number-density distribution used in laser extinction computations.

One other sampling effect should be mentioned. The craters, seen in Figure 43, may not accurately reflect the true impacting particle size. A solid spherical particle striking a thin magnesium oxide film would only crush the film down to the point of contact of the particle with the underlying glass. This, in effect, would leave a "crater" smaller than the true size of the particle. This effect, while operative mainly with the larger particles, also indicates that the measured ice volume is really a lower limit to the true ice particle volume per unit volume in the cold chamber.

It is clear from these fog impactor measurements that considerable uncertainty exists about the true ice fog number-density distribution. This is particularly true in regard to the smaller particles (those less than about  $7 \mu$  in diameter) since the impactor registered these particles poorly if at all. There does not exist at this time a method or technique suitable for making an accurate measurement of the fog number-density distribution.

Although desirable, it is therefore not possible to refer the electromagnetic measurements to a fog particle number density. However, a suitable reference fog level is the measured extinction of a 6328 Å helium-neon laser. It was shown that comparable levels of laser extinction give comparable

Table X. Electromagnetic measurements, normalized to 1 dB/m at 6328 Å extinction.

$T$ (°C)	$\Delta f$ (kHz)	$N$	Laser extinction (dB/m)	$N/\text{dB/m}$	$\chi$ , $\text{cm}^{-1}$	$\chi/\text{dB/m}$
-46	228.6	2.36	1.46	1.62	$5.50 \times 10^{-7}$	$3.76 \times 10^{-7}$
-46	238.3	2.46	1.35	1.82	$10.40 \times 10^{-7}$	$7.70 \times 10^{-7}$
-45.5	229.6	2.37	1.46	1.63	$6.25 \times 10^{-7}$	$4.28 \times 10^{-7}$
-46	236.9	2.44	1.42	1.72	$9.55 \times 10^{-7}$	$6.71 \times 10^{-7}$
-46	233.1	2.41	1.46	1.65	$8.70 \times 10^{-7}$	$5.95 \times 10^{-7}$
-46.5	262.1	2.71	1.90	1.43	$4.80 \times 10^{-7}$	$2.53 \times 10^{-7}$
-47	236.0	2.43	1.28	1.90	$5.50 \times 10^{-7}$	$4.30 \times 10^{-7}$
-46.5	260.0	2.68	1.80	1.49	$6.40 \times 10^{-7}$	$3.56 \times 10^{-7}$
-46.5	224.5	2.32	1.17	1.98	$7.25 \times 10^{-7}$	$6.20 \times 10^{-7}$
-42.5	250.5	2.59	1.57	1.65	$9.57 \times 10^{-7}$	$6.10 \times 10^{-7}$
-43	260.9	2.70	1.55	1.74	$10.40 \times 10^{-7}$	$6.70 \times 10^{-7}$
-42.5	340.9	3.52	1.55	2.27	$10.30 \times 10^{-7}$	$6.65 \times 10^{-7}$
-43	298.1	3.08	1.19	2.59	$9.00 \times 10^{-7}$	$7.55 \times 10^{-7}$
-43	203.4	2.10	1.13	1.86	$9.15 \times 10^{-7}$	$8.10 \times 10^{-7}$
-42.5	279.7	2.89	1.40	2.06	$4.94 \times 10^{-7}$	$3.52 \times 10^{-7}$
-42.5	324.4	3.35	1.61	2.08	$7.25 \times 10^{-7}$	$4.50 \times 10^{-7}$
-43	322.5	3.33	1.57	2.12	$13.60 \times 10^{-7}$	$8.65 \times 10^{-7}$
-44	298.0	3.08	1.44	2.14	$5.95 \times 10^{-7}$	$4.14 \times 10^{-7}$
-42	286.8	2.96	1.51	1.96	$4.50 \times 10^{-7}$	$9.60 \times 10^{-7}$
-42	587.0	6.05	2.53	2.39	$10.90 \times 10^{-7}$	$4.31 \times 10^{-7}$
-42.5	331.2	3.42	1.48	2.31	$7.84 \times 10^{-7}$	$5.30 \times 10^{-7}$
-43	261.8	2.70	1.72	1.57	$8.00 \times 10^{-7}$	$4.65 \times 10^{-7}$
-43.5	537.3	5.55	3.00	1.85	$18.90 \times 10^{-7}$	$6.30 \times 10^{-7}$
-43	234.9	2.42	1.25	1.94	$7.25 \times 10^{-7}$	$5.80 \times 10^{-7}$
-39	769.7	7.94	2.76	2.87	$25.4 \times 10^{-7}$	$9.2 \times 10^{-7}$
-39	772.0	7.96	2.92	2.73	$9.0 \times 10^{-7}$	$3.08 \times 10^{-7}$
-39	825.4	8.51	3.03	2.81	$13.1 \times 10^{-7}$	$4.32 \times 10^{-7}$
-38	393.3	4.05	2.13	1.90	$6.95 \times 10^{-7}$	$3.26 \times 10^{-7}$
-38	424.4	4.37	2.02	2.16	$8.70 \times 10^{-7}$	$4.31 \times 10^{-7}$
-38	333.2	3.43	1.61	2.13	$26.8 \times 10^{-7}$	$16.60 \times 10^{-7}$
-37	328.2	3.39	1.35	2.51	$14.50 \times 10^{-7}$	$10.72 \times 10^{-7}$
-38	270.5	2.79	1.28	2.18	$22.8 \times 10^{-7}$	$17.80 \times 10^{-7}$
-38	302.9	3.13	1.24	2.52	$4.50 \times 10^{-7}$	$3.63 \times 10^{-7}$
-37	275.9	2.84	1.28	2.22	$8.85 \times 10^{-7}$	$6.91 \times 10^{-7}$
-38	333.2	3.44	1.59	2.16	$6.95 \times 10^{-7}$	$4.37 \times 10^{-7}$
-39.5	331.8	3.42	1.31	2.61	$15.2 \times 10^{-7}$	$11.60 \times 10^{-7}$
-38	241.9	2.50	1.22	2.05	$18.1 \times 10^{-7}$	$14.80 \times 10^{-7}$
-38	429.0	4.43	1.64	2.70	$5.22 \times 10^{-7}$	$3.18 \times 10^{-7}$
-38	267.9	2.76	1.77	1.56	$8.55 \times 10^{-7}$	$4.84 \times 10^{-7}$
-38.5	361.9	3.73	1.40	2.66	$12.8 \times 10^{-7}$	$9.15 \times 10^{-7}$
-38.5	346.5	3.58	1.51	2.37	$12.9 \times 10^{-7}$	$8.55 \times 10^{-7}$

Table X (cont'd).

<i>T</i> (°C)	<i>N<sub>f</sub></i> (kHz)	<i>N</i>	Laser extinction (dB/m)	<i>N</i> /dB/m	<i>X<sub>v</sub></i> cm <sup>-1</sup>	<i>X<sub>v</sub></i> /dB/m
-33	585.8	6.05	2.25	2.69	$3.64 \times 10^{-6}$	$1.62 \times 10^{-6}$
-35	399.3	4.12	2.07	1.99	$5.44 \times 10^{-6}$	$2.62 \times 10^{-6}$
-34	643.9	6.65	2.88	2.31	$5.32 \times 10^{-6}$	$1.85 \times 10^{-6}$
-35	385.6	3.98	2.31	1.72	$6.36 \times 10^{-6}$	$2.75 \times 10^{-6}$
-35	608.1	6.27	2.88	2.18	$6.75 \times 10^{-6}$	$2.34 \times 10^{-6}$
-34	362.8	3.74	1.86	2.01	$3.06 \times 10^{-6}$	$1.65 \times 10^{-6}$
-35	634.4	6.54	2.55	2.56	$4.55 \times 10^{-6}$	$1.78 \times 10^{-6}$
-34.5	609.3	6.29	2.92	2.15	$3.03 \times 10^{-6}$	$1.04 \times 10^{-6}$
-34	442.7	4.57	2.38	1.92	$4.07 \times 10^{-6}$	$1.71 \times 10^{-6}$
-34	531.6	5.50	3.33	1.65	$6.35 \times 10^{-6}$	$1.91 \times 10^{-6}$
-35	226.5	2.34	1.10	2.12	$3.42 \times 10^{-6}$	$3.11 \times 10^{-6}$
-34	258.3	2.67	1.92	1.39	$3.25 \times 10^{-6}$	$1.69 \times 10^{-6}$
-34	295.5	3.05	2.56	1.19	$6.90 \times 10^{-6}$	$2.70 \times 10^{-6}$
-35	276.8	2.86	2.16	1.32	$4.15 \times 10^{-6}$	$1.92 \times 10^{-6}$
-34	206.1	2.13	1.06	2.01	$4.16 \times 10^{-6}$	$3.92 \times 10^{-6}$
-34.5	637.3	6.57	2.50	2.63	$7.0 \times 10^{-6}$	$2.80 \times 10^{-6}$
-35	270.4	2.79	1.90	1.47	$3.98 \times 10^{-6}$	$2.10 \times 10^{-6}$
-27.5	272.9	2.82	1.57	1.8	$3.92 \times 10^{-6}$	$2.5 \times 10^{-6}$
-29	558.9	5.76	2.07	2.78	$7.95 \times 10^{-6}$	$3.84 \times 10^{-6}$
-30	263.9	2.72	2.31	1.18	$10.1 \times 10^{-6}$	$4.37 \times 10^{-6}$
-30	183.1	1.89	2.44	0.775	$12.6 \times 10^{-6}$	$5.16 \times 10^{-6}$
-29.5	154.8	1.60	1.94	0.825	$9.6 \times 10^{-6}$	$4.95 \times 10^{-6}$
-29	141.2	1.46	1.94	0.754	$10.4 \times 10^{-6}$	$5.35 \times 10^{-6}$
-29	168.7	1.74	1.96	0.890	$5.08 \times 10^{-6}$	$2.59 \times 10^{-6}$
-29	231.2	2.39	1.96	1.22	$5.95 \times 10^{-6}$	$3.04 \times 10^{-6}$
-29	170.0	1.76	1.96	0.9	$9.25 \times 10^{-6}$	$4.72 \times 10^{-6}$
-30	282.7	2.92	1.66	1.76	$4.58 \times 10^{-6}$	$2.76 \times 10^{-6}$
-30	213.5	2.20	1.48	1.49	$4.22 \times 10^{-6}$	$2.85 \times 10^{-6}$

fog impactor number-density measures and, as will be seen in the next section, the electromagnetic measurements correlate very well with the laser extinction level. Thus, the best possible ice fog characterization is obtained by the impactor measurements together with the laser extinction level.

#### Electromagnetic measurements and applications to one-way propagation through ice fog

Sixty-nine different electromagnetic measurements of the complex permittivity of a fog were made covering the temperature range  $-30^{\circ}$  to  $-48^{\circ}\text{C}$ . Recorded simultaneously with the cavity frequency shift and amplitude change was the laser extinction, which was put on chart paper for convenience in future analysis. Chart speed in all cases was  $\frac{3}{4}$  in./min.

Since it is obvious that an accurate measure of the fog number-density distribution is at present impossible to obtain, it is necessary to refer all electromagnetic measurements to some other reference fog level. One such convenient level is the 6328 Å extinction record. The laser extinction,

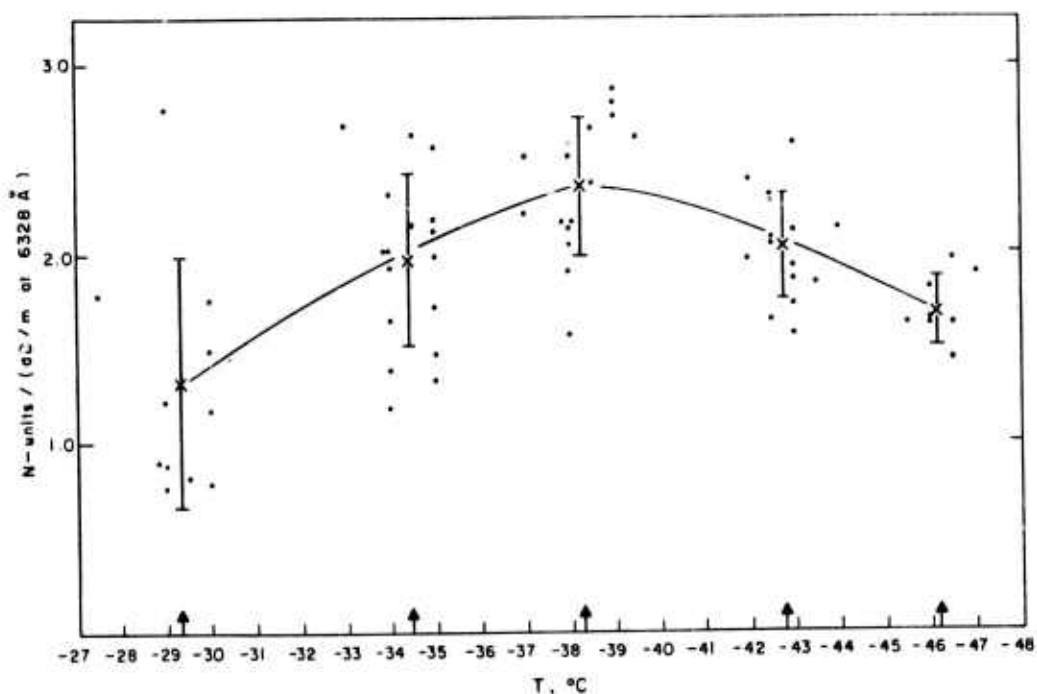


Figure 45. Normalized ice fog N-unit measurements at 97 GHz.

in dB/m, was used to normalize the measured N-unit change of the cavity refractive index and the extinction coefficient  $\chi_0$  of the radio wave in the fog. That is, the units for these quantities are N-units/(dB/m at 6328 Å) and  $\text{cm}^{-1}/(\text{dB/m at } 6328 \text{ Å})$ . The data from these measurements are presented in Table X. Figures 45 and 46 show plots of the normalized N-unit change in cavity frequency and extinction coefficients as a function of temperature. For Figure 45, the standard deviation error  $\sigma$  associated with the spread in the data points decreases with decreasing temperature, dropping from  $\sigma = 0.642$  N-units/(dB/m at 6328 Å) at  $-30^\circ\text{C}$  to  $\sigma = 0.182$  N-units/(dB/m at 6328 Å) at  $-46^\circ\text{C}$ . The standard deviation error  $\sigma$  was computed from the relationship

$$\sigma = \sqrt{\frac{1}{n-1} \sum_{i=1}^n (x_i - \bar{x})^2}$$

where  $\bar{x}$  is the mean value of  $\chi$  or the refractive index found from averaging these experimental measurements. The mean values of  $\chi$  and  $N$  at each temperature interval of interest were found by assuming that the measurements appropriate to these intervals applied to some mean temperature appropriate to that interval. The smaller standard deviation error of the colder fogs is consistent with the fact that the colder ice fogs were much more easily reproduced than their warmer counterparts. However, the refractive index of these ice fogs is relatively constant over the temperature interval  $-30^\circ$  to  $-47^\circ\text{C}$ .

The plot of the extinction coefficient, in  $\text{cm}^{-1}$  (Fig. 46), shows an interesting rise associated with the warmer ice fogs. Since  $-30^\circ$  to  $-35^\circ\text{C}$  is rather critical to ice fog formation, it is reasonable to suppose that some percentage of the ice fog is in the liquid state; either some small percentage of the droplets could be liquid, or some ice crystals could have a liquid coating. By the time that the temperature has dropped to  $-39^\circ\text{C}$  or lower the extinction coefficient has dropped by a factor of 4 or 5 to about  $5 \times 10^{-7} \text{ cm}^{-1}$  (for 1 dB/m of laser extinction). A part of the error associated with the measure of  $\chi$  of the colder ice fogs is the difficulty in accurately reading small

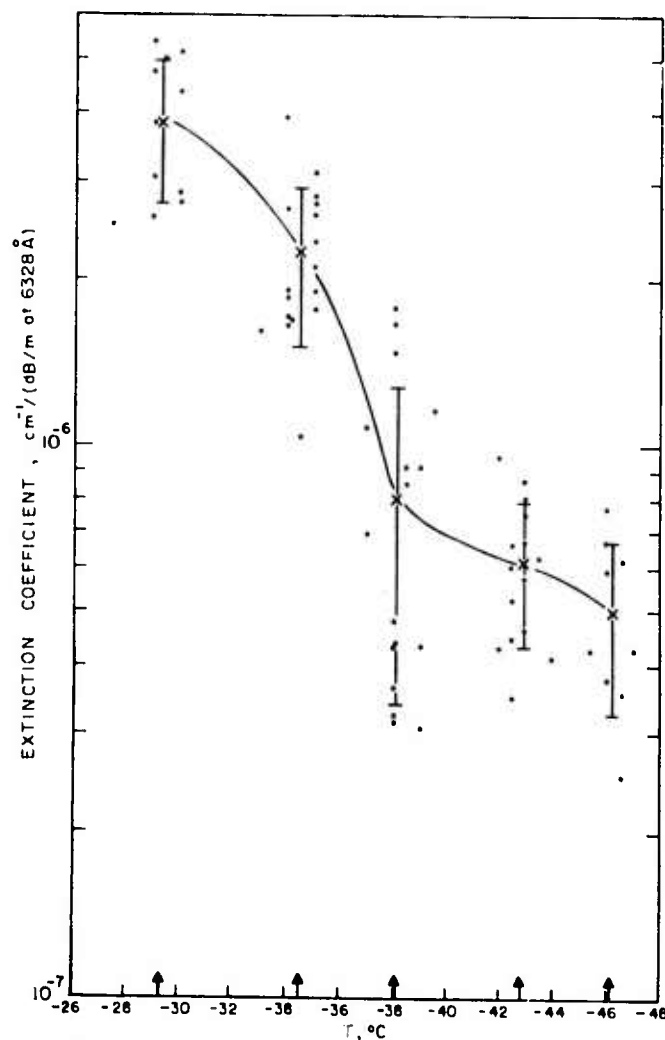
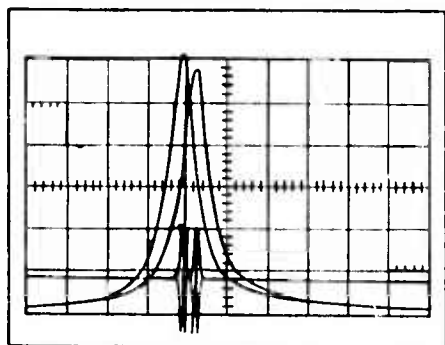


Figure 46. Normalized ice fog extinction coefficient measurements at 97 GHz.

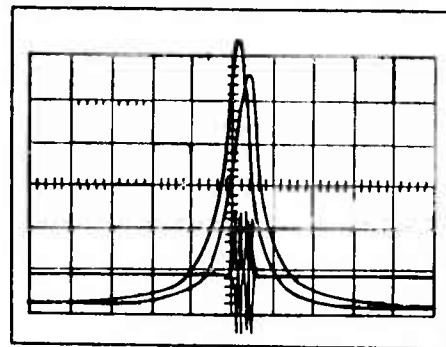
changes in the cavity amplitude response. For this reason, the standard deviation error bars are larger for the colder ice fogs.

Figures 47-56 are traces of the oscilloscope photographs made of the cavity response to these fogs over the temperature interval  $-30^{\circ}$  to  $-48^{\circ}\text{C}$ . Two pictures at each temperature interval of interest were chosen as representative samples. Accompanying each photograph tracing is the section of the strip chart with the laser level at the time the photograph was taken. The original photographs were not of high enough quality and contrast to reproduce directly, which is why tracings of these pictures are included rather than reproductions of the original photographs. The high correlation between the measured laser extinction and the electromagnetic measurements is well demonstrated by Figures 45 and 46.

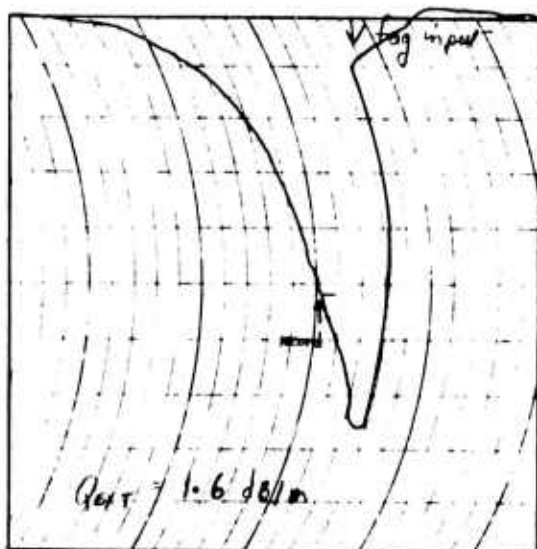
The extinction coefficient  $\chi$ , in  $\text{cm}^{-1}$ , and the change in the refractive index  $\Delta n$  were directly measured. Knowing these two quantities, the propagation constant  $\beta$  in the ice fog can be computed from the relation



$T = -30^{\circ}\text{C}$ ,  $\Delta f = 272.9 \text{ kHz}$ ,  $\alpha = 3.92 \times 10^{-6} \text{ cm}^{-1}$

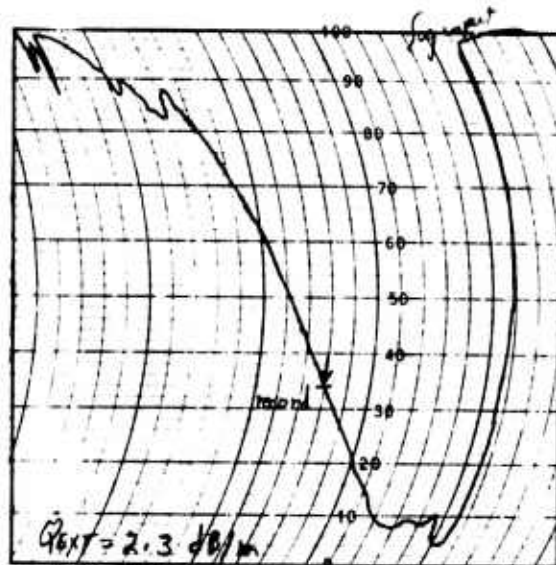


$T = -30^{\circ}\text{C}$ ,  $\Delta f = 263.9 \text{ kHz}$ ,  $\alpha = 10.1 \times 10^{-6} \text{ cm}^{-1}$



LASER EXTINCTION RECORD

Figure 47. Sample cavity response due to ice fog,  $T = -30^{\circ}\text{C}$ .



LASER EXTINCTION RECORD

Figure 48. Sample cavity response due to ice fog,  $T = -30^{\circ}\text{C}$ .

$$\beta^2 = \frac{(n')^2 + \alpha^2 \left(\frac{\lambda_0}{2\pi}\right)^2}{1 + \frac{\alpha^2 \left(\frac{\lambda_0}{2\pi}\right)^2}{(n')^2}} \cdot \left(\frac{2\pi}{\lambda_0}\right)^2$$

where  $n' = 1 + \Delta n$

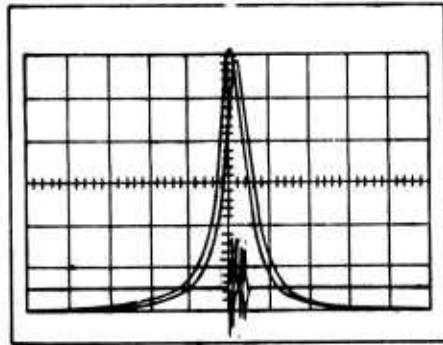
$\lambda_0$  = free-space wavelength

$\alpha = \chi/2$ .

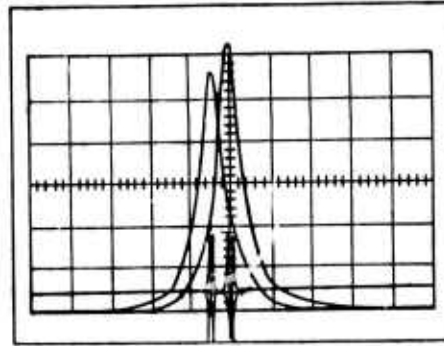
This expression can be simplified in this case, and to a high degree of accuracy is given by

$$\beta = n' \cdot \beta_0.$$

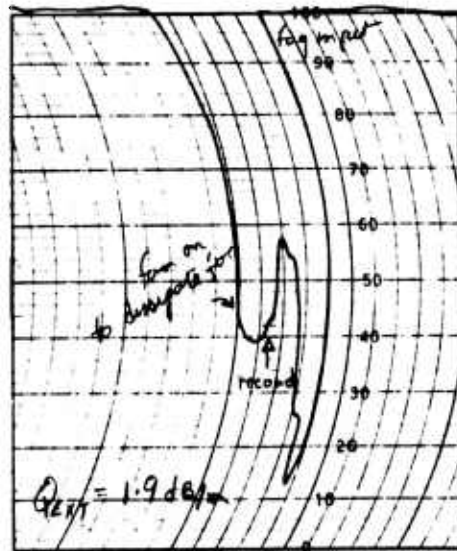
The loss tangent,  $\tan \delta = \epsilon''/\epsilon'$ , of this medium can be readily determined. Writing



$T = -35^{\circ}\text{C}$ ,  $\Delta f = 270.4 \text{ kHz}$ ,  $\alpha = 3.98 \times 10^{-6} \text{ cm}^{-1}$

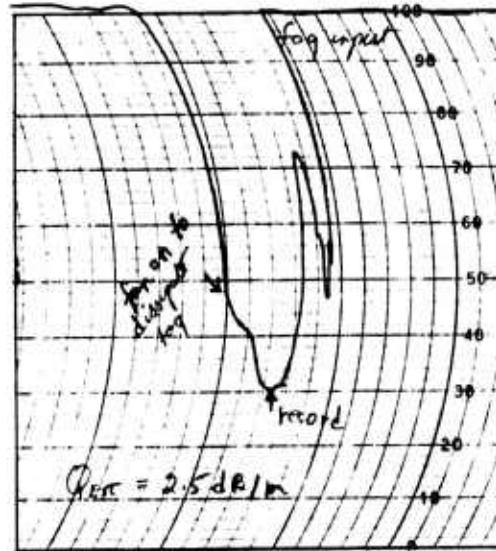


$T = -35^{\circ}\text{C}$ ,  $\Delta f = 637.3 \text{ kHz}$ ,  $\alpha = 7 \times 10^{-6} \text{ cm}^{-1}$



LASER EXTINCTION RECORD

Figure 49. Sample cavity response due to ice fog,  $T = -35^{\circ}\text{C}$ .



LASER EXTINCTION RECORD

Figure 50. Sample cavity response due to ice fog,  $T = -35^{\circ}\text{C}$ .

$$m_c = n' - jn'' = \sqrt{\epsilon_c}$$

and since

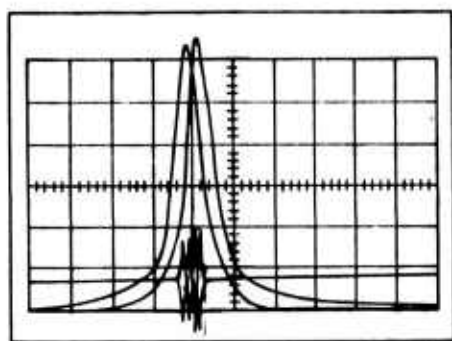
$$m_c = \frac{c}{\omega} (\beta - ja)$$

where

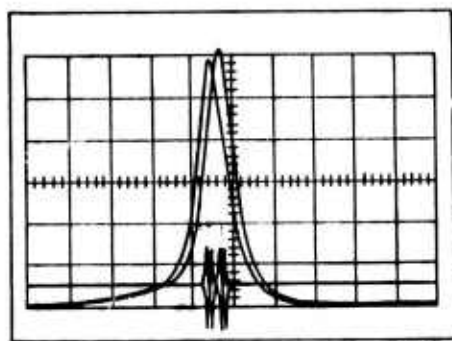
$$\frac{c}{\omega} = \frac{\lambda_0}{2\pi}$$

then

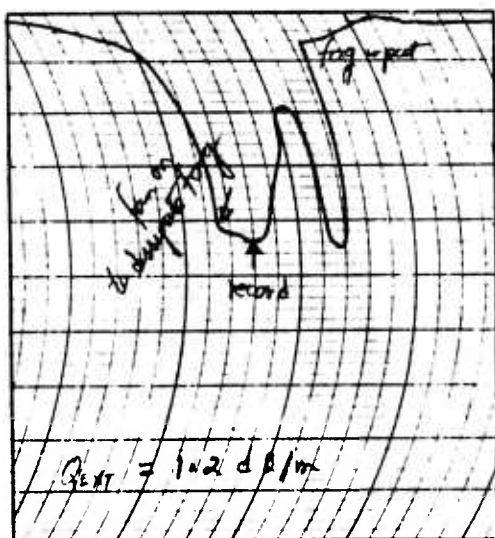
$$n'' = \alpha \frac{\lambda_0}{2\pi}$$



$T = -39^{\circ}\text{C}$ ,  $\Delta f = 241.9 \text{ kHz}$ ,  $\alpha = 1.81 \times 10^{-6} \text{ cm}^{-1}$

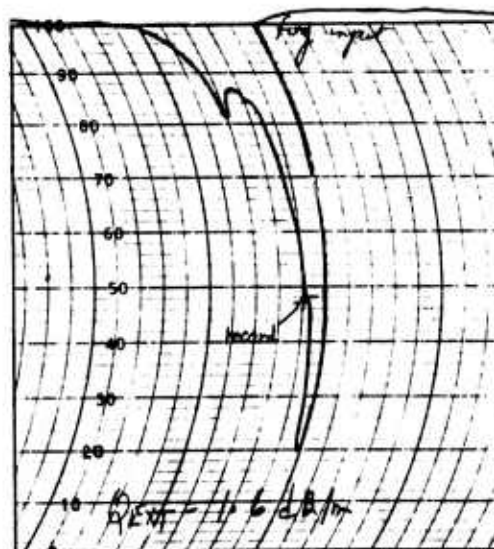


$T = -39^{\circ}\text{C}$ ,  $\Delta f = 333.2 \text{ kHz}$ ,  $\alpha = 2.68 \times 10^{-6} \text{ cm}^{-1}$



LASER EXTINCTION RECORD

Figure 51. Sample cavity response due to ice fog,  $T = -39^{\circ}\text{C}$ .



LASER EXTINCTION RECORD

Figure 52. Sample cavity response due to ice fog,  $T = -39^{\circ}\text{C}$ .

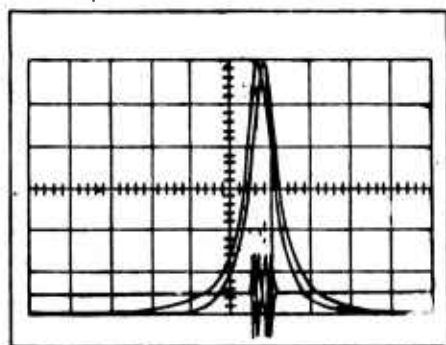
and thus

$$\tan \delta = \frac{2n'n''}{(n')^2 - (n'')^2} = 2n'' = \alpha \left( \frac{\lambda_0}{\pi} \right) = \chi \left( \frac{\lambda_0}{2\pi} \right)$$

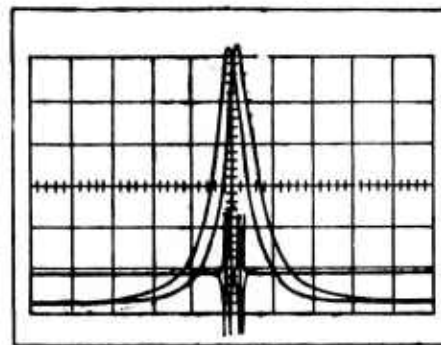
Table XI lists the appropriate propagation parameters which characterize the propagation of 97-GHz radio waves through ice fogs over the temperature interval  $-29^{\circ}$  to  $-46^{\circ}\text{C}$ .

At the conclusion of each data run, the fan was switched on to dissipate the fog. As the fog dissipated, the cavity response curve was observed to shift back to its original unperturbed state, which is a strong argument against drift and mirror accumulation effects.

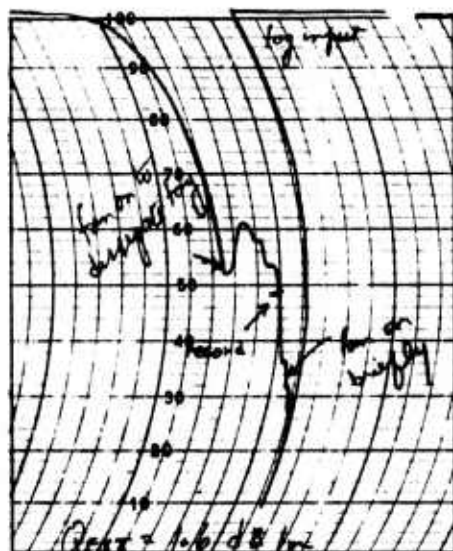
With these results, calculation of the effects of an ice fog on 97-GHz radio wave propagation can be made. In terms of signal propagation effects, it is more appropriate to refer to a 1-km path. The attenuation and phase shifts, appropriate for the temperature interval studied, for a 1-km path and an assumed 1-dB/m extinction of 6328 Å light, are presented in Table XII. As pointed out earlier, the electromagnetic measurements are well correlated with the reference helium-neon laser



$T = -43^{\circ}\text{C}$ ,  $\Delta f = 250.5 \text{ kHz}$ ,  $\alpha = 9.57 \times 10^{-7} \text{ cm}^{-1}$

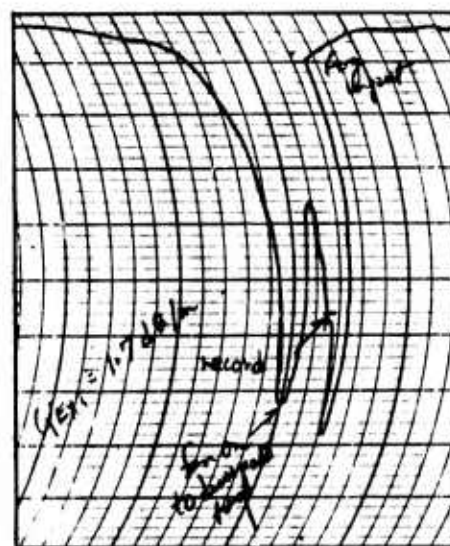


$T = -43^{\circ}\text{C}$ ,  $\Delta f = 261.8 \text{ kHz}$ ,  $\alpha = 8.0 \times 10^{-7} \text{ cm}^{-1}$



LASER EXTINCTION RECORD

Figure 53. Sample cavity response due to ice fog,  $T = -43^{\circ}\text{C}$ .



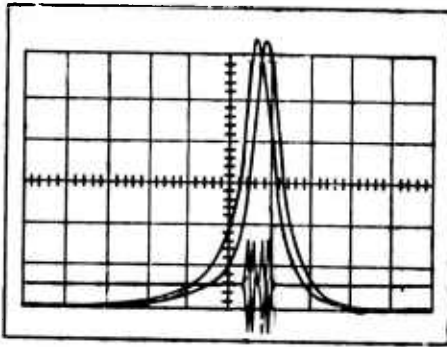
LASER EXTINCTION RECORD

Figure 54. Sample cavity response due to ice fog,  $T = -43^{\circ}\text{C}$ .

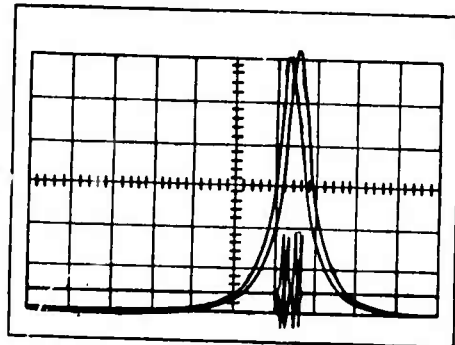
Table XI. Propagation constants of ice fogs at 97 GHz for 1 dB/m extinction of 6328 Å red light.

$T$ ( $^{\circ}\text{C}$ )	$N$ -units	Mean extinction coeff $\chi(\text{cm}^{-1})$	$(\beta - \beta_0) \times 10^3$ (rad/m)	$\tan \delta$
-29.3	$1.31 \pm 0.64$	$3.83 \pm 1.11 \times 10^{-6}$	2.666	$1.38 \times 10^{-7}$
-34.4	$1.96 \pm 0.46$	$2.21 \pm 0.7 \times 10^{-6}$	3.989	$1.09 \times 10^{-7}$
-38.3	$2.36 \pm 0.36$	$8.08 \pm 4.68 \times 10^{-7}$	4.803	$3.98 \times 10^{-8}$
-42.8	$2.04 \pm 0.28$	$6.12 \pm 1.79 \times 10^{-7}$	4.151	$3.01 \times 10^{-8}$
-46.2	$1.69 \pm 0.18$	$5.0 \pm 1.71 \times 10^{-7}$	3.439	$2.46 \times 10^{-8}$

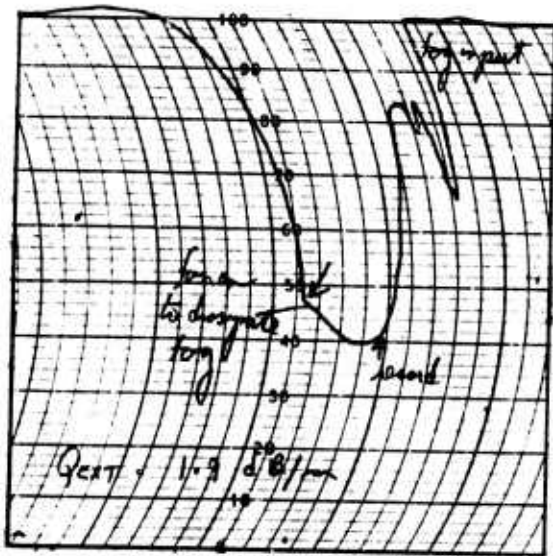
70 COMPLEX REFRACTIVE INDEX OF ICE FOG AT A RADIO WAVELENGTH OF 3 MM



$T = -46.5^{\circ}\text{C}$ ,  $\Delta f = 262.1 \text{ kHz}$ ,  $\alpha = 4.8 \times 10^{-7} \text{ cm}^{-1}$

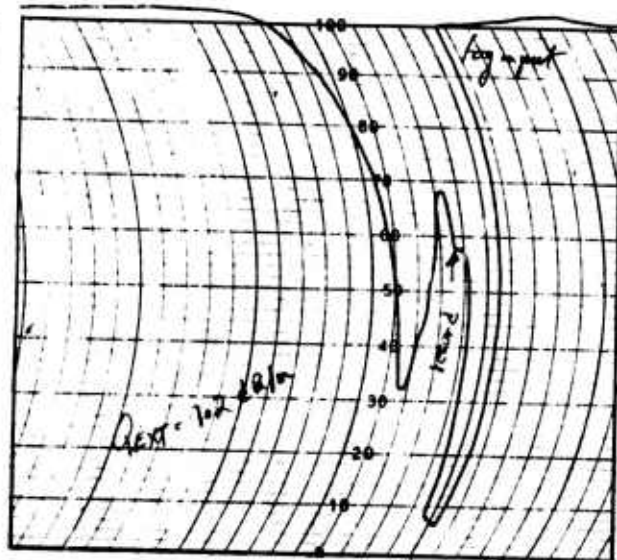


$T = -46.5^{\circ}\text{C}$ ,  $\Delta f = 224.5 \text{ kHz}$ ,  $\alpha = 7.25 \times 10^{-8} \text{ cm}^{-1}$



LASER EXTINCTION RECORD

Figure 55. Sample cavity response due to ice fog,  $T = -46.5^{\circ}\text{C}$ .



LASER EXTINCTION RECORD

Figure 56. Sample cavity response due to ice fog,  $T = -46.5^{\circ}\text{C}$ .

Table XII. One-way radio wave propagation effects (for 1 dB/m extinction of 6328 Å red light).

$T$ ( $^{\circ}\text{C}$ )	Attenuation (dB/km)	Differential phase shift $(\beta - \beta_0) \cdot z$ (rad/km)
-29.3	$1.66 \pm .48$	2.666
-34.4	$0.96 \pm .31$	3.989
-38.3	$0.35 \pm 0.2$	4.803
-42.8	$0.27 \pm .08$	4.151
-46.2	$0.22 \pm .08$	3.439

level for extinction of 2 dB/m or less. Therefore, it is appropriate to scale to propagation parameters from this table according to the measured laser level so long as this limitation is observed.

**Comparison of computed and measured values**

*Change of index of refraction due to the ice fog.* The general results obtained in the previous section may be compared with the theoretical prediction of the Van de Hulst expression

$$n' = 1 + \frac{2\pi N}{k^3} \text{Im} \{S(0)\}.$$

The ice fog impactor measurements of Chapter VII emphasized that the number-densities reported were a lower limit to the true number-density since the collection efficiency of the impactor was unknown and the smaller particles were poorly sampled. As indicated in Chapter VII, the craters measured under the microscope were taken to be indicative of the particle size making them, but this may not be accurate. For example, a solid spherical particle colliding with a thin magnesium-oxide coated glass surface would not necessarily make a crater the size of its own diameter, but could in fact make a much smaller area proportional to the amount of magnesium oxide crushed down to the point of contact of the spherical particle surface with the glass.

Both the literature and private communication with some authorities in this area have indicated that no method or technique exists for making accurate, reliable ice fog number-density measurements. The measurements made on these ice fogs indicated the existence of number-densities of from 100 to about 300 particles/cm<sup>3</sup>, with the apparent diameter of most particles less than about 15 μ.

In any case, it is reasonable to take 200 particles/cm<sup>3</sup> of 20 μ diameter, which gives an N-unit refractive index change of

$$(n - 1) \times 10^6 = \frac{(2\pi)(200)(10^6)}{8.43 \times 10^9} \cdot \frac{3}{2} \cdot 2.30 \times 10^{-6} \times 10^6$$

$$\cong 0.52 \text{ N-units.}$$

The expected change in the index of refraction is quite sensitive to the ice particle size, as previously stated. This can best be emphasized by making one more brief calculation for 30-μ-diam particles with the same density. Here,

$$(n - 1) \times 10^6 = \frac{2\pi(200)(10^6)}{8.43 \times 10^9} \cdot \frac{3}{2} \cdot 7.75 \times 10^{-6} \times 10^6$$

$$\cong 1.73 \text{ N-units.}$$

These calculations assumed small (with respect to a wavelength) spherical particles of complex dielectric constant  $\epsilon_c = 3.08 - j .004$ . The value of  $S(0)$ , appropriate to these particle diameters, is 3/2 times the value of  $b_1^{im}$  listed in Table V.

This is not meant to minimize the effective contribution of the smaller particles. Large numbers of the smaller particles are undoubtedly present, and their effective contribution, which varies directly with their number density, is likely some significant fraction of the overall N-unit measurement.

72 COMPLEX REFRACTIVE INDEX OF ICE FOG AT A RADIO WAVELENGTH OF 3 MM

For example, 10,000 particles of 6  $\mu$  diameter per cubic centimeter would give a change in the index of refraction of

$$(n - 1) \cdot 10^6 = \frac{(2\pi) \times 1 \times 10^4 \times 10^6}{8.43 \times 10^9} \times \frac{3}{2} \times 6.2 \times 10^{-8} \times 10^6$$

$$\approx 0.7 \text{ N-unit}$$

and several tenths more N-unit could easily come from the more easily detected larger particles in the size range 15-25  $\mu$ .

*Radio wave loss due to the fog.* The expression for energy loss due to an assemblage of small scatterers, as given, is

$$\chi = 2kn''$$

where  $k = \frac{2\pi}{\lambda}$

and  $n'' = \frac{2\pi N}{k^3} \text{Re}\{S(0)\}$ .

This, too, is very sensitive to the number and sizes of the particles involved. To consider a case similar to the last case in the section above, 10,000 particles 6  $\mu$  in diameter would give a theoretical loss of

$$\chi = \frac{4\pi \times 10^4 \cdot 10^6}{4.5 \times 10^6} \times \frac{3}{2} \cdot 7.04 \times 10^{-11} \cdot 10^{-2} \text{ cm}^{-1}$$

$$= 2.95 \times 10^{-8} \text{ cm}^{-1}$$

and, for 200 particles 30  $\mu$  in diameter, the loss would be

$$\chi = \frac{(4\pi)(2) \times 10^2 \cdot 10^6}{4.5 \times 10^6} \times \frac{3}{2} \cdot 8.9 \times 10^{-9} \times 10^{-2}$$

$$= 7.5 \times 10^{-8} \text{ cm}^{-1}$$

The cavity measurements, for the colder and more stable fogs, indicate a loss of about  $5 \times 10^{-7} \text{ cm}^{-1}$ . This is about a factor of 7 greater than the last theoretical calculation would indicate. These calculations were again made for a dielectric constant of  $\epsilon_c = 3.08 - j .004$ .

These calculations can be compared with the predicted loss for a water fog. In this case,  $\epsilon_c = 12 - j 15$ , and for 6- $\mu$ -diam water spheres

$$b_1^{\text{re}} = 1.7 \times 10^{-8}$$

Therefore the ratio

$$\frac{(b_1^{re})_{\text{water}}}{(b_1^{re})_{\text{ice}}} = \frac{1.7 \times 10^{-8}}{7 \times 10^{-11}} = 250$$

and thus the expected loss for a water fog would be on the order of 250 times that for an ice fog of the same number-density. The theoretical and experimental measurements are in far closer agreement than this (less than a factor of 10) for the ice fog, and, as mentioned in the preceding section, this discrepancy certainly reflects in part the uncertainty in the particle size/number-density distribution. Of course, some small fractional part of the fog particles could still be liquid at these temperatures, which could account for this discrepancy.

*Experimental and theoretical relationship of  $n'$  with  $n''$ .* One further bit of information can be extracted from these data. From the Van de Hulst expressions for the complex refractive index of the medium,

$$n' = 1 + \frac{2\pi N}{k^3} \text{Im} \{S(0)\}$$

$$n'' = \frac{2\pi N}{k^3} \text{Re} \{S(0)\}$$

$$S(0) = \frac{1}{2} \sum_{n=1}^{\infty} (2n+1)(a_n^s + b_n^s)$$

where all factors are the same as previously described in Chapter IV. Then the ratio

$$n''/(n' - 1) 10^{-6}$$

is independent of the actual fog particle number and distribution, and only dependent upon the complex dielectric constant of the individual particles. This can be readily seen for this case where the wavelength is much larger than the particle diameter (Rayleigh approximation), where

$$\frac{1}{2} \sum_{n=1}^{\infty} (2n+1)(a_n^s + b_n^s) \cong \frac{3}{2} (a_1^s + b_1^s)$$

and where

$$a_1 = \frac{j(m^2 - 1)}{45} \rho^5$$

= first magnetic mode in the sphere

$$b_1 = -j \frac{2}{3} \left( \frac{m^2 - 1}{m^2 + 2} \right) \rho^3$$

= first electric mode in the sphere

74 COMPLEX REFRACTIVE INDEX OF ICE FOG AT A RADIO WAVELENGTH OF 3 MM

where  $\rho = k_0 a$

$a$  = radius of dielectric sphere

$$k_0 = 2\pi/\lambda_0$$

$m$  = complex refractive index of the small spheres.

$b_1$  dominates  $a_1$ , hence the ratio  $\text{Re}\{S(0)\}/\text{Im}\{S(0)\}$  is the ratio of the real to the imaginary part of  $b_1$ , and hence the sphere size dependence drops out.

The Fabry-Perot cavity measures the extinction coefficient associated with the fog losses. Since for this wavelength and this size particle absorption dominates scattering effects, then for all practical purposes extinction = absorption, and

$$\chi = 2\alpha$$

where  $\alpha$  is a field quantity and  $\chi$  is the extinction measured for the power loss due to the ice fog. Another form, as given earlier, for the complex index of refraction is

$$m = n' - jn'' = \frac{c}{\omega} (\beta - ja).$$

Therefore,

$$n'' = \frac{c\alpha}{\omega} = \frac{c\chi}{2\omega} = \frac{\chi}{4070} \times 10^2 \text{ for } \chi \text{ in cm}^{-1}.$$

Writing

$$\frac{n''}{(n' - 1) \times 10^{-6}} = \frac{\chi}{N} \frac{10^2}{4070 \times 10^{-6}} = \frac{\chi}{N} 2.46 \times 10^4.$$

From these ice fog measurements, appropriate values to take for the 97-GHz extinction due to the ice fog and the N-unit change in the medium refractive index would be

$$\chi = 5 \times 10^{-7}$$

and

$$N = 2,$$

to get

$$\frac{n''}{(n' - 1) \times 10^{-6}} = \frac{5 \times 10^{-7} \times 2.46 \times 10^4}{2} = 6.15 \times 10^{-3},$$

and for a measured solid ice complex dielectric constant of  $\epsilon_c = 3.1 - j .004$ ,

$$S(0) = j \left( \frac{m^2 - 1}{m^2 + 2} \right) \rho^3 \\ = + 0.462 \times 10^{-3} + j 0.411$$

then

$$\frac{\text{Re } \{S(0)\}}{\text{Im } \{S(0)\}} = 1.13 \times 10^{-3}.$$

The ratio  $n''/(n' - 1) 10^{-6}$  was based upon data taken from the low temperature ice fogs;  $5 \times 10^{-7} \text{ cm}^{-1}$  is well within the possible error for the three lower temperature fogs. A  $\chi$  of  $5 \times 10^{-7} \text{ cm}^{-1}$  was used since these lower temperature fogs are stable in that they are considered below the transition temperature for spontaneous droplet freezing. In computing the ratio of

$$\frac{\text{Re } \{S(0)\}}{\text{Im } \{S(0)\}}$$

the mean dielectric constant found earlier for slab ice was used. The match between the measured value of

$$n''/(n' - 1) 10^{-6}$$

and the computed quantity

$$\frac{\text{Re } \{S(0)\}}{\text{Im } \{S(0)\}}$$

is fairly good, and these results are not unexpected in light of the results of the preceding section. With the error bars involved on the measured quantities, going into the above ratios, it is possible to obtain a near-perfect agreement, although this is not the important point here. The point is that the Fabry-Perot cavity measurements which can be related to the complex dielectric constant of the ice fog particles are in substantial agreement with previously made slab ice complex dielectric constant measurements.

### VIII. SUMMARY AND CONCLUSIONS

The main thrust of this work was to make measurements of the index of refraction and signal loss associated with propagation of 3-mm radio waves through an arctic ice fog. This work was originally motivated by the planned operation of 3-mm pulse radars on surface effects vehicles to be operated over arctic terrain. These radars scan horizontally at near grazing angles of incidence and must be capable of seeing objects through low temperature fogs soon enough for evasive action to be taken. The low temperature ice fog is a relatively common meteorological occurrence in the Arctic and Antarctic, and almost nothing was known of its effect on 3-mm radio waves. These measurements are thus a "first ever" attempt to characterize the 3-mm radio wave propagation effects of an ice fog.

It was also of specific interest to make measurements of the complex dielectric constant of slab ice at 97 GHz to compare these measurements with the high frequency limiting values of  $\epsilon_{\infty}$  typically used in the Debye equations and found in the literature for frequencies up to about 25 GHz. The complex dielectric constant of pure ice was found to be  $\epsilon_c = (3.08 \pm 0.2) - j(3.99 \pm 1.50) \times 10^{-3}$ . The real part, 3.08, is in excellent agreement with the limiting values reported in the literature for frequencies up to 24 GHz, but the imaginary part is slightly higher at 97 GHz than the reported values for lower frequencies. Measurements of samples of the ice prepared from water samples taken from a local lake gave slightly higher values for the complex dielectric constant, but the error bars associated with these measurements are all overlapping.

The technique used to make these measurements involved a quasi-optical free-space approach commonly described in the literature and successfully used at lower frequencies. Prior to using this technique directly on making the ice measurements an extensive sequence of measurements was made on materials of known permittivity. One such material with a well behaved and known permittivity is polystyrene. This calibration sequence was done primarily to establish the necessary care and skill prior to making the ice measurements.

The ice fog measurements were made with a Fabry-Perot cavity, a device commonly used in optical interferometry. The Fabry-Perot resonator has been adapted to millimeter wave usage, and ample precedent for its use exists in the literature. The Fabry-Perot resonator built for this experiment is an open-sided semi-confocal resonator (the fields are established between one spherical and one flat mirror) with a measured, loaded  $Q$  of 140,000 at an operating wavelength of 3.09 mm. The semi-confocal cavity was selected for use primarily for the convenience of its physical size and its ease of mechanical construction. It can be demonstrated that the change in the index of refraction of a medium is measured by the change in the cavity resonant frequency, and the change in the amplitude of the cavity response is related to the losses of the medium.

A method employing a phase-locking technique was used to lock the klystron to a high multiple of a stabilized reference 1.7-GHz oscillator. The difference between this reference frequency and the klystron frequency, the IF, was compared with the output of a sweep generator in a phase locking system, and the dc error output was used to steer the klystron in such a manner that its frequency deviation at 97 GHz followed the frequency deviation of the sweep generator. Thus the klystron frequency was locked and swept  $\pm \Delta f$  over the Fabry-Perot cavity frequency. The output of the cavity was sampled through a square-law detector loosely coupled to the cavity and displayed as the ordinate on an oscilloscope. Marker beats, whose frequencies could be measured with high precision, were also displayed superimposed on the horizontal oscilloscope sweep, and these were used to measure the cavity frequency shift between conditions of ice fog and no fog in the cavity. This technique of sweeping the cavity and photographing the response proved especially convenient for information readout and storage.

Ice accumulation on the mirror surfaces was investigated by grazing a laser beam across the metal surface and photographing the light scattering from the adhering ice particles. Time lapse photography showed that this accumulation occurred only during the first few seconds after entry of the warm steam fog, and that the total accumulation was small when compared with the light scattered by a thin  $3\text{-}\mu$  polystyrene dust coat. Furthermore, it was seen that if a thin, low loss dielectric material covered the mirrors, there was no measurable change in cavity response. When the environmental chamber was shut down and quickly opened, a heavy white frost coating was quickly formed on all interior metal parts from the intruding warm, moist air. This had no effect on the cavity response, but just as soon as this frost coat started to liquefy the response changed radically. Additional confirmation of mirror accumulation effects came when the interior fan was restarted after fog electromagnetic measurements had been made. As the fog was dissipated, the cavity response curve could be observed to shift back to its original no-fog response. This is also indicative of a minimum amount of mechanical and electrical drift effects.

An environmental chamber of about  $70\text{ ft}^3$  volume was constructed of Styrofoam to house the refrigeration evaporators and the Fabry-Perot cavity. Waveguide was run through the chamber walls to connect with the electronics. Mirror movement was accomplished through remote drive motors suitably geared down so as to move drive screws in three mutually orthogonal directions to control the spherical mirror. The refrigeration compressor, a 3-hp, 3-phase unit, was resurrected from an old piece of surplus equipment. To get to the low temperatures necessary for this work it was necessary to use a lower boiling point refrigerant, R-502. Chamber temperatures as low as  $-50^\circ\text{C}$

could be achieved and maintained. To minimize vibration effects during the electromagnetic measurements it was necessary to stop both the fan and the compressor. Temperature changes in the chamber during this time were rarely observed to exceed two degrees.

Initially it was planned to correlate fog number-density measurements with the electromagnetic measurements. This plan hinged upon having a reliable method for obtaining these measurements, or at least having experienced help in obtaining these data. As it turned out, the help never materialized, and a borrowed cascade impactor was all the instrumentation available. This impactor used magnesium oxide coated slides upon which the ice fog particles would "crater," leaving pits the size of the fog particles to be counted. Slides made of the colder fogs were generally fairly consistent; much more difficulty was encountered in trying to obtain any degree of repeatability with the warmer fogs. On many of the slides taken with this impactor there were very faint traces of particles less than about  $4 \mu$ . These were too faint to satisfactorily count, and thus these measured number densities represent only some kind of lower limit to the true fog number densities. During the later stage of this experiment a single-stage silicone oil impactor was used to make fog density measurements. This device, too, proved to be unsatisfactory and inconclusive. This type of impactor should only be used in an environment at or below the freezing temperature. As it turned out, the collected particles started to disappear from the oil base collecting medium as soon as the impactor was withdrawn from the environmental chamber. By the time these collections were photographed, an average of 20 seconds had elapsed, far too long a time for any accurate analysis. However, these oil base impactor measurements did show a very substantial number of small particles, and surprisingly there appeared to be a small number (30 or so on one particular photograph) of very large ( $> 25 \mu$  diameter) particles per cubic centimeter present.

There is also some question about the accurate particle size replication of the magnesium-oxide craters formed by the impacting ice fog particles. The "craters" measured and studied under the microscope may not have had diameters equivalent to the ice particle diameters, but in fact the crater size could have been smaller than the actual particle sizes. A solid spherical particle, for example, would crush the magnesium-oxide coating down only to the point of contact with the underlying glass, which would make a "crater" much smaller than the impacting particle. This is undoubtedly responsible for some of the discrepancy between the theoretical and experimental results (as noted in Chapter VII), as the magnesium-oxide films deposited on these slides tended to be quite thin which enhances this effect.

In order to achieve some degree of uniformity from fog to fog, a helium-neon laser beam was shot through a 2-m path in the fog, and all electromagnetic and impactor measurements were made at or near a laser extinction level of 1.5 dB/m. The required fog density was achieved simply by inputting and mixing the fog with the fan until the required extinction level was reached. While somewhat arbitrary, this amount of laser extinction was chosen since it was well within the dynamic range of the optical detector, and was, for the total path, a total extinction level checked and calibrated by an optical filter of known transmission properties. In addition, this fog density provided for a reasonable amount of cavity response (frequency and amplitude change). Visually, this fog level appeared to be at least as dense as any warm fog ever encountered in a southern swamp on a cool, calm evening.

Calculations of the total extinction of the  $6328 \text{ \AA}$  laser red light were made and compared with the measured extinction. These calculations used as input data the measured number-density and particle sizes of these ice fogs. However, the calculated extinction was between  $\frac{1}{4}$  and  $\frac{1}{2}$  (depending upon the particular number density distribution used) of the actual measured extinction. This says that either the number distribution used in the calculations is somewhat wrong, or Mie's theory has been incorrectly applied to the ice fog particles (that is, the particles may be tiny prisms, or geometrical columns with flat faces). This information was communicated to interested

groups at Johns Hopkins Applied Physics Laboratory and to the Cold Regions Research and Engineering Laboratory. This finding is in substantial agreement with their results for ice fogs, and has not yet been resolved.

One of the major problems yet to be solved is how to accurately measure ice fog particle number densities. One group at White Sands made a study of impactor types and various replicating media, and concluded that fog drop size distributions were method-dependent. They also concluded that no method was satisfactory for detecting or capturing small droplets less than  $4 \mu$  in diameter, and that "lack of correlation between number of captured droplets and visibility was present in even the most careful determinations employing impactor methods. It appears that either small droplets have not been captured and replicated or that factors other than scattering by water droplets contribute heavily to the deterioration of visibility in fog."

It was therefore concluded that the electromagnetic measurements could not be referenced to the fog impactor measurements. The most reasonable reference standard for these electromagnetic measurements was taken to be measured extinction of a 6328 Å helium-neon laser. The laser extinction, supplemented by the impactor measurements and recorded temperature, thus constitute the best meteorological description of fog which could be obtained.

By being as consistent as possible in generating these fogs over the temperature interval of interest, the measured changes in the index of refraction ran from about  $\frac{3}{4}$  to  $2\frac{1}{2}$  N-units for 1 dB/m of laser extinction. The extinction coefficient dropped from a high of  $3.8 \times 10^{-6} \text{ cm}^{-1}$  at  $29^\circ\text{C}$  to  $8 \times 10^{-7} \text{ cm}^{-1}$  at  $-38^\circ\text{C}$ , and then dropped very slowly to  $5 \times 10^{-7}$  at  $-46^\circ\text{C}$ . The temperature interval  $-30^\circ$  to  $-36^\circ\text{C}$  is somewhat critical to ice fog formation. A critical literature review indicated that natural ice fogs almost never occur at temperatures above  $-30^\circ\text{C}$ , and occur much more frequently and with increasing severity (greater reduction of visibility) with the onset of lower temperatures.

Theoretical calculations using the Van de Hulst expressions tend to confirm the experimental measurements. Both the refractive index calculations and the loss calculations tend to be low (but within a factor of 10) in comparison with the experimental measurements. The experimental measurements indicate that a higher volume of ice particles per unit volume exists in the cavity than is indicated by the impactor measurements, which, for reasons given earlier, are thought to be lower limits to the true number densities. If the fog were entirely liquid, the theoretical calculations indicate that the loss, for example, would be more than 200 times what it is for an ice fog. It is also possible that some small fraction of the fog particles are liquid or have a liquid coat. This, together with low particle samples, could account for the discrepancy between the measured and calculated values indicated in Chapter VII.

The ratio of the experimentally measured quantity

$$\frac{n''}{(n' - 1) 10^{-6}}$$

can be compared with the theoretical ratio obtained for a very dilute scattering medium

$$\frac{\text{Re } \{S(0)\}}{\text{Im } \{S(0)\}}$$

where  $S(0)$  is formed from the series of the complex amplitude coefficients associated with the electric and magnetic modes present in the dielectric spheres. For the Rayleigh limit it can be shown that there is no particle volume dependency in the above ratio. Therefore the ratio  $\text{Re } \{S(0)\} / \text{Im } \{S(0)\}$  depends upon the complex dielectric constant of ice used in the computation of  $S(0)$ . When

each of these ratios is computed, in one case from a knowledge of the complex dielectric constant of ice, and in the other case using the measured cavity extinction and index of refraction, they are less than a factor of six from each other.

Therefore the larger extinction coefficients and their rapid drop-off above about  $-36^{\circ}\text{C}$  are not surprising, since some small fraction of the ice fog may still be liquid, either existing as isolated liquid drops or as a liquid coating on some ice crystals.

Both the refractive index measurements and the extinction coefficients correlated very well with the measured laser extinction. While it is true that the laser is sensitive to small particle concentrations, and the cavity is sensitive to larger particles (since its response depends upon net volume of ice in its fields), the particle distribution is apparently not changing radically over the temperature range  $-29^{\circ}$  to  $-46^{\circ}\text{C}$  since there is both a uniform warm fog input at all temperatures and good correlation with the measured electromagnetic parameters.

Since the impactor measurements of these fogs are quite similar to the measurements of established experts in the field, there is no reason to suspect that these ice fogs are atypical of naturally occurring fogs, except in density. But because of the good correlation with the measured helium-neon laser extinction, it is appropriate to scale these measured values of  $\chi$  and  $N$  down to arrive at an expected value for 97 GHz radio wave extinction and phase shift in an ice fog of lesser density.

#### LITERATURE CITED

- Aden, A.L. (1950) Electromagnetic scattering from metal and water spheres. Office of Naval Research Report No. 106.
- Auty, R.P. and R.H. Cole (1952) Dielectric properties of ice and solid  $\text{D}_2\text{O}$ . *Journal of Chemical Physics*, vol. 20, no. 8, p. 1309.
- Ball, F.K. (1959) Winds on the ice slopes of Antarctica. *Antarctic Meteorology, Proceedings of Symposium held in Melbourne*, p. 9.
- Benson, C. (1965) Ice fog: low temperature air pollution - defined with Fairbanks, Alaska as type locality. University Geophysical Institute Report, UAG-R-173. Also USA CRREL Research Report 121, 1970.
- Bertie, J.G. and E. Whalley (1964) Infrared spectra of ices  $I_H$  and  $I_C$  in the range 4000 to  $350\text{ cm}^{-1}$ . *Journal of Chemical Physics*, vol. 40, p. 1637-1659.
- Boyd, G.D. and J.P. Gordon (1961) Confocal multimode resonator for millimeter through optical wavelength masers. *Bell System Tech. Journal*, vol. 40, p. 489-508.
- Boyd, G.D. and H. Kogelnik (1962) Generalized confocal resonator theory. *Bell System Tech. Journal*, vol. 41, p. 1347-1369.
- Chamberlain, J.E., G.W. Chantry, H.A. Geffie, N.W.B. Stone, T.B. Taylor and G. Wyllie (1966) Submillimeter absorption and dispersion of liquid water. *Nature*, vol. 210, no. 5038, p. 790.
- Civilong, B.M. (1945) Sublimation in a Wilson Chamber. *Nature*, vol. 155, p. 361.
- Civilong, B.M. (1947) Observations on the incidence of supercooled water in expansion chambers and on cooled solid surfaces. *Journal of Glaciology*, vol. 1, no. 2, p. 53.
- Civilong, B.M. (1947) Sublimation in outdoor air. *Nature*, vol. 160, p. 198.
- Culie, C.H., J.B. Hasted and D.M. Retson (1948) The dielectric properties of water and heavy water. *Proceedings of the Physical Society*, vol. 60, p. 145.
- Culshaw, W. (1959) Reflectors for a microwave Fabry-Perot interferometer. *IRE Transactions on Microwave Theory and Techniques*, MTT-7, p. 221-228.

- Culshaw, W. (1960) High resolution millimeter wave Fabry-Perot interferometer. *IRE Transactions on Microwave Theory and Techniques*, MTT-8, p. 182-189.
- Culshaw, W. (1961) Resonators for millimeter and submillimeter wavelengths. *IRE Transactions on Microwave Theory and Techniques*, MTT-9, p. 135-144.
- Culshaw, W. (1962) Further considerations on Fabry-Perot type resonators. *IRE Transactions on Microwave Theory and Techniques*, MTT-10, p. 331-339.
- Culshaw, W. and M.V. Anderson (1962) Measurement of permittivity and dielectric loss with a millimeter-wave Fabry-Perot interferometer. *Proc. IEE, London, Part B, Supp.*, vol. 109, no. 23, p. 820-826.
- Cumming, W.A. (1952) The dielectric properties of ice and snow at 3.2 cm. *Journal of Applied Physics*, vol. 23, p. 768.
- D'Albe, F. (1918) Condensation of water vapor below  $1^{\circ}\text{C}$ . *Nature*, vol. 162, p. 921.
- Debye, P. (1929) *Polar molecules*. New York: The Chemical Catalogue Co., Inc.
- Dees, J.W. and A.P. Sheppard (1965) Fabry-Perot interferometer at 168 Gc/s. *IEEE Transactions on Instrumentation and Measurement*, p. 52-58.
- Degenford, J.E. and P.D. Coleman (1966) A quasi-optics perturbation technique for measuring dielectric constants. *Proc. IEEE*, vol. 54, no. 4, p. 520-522.
- Dunsmuir, R. and J. Lamb (1945) The dielectric properties of ice at wavelengths of 3 and 9 cm. Manchester University Report No. 61.
- Eisenberg, D. and W. Kouzmann (1969) *Structure and properties of water*. New York: Oxford University Press.
- Fox, A.G. and T. Li (1961) Resonant modes in a maser interferometer. *Bell System Tech. Journal*, vol. 40, p. 453-488.
- French, I.P. and T.E. Arnold (1967) High-Q Fabry-Perot resonator for nitric oxide absorption measurements at 150 GHz. *Review of Scientific Instruments*, vol. 28, no. 11, p. 1604-1607.
- Frenkel, L. and D. Woods (1966) The microwave absorption by  $\text{H}_2\text{O}$  vapor and its mixtures with other gases between 100 and 300 Gc<sup>2</sup>/s. *Proc. IEEE*, vol. 54, no. 4, p. 498-505.
- Gotaas, Y. and C.S. Benson (1965) The effect of suspended ice crystals on radiative cooling. *Journal of Applied Meteorology*, vol. 4, p. 146-153.
- Gunn, K.L.S. and T.W.R. East (1954) The microwave properties of precipitation particles. *Quarterly Journal of the Royal Meteorological Society*, vol. 80, p. 522.
- Hertel, P., A.W. Straiton and C.W. Tolbert (1953) Dielectric constant measurements at 8.6 millimeter-wavelength. Electrical Engineering Research Laboratory, University of Texas, Report No. 65.
- Ingalls, A.G. (Ed.) (1970) *Amateur telescope making*, Book 1, *Scientific American, Inc.*, p. 264.
- Irvine, W.M. and J.B. Pollack (1968) Infrared optical properties of water and ice spheres. *Icarus*, vol. 8, p. 324-360.
- Jackson, J.D. (1963) *Classical electrodynamics*. New York: John Wiley & Sons, Ch. 4.
- Kerr, D.E. (1951) *Propagation of short radio waves*. New York: McGraw-Hill.
- Kogelnik, H. and T. Li (1966) Laser beams and resonators. *Proc. IEEE*, vol. 54, no. 10, p. 1312-1329.
- Kumai, M. (1951) Electron-microscope study of snow crystal nuclei. *Journal of Meteorology*, vol. 8, p. 151.
- Kumai, M. (1964) A study of ice fog and ice-fog nuclei at Fairbanks, Alaska, Part I. U.S. Army Cold Regions Research and Engineering Laboratory (USA CRREL) Research Report 150.

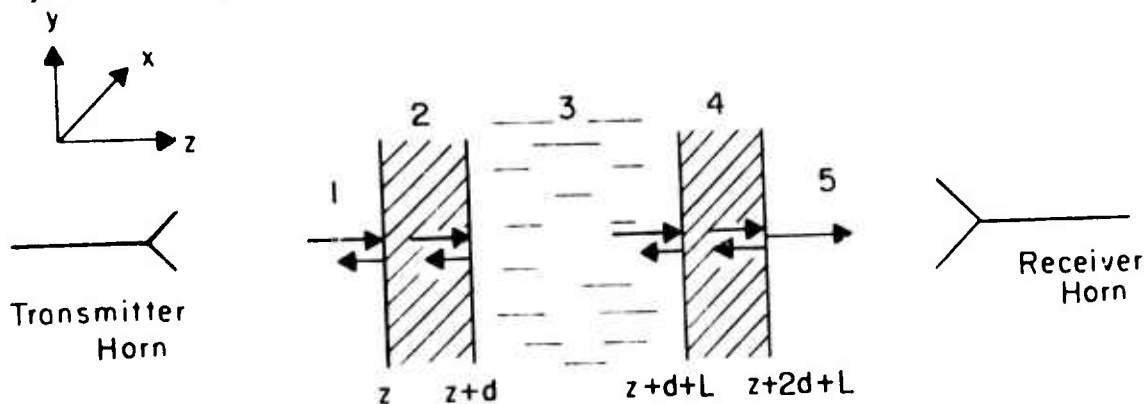
- Kumai, M. and H.W. O'Brien (1965) A study of ice fog and ice-fog nuclei at Fairbanks, Alaska, Part II. USA CRREL Research Report 150.
- Kumai, M. and J.D. Russell (1969) The attenuation and backscattering of infrared radiation by ice fog and water fog. USA CRREL Research Report 264.
- Kuriowa, D. (1957) Electron-microscope study of fog nuclei. *Journal of Meteorology*, vol. 8, p. 157.
- Lamb, J. (1916) Measurements of the dielectric properties of ice. *Transactions of the Faraday Society*, vol. 42A, p. 233.
- Lamb, J. and A. Turney (1949) The dielectric properties of ice at 1.25 cm wavelength. *Proc. Physical Society, London*, vol. B62, Pt. 4, p. 272.
- Lane, J.A. and J.A. Saxton (1952) Dielectric dispersion in pure polar liquids at very high radio-frequencies. 1. Measurements on water, methyl and ethyl alcohols. *Proceedings of the Royal Society*, vol. 213, p. 400.
- Lonsdale, K. (1958) The structure of ice. *Proceedings of the Royal Society, London*, vol. A247, p. 429.
- Mason, B.J. (1950) The formation of ice crystals and snowflakes. *Cent. Proceedings of the Royal Meteorological Society*, p. 51.
- Mason, B.J. (1950) The nature of ice-forming nuclei in the atmosphere. *Quarterly Journal of the Royal Meteorological Society*, vol. 76, no. 327, p. 59.
- Mie, G. (1908) *Ann. Physik*, vol. 25, p. 377.
- Minnaert, M. (1954) *The nature of light and colour in the open air*. Dover Publications, p. 190-208.
- Montgomery, C.G. (Ed.) (1947) *Techniques of microwave measurements*. (MIT Radiation Laboratory Series) MIT Press, Cambridge, Mass., p. 591-606.
- Munis, R. and A. Delaney (1972) Measurements of laser extinction in ice fog for design of SEV pilotage system. USA CRREL Research Report 302.
- Ohtake, T. (1967) Alaskan ice fog, 1. Proceedings of the International Conference on Physics of Snow and Ice, Part 1, Hokkaido University, Sapporo, Japan, p. 105.
- Ohtake, T., Personal communication.
- Ohtake, T. (1970) Unusual crystal in ice fog. *Journal of the Atmospheric Sciences*, vol. 27, no. 3, p. 509-511.
- Ohtake, T. (1970) Studies on ice fog. University of Alaska Geophysical Institute Report, UAG R-211, EPA Publication APTD 0626.
- Ohtee, S. (1949) Investigations on condensation nuclei. *Bulletin of American Meteorological Society*, vol. 30, no. 8, p. 295.
- Oliver, V.J. and M.B. Oliver (1949) Ice fog in the interior of Alaska. *Bulletin of American Meteorological Society*, vol. 31, no. 1, p. 23-26.
- Orvig, S. (Ed.) (1970) *World survey of climatology*. Elsevier Publishing Co., vol. 14.
- Pate, D.N. (1967) (Master's Thesis) University of Texas, Austin, Dept. of Electrical Engineering.
- Perry, J.W. and A.W. Straiton (1972) Dielectric constant of ice at 35.3 and 94.5 GHz. *Journal of Applied Physics*, vol. 43, no. 2, p. 731.
- Ragle, R.H., R.G. Blair and L.E. Persson (1964) Ice core studies of Ward Hunt Ice Shelf, 1960. *Journal of Glaciology*, vol. 5, no. 37, p. 39.
- Ray, P. (1971) Broad-band complex refractive indices of ice and water. Research Report of Atmospheric Sciences, Florida State University, Tallahassee.
- Reference Data for Radio Engineers* (1970) New York. International Telephone and Telegraph Corp., 5th ed., p. 428-429.

- Rinehart, G.S. (1969) Fog drop size distributions — measurement methods and evaluation. Atmospheric Sciences Laboratory of the White Sands Missile Range, Report ECOM-5247.
- Robinson, E., G.B. Bell, W.C. Thuman, G.A. St. John and E.J. Wiggins (1955) An investigation of the ice fog phenomena in the Alaska area. Final Report, Contract No. AF 19(122)-634. Stanford Research Institute, Stanford, California.
- Robinson, E., W.C. Thuman and E.J. Wiggins (1957) Ice fog as a problem of air pollution in the Arctic. *Arctic*, vol. 10, p. 89-104.
- Rothman, T. and J.O. Ledbetter (1968) Droplet size of cooling tower fog. U.S. Public Health Service Technical Report EHE-11-6802.
- Saxton, J.A., R.A. Bond, G.T. Coats and R.M. Dickinson (1962) Dispersion at millimeter wavelengths in methyl and ethyl alcohols. University of Texas, Electrical Engineering Research Laboratory, Report No. 7-21.
- Saxton, J.A. (1952) Dielectric dispersion in pure polar liquids at very high radio-frequencies II. Relation of experimental results to theory. *Proceedings of the Royal Society*, vol. 13, p. 473.
- Schaefer, V.J. (1946) The production of ice crystals in a cloud of supercooled water droplets. *Science*, vol. 104, no. 2707, p. 457.
- Schaefer, V.J. (1948) The production of clouds containing supercooled water droplets or ice crystals under laboratory conditions. *Bulletin of the American Meteorological Society*, vol. 29, p. 145.
- Schawlow, A.L. and C.H. Townes (1958) Infrared and optical masers. *Physical Review*, vol. 29, p. 1940-1949.
- Smithsonian Meteorological Tables* (1966) Prepared by R.J. List, 6th ed., p. 382-384.
- Straiton, A.W. and C.W. Tolbert (1948) Measurement of the dielectric properties of soils and water at 3.2 cm wavelength. *Journal of the Franklin Institute*, vol. 246, p. 13.
- Stratton, J.A. (1941) *Electromagnetic theory*. New York: McGraw-Hill.
- Thuman, W.C. and E. Robinson (1954) Studies of Alaskan ice-fog particles. *Journal of Meteorology*, vol. 11, p. 151-156.
- Van de Hulst, H.C. (1957) *Light scattering by small particles*. New York: John Wiley & Sons.
- Valkenburg, E.P. and V.E. Derr (1966) A high-Q Fabry-Perot interferometer for water vapor absorption measurements in the 100 Gc/s to 300 Gc/s frequency range. *Proc. IEEE*, vol. 54, no. 4, p. 493-498.
- Von Hippel, A. (Ed.) (1954) *Dielectric materials and applications*. Cambridge, Mass.: MIT Press, p. 301.
- Vonnegut, B. (1947) The nucleation of ice formation by silver iodide. *Journal of Applied Physics*, vol. 18, no. 7, p. 593.
- Vonnegut, B. (1949) A note on nuclei for ice crystals formation. *Bulletin of American Meteorological Society*, vol. 30, no. 5, p. 194.
- Vonnegut, B. (1949) Nucleation of supercooled water clouds by silver iodide smokes. *Chemical Review*, vol. 44, p. 277.
- Weinreb, S. (1970) Millimeter-wave spectral line receiver-local oscillator and IF sections. National Radio Astronomy Observatory, Electronics Division Internal Report No. 97.
- Wiebe, M.L. (1971) Laboratory measurement of the complex dielectric constant of soils. Texas A&M University Remote Sensing Center Technical Report No. RSC-23.
- Worz, O. and R.H. Cole (1969) Dielectric properties of ice. *Journal of Chemical Physics*, vol. 51, p. 1546.
- Yoshino, T. (1961) Radio wave propagation on the ice cap. *Antarctic Record (Tokyo)*, no. 11, p. 228.

- Zimmerer, R.W. (1962) New wavemeter for millimeter wavelengths. *Review of Scientific Instruments*, vol. 33, no. 8, p. 858-859.
- Zimmerer, R.W., M.V. Anderson, G.L. Strine and Y. Beers (1963) Millimeter wavelength resonant studies. *IEEE Transactions on Microwave Theory and Techniques*, MTT-11, p. 142-149.
- Zimmerer, R.W. (1963) Spherical mirror Fabry-Perot resonators. *IEEE Transactions on Microwave Theory and Techniques*, MTT-11, p. 371-379.
- Zolotarev, V.M., B.A. Mikhailov, L.I. Alpervick and S.I. Popov (1969) Dispersion and absorption of liquid water in the infrared and radio regions of the spectrum. *Opt. Spektrosk*, vol. 27, p. 430.

APPENDIX

The derivation of the propagating E-field through a four-boundary three-layer medium is as follows:



Region 1:

$$E_x = A_1 e^{-j\beta_1 z} + B_1 e^{j\beta_1 z} \quad z < Z$$

$$H_y = \frac{1}{\eta_1} [A_1 e^{-j\beta_1 z} - B_1 e^{j\beta_1 z}]$$

Region 2:

$$E_x = A_2 e^{-\Gamma_2 z} + B_2 e^{\Gamma_2 z} \quad Z < z < Z + d$$

$$H_y = \frac{1}{\eta_2} [A_2 e^{-\Gamma_2 z} - B_2 e^{\Gamma_2 z}]$$

Region 3:

$$E_x = A_3 e^{-\Gamma_3 z} + B_3 e^{\Gamma_3 z} \quad Z + d < z < Z + d + L$$

$$H_y = \frac{1}{\eta_3} [A_3 e^{-\Gamma_3 z} - B_3 e^{\Gamma_3 z}]$$

Region 4:

$$E_x = A_4 e^{-\Gamma_4 z} + B_4 e^{\Gamma_4 z}$$

$$Z + d + L < z < Z + 2d + L$$

$$H_y = \frac{1}{\eta_4} \left[ A_4 e^{-\Gamma_4 z} - B_4 e^{\Gamma_4 z} \right]$$

Region 5:

$$E_x = A_5 e^{-j\beta_5 z}$$

$$z > Z + 2d + L$$

$$H_y = \frac{1}{\eta_5} \left[ A_5 e^{-j\beta_5 z} \right]$$

#### Match Boundary Conditions

at 1-2 boundary,  $z = Z = 0$

$$E_x: \quad A_1 + B_1 = A_2 + B_2$$

$$H_y: \quad \frac{1}{\eta_1} [A_1 - B_1] = \frac{1}{\eta_2} [A_2 - B_2]$$

at 2-3 boundary,  $z = d$

$$E_x: \quad A_2 e^{-\Gamma_2 d} + B_2 e^{\Gamma_2 d} = A_3 + B_3$$

$$H_y: \quad \frac{1}{\eta_2} [A_2 e^{-\Gamma_2 d} - B_2 e^{\Gamma_2 d}] = \frac{1}{\eta_3} [A_3 - B_3]$$

at 3-4 boundary,  $z = d + L$

$$E_x: \quad A_3 e^{-\Gamma_3(L)} + B_3 e^{\Gamma_3(L)} = A_4 + B_4$$

$$H_y: \quad \frac{1}{\eta_3} [A_3 e^{-\Gamma_3(L)} - B_3 e^{\Gamma_3(L)}] = \frac{1}{\eta_4} [A_4 - B_4]$$

at 4-5 boundary,  $z = 2d + L$

$$E_x: \quad A_4 e^{-\Gamma_4 d} + B_4 e^{\Gamma_4 d} = A_5$$

$$H_y: \quad \frac{1}{\eta_4} [A_4 e^{-\Gamma_4 d} - B_4 e^{\Gamma_4 d}] = \frac{1}{\eta_5} A_5$$

$$\eta_1 = \eta_5$$

$$\eta_2 = \eta_4 = \eta_g$$

Solve 8 equations in 7 unknowns simultaneously

$$B_4 e^{\Gamma_4 d} = A_5 - A_4 e^{-\Gamma_4 d}$$

$$B_4 = A_5 e^{-\Gamma_4 d} - A_4 e^{-2\Gamma_4 d}$$

$$\frac{1}{\eta_4} [A_4 e^{-\Gamma_4 d} - (A_5 e^{-\Gamma_4 d} - A_4 e^{-2\Gamma_4 d}) e^{\Gamma_4 d}] = \frac{1}{\eta_5} A_5$$

$$[A_4 e^{-\Gamma_4 d} - A_5 + A_4 e^{-\Gamma_4 d}] = \frac{\eta_4}{\eta_5} A_5$$

$$A_4 [2e^{-\Gamma_4 d}] = \left[ \frac{\eta_4}{\eta_5} + 1 \right] A_5$$

$$A_4 = \frac{1}{2} e^{\Gamma_4 d} \left[ 1 + \frac{\eta_4}{\eta_5} \right] A_5$$

$$B_4 = \left\{ A_5 - \frac{1}{2} e^{\Gamma_4 d} \left[ 1 + \frac{\eta_4}{\eta_5} \right] A_5 e^{-\Gamma_4 d} \right\} e^{-\Gamma_4 d}$$

$$= \left\{ A_5 - \frac{1}{2} \left[ 1 + \frac{\eta_4}{\eta_5} \right] A_5 \right\} e^{-\Gamma_4 d}$$

$$= \left[ \frac{1}{2} - \frac{1}{2} \frac{\eta_4}{\eta_5} \right] A_5 e^{-\Gamma_4 d}$$

$$B_4 = \frac{A_5}{2} e^{-\Gamma_4 d} \left[ 1 - \frac{\eta_4}{\eta_5} \right]$$

$$A_4 = \frac{A_5}{2} e^{\Gamma_4 d} \left[ 1 + \frac{\eta_4}{\eta_5} \right]$$

so

$$B_3 e^{\Gamma_3 L} = A_4 + B_4 - A_3 e^{-\Gamma_3 L}$$

$$B_3 = A_4 e^{-\Gamma_3 L} + B_4 e^{-\Gamma_3 L} - A_3 e^{-2\Gamma_3 L}$$

$$A_3 e^{-\Gamma_3 L} - B_3 e^{\Gamma_3 L} = \frac{\eta_3}{\eta_4} [A_4 - B_4]$$

$$A_3 e^{-\Gamma_3 L} - \left[ A_4 e^{-\Gamma_3 L} + B_4 e^{-\Gamma_3 L} - A_3 e^{-2\Gamma_3 L} \right] e^{\Gamma_3 L}$$

$$= \frac{\eta_3}{\eta_4} [A_4 - B_4]$$

$$A_3 e^{-\Gamma_3 L} - A_4 - B_4 + A_3 e^{-\Gamma_3 L} = \frac{\eta_3}{\eta_4} [A_4 - B_4]$$

$$A_3 2e^{-\Gamma_3 L} = \frac{\eta_3}{\eta_4} [A_4 - B_4] + A_4 + B_4$$

$$= A_4 \left[ \frac{\eta_3}{\eta_4} + 1 \right] + B_4 \left[ 1 - \frac{\eta_3}{\eta_4} \right]$$

$$A_3 = \frac{A_4}{2} e^{\Gamma_3 L} \left[ 1 + \frac{\eta_3}{\eta_4} \right] + \frac{B_4}{2} e^{\Gamma_3 L} \left[ 1 - \frac{\eta_3}{\eta_4} \right]$$

$$B_3 = A_4 e^{-\Gamma_3 L} + B_4 e^{-\Gamma_3 L} - \frac{A_4}{2} e^{-\Gamma_3 L} \left[ 1 + \frac{\eta_3}{\eta_4} \right] - \frac{B_4}{2} e^{-\Gamma_3 L} \left[ 1 - \frac{\eta_3}{\eta_4} \right]$$

$$= A_4 e^{-\Gamma_3 L} \left[ 1 - \frac{1}{2} - \frac{1}{2} \frac{\eta_3}{\eta_4} \right] + B_4 e^{-\Gamma_3 L} \left[ 1 - \frac{1}{2} + \frac{1}{2} \frac{\eta_3}{\eta_4} \right]$$

$$= \frac{A_4}{2} e^{-\Gamma_3 L} \left[ 1 - \frac{\eta_3}{\eta_4} \right] + \frac{B_4}{2} e^{-\Gamma_3 L} \left[ 1 + \frac{\eta_3}{\eta_4} \right]$$

$$A_3 = \frac{A_4}{2} e^{\Gamma_3 L} \left[ 1 + \frac{\eta_3}{\eta_4} \right] + \frac{B_4}{2} e^{\Gamma_3 L} \left[ 1 - \frac{\eta_3}{\eta_4} \right]$$

$$B_3 = \frac{A_4}{2} e^{-\Gamma_3 L} \left[ 1 - \frac{\eta_3}{\eta_4} \right] + \frac{B_4}{2} e^{-\Gamma_3 L} \left[ 1 + \frac{\eta_3}{\eta_4} \right]$$

Similarly

$$A_2 = \frac{A_3}{2} e^{\Gamma_2 d} \left[ 1 + \frac{\eta_2}{\eta_3} \right] + \frac{B_3}{2} e^{\Gamma_2 d} \left[ 1 - \frac{\eta_2}{\eta_3} \right]$$

$$B_2 = \frac{A_3}{2} e^{-\Gamma_2 d} \left[ 1 - \frac{\eta_2}{\eta_3} \right] + \frac{B_3}{2} e^{-\Gamma_2 d} \left[ 1 + \frac{\eta_2}{\eta_3} \right]$$

$$A_1 = \frac{A_2}{2} \left[ 1 + \frac{\eta_1}{\eta_2} \right] + \frac{B_2}{2} \left[ 1 - \frac{\eta_1}{\eta_2} \right]$$

$$B_1 = \frac{A_2}{2} \left[ 1 - \frac{\eta_1}{\eta_2} \right] + \frac{B_2}{2} \left[ 1 + \frac{\eta_1}{\eta_2} \right]$$

$$A_3 = \frac{1}{2} e^{\Gamma_3 L} \left[ \frac{A_5}{2} e^{\Gamma_4 d} \left( 1 + \frac{\eta_4}{\eta_5} \right) \right] \left[ 1 + \frac{\eta_3}{\eta_4} \right] \\ + \frac{1}{2} e^{\Gamma_3 L} \left[ \frac{A_5}{2} e^{-\Gamma_4 d} \left( 1 - \frac{\eta_4}{\eta_5} \right) \right] \left[ 1 - \frac{\eta_3}{\eta_4} \right]$$

$$A_3 = \frac{A_5}{4} e^{\Gamma_3 L} e^{\Gamma_4 d} \left( 1 + \frac{\eta_4}{\eta_5} \right) \left( 1 + \frac{\eta_3}{\eta_4} \right) + \frac{A_5}{4} e^{\Gamma_3 L} e^{-\Gamma_4 d} \left( 1 - \frac{\eta_4}{\eta_5} \right) \left( 1 - \frac{\eta_3}{\eta_4} \right)$$

$$B_3 = \frac{1}{2} e^{-\Gamma_3 L} \left[ \frac{A_5}{2} e^{\Gamma_4 d} \left( 1 + \frac{\eta_4}{\eta_5} \right) \right] \left[ 1 - \frac{\eta_3}{\eta_4} \right] \\ + \frac{1}{2} e^{-\Gamma_3 L} \left[ \frac{A_5}{2} e^{-\Gamma_4 d} \left( 1 - \frac{\eta_4}{\eta_5} \right) \right] \left[ 1 + \frac{\eta_3}{\eta_4} \right]$$

$$B_3 = \frac{A_5}{4} e^{-\Gamma_3 L} e^{\Gamma_4 d} \left( 1 + \frac{\eta_4}{\eta_5} \right) \left( 1 - \frac{\eta_3}{\eta_4} \right) + \frac{A_5}{4} e^{-\Gamma_3 L} e^{-\Gamma_4 d} \left( 1 - \frac{\eta_4}{\eta_5} \right) \left( 1 + \frac{\eta_3}{\eta_4} \right)$$

$$A_2 = \frac{1}{2} e^{\Gamma_2 d} \left[ 1 + \frac{\eta_2}{\eta_3} \right] \left[ \frac{A_5}{4} e^{\Gamma_3 L} e^{\Gamma_4 d} \left( 1 + \frac{\eta_4}{\eta_5} \right) \left( 1 + \frac{\eta_3}{\eta_4} \right) + \right.$$

$$\left. \frac{A_5}{4} e^{\Gamma_3 L} e^{-\Gamma_4 d} \left( 1 - \frac{\eta_4}{\eta_5} \right) \left( 1 - \frac{\eta_3}{\eta_4} \right) \right]$$

$$+ \frac{1}{2} e^{\Gamma_2 d} \left[ 1 - \frac{\eta_2}{\eta_3} \right] \left[ \frac{A_5}{4} e^{-\Gamma_3 L} e^{\Gamma_4 d} \left( 1 + \frac{\eta_4}{\eta_5} \right) \left( 1 - \frac{\eta_3}{\eta_4} \right) \right.$$

$$\left. + \frac{A_5}{4} e^{-\Gamma_3 L} e^{-\Gamma_4 d} \left( 1 - \frac{\eta_4}{\eta_5} \right) \left( 1 + \frac{\eta_3}{\eta_4} \right) \right]$$

$$A_2 = \frac{A_5}{8} e^{\Gamma_2 d} e^{\Gamma_3 L} e^{\Gamma_4 d} \left(1 + \frac{\eta_2}{\eta_3}\right) \left(1 + \frac{\eta_3}{\eta_4}\right) \left(1 + \frac{\eta_4}{\eta_5}\right)$$

$$+ \frac{A_5}{8} e^{\Gamma_2 d} e^{\Gamma_3 L} e^{-\Gamma_4 d} \left(1 + \frac{\eta_2}{\eta_3}\right) \left(1 - \frac{\eta_3}{\eta_4}\right) \left(1 - \frac{\eta_4}{\eta_5}\right)$$

$$+ \frac{A_5}{8} e^{\Gamma_2 d} e^{-\Gamma_3 L} e^{\Gamma_4 d} \left(1 - \frac{\eta_2}{\eta_3}\right) \left(1 - \frac{\eta_3}{\eta_4}\right) \left(1 + \frac{\eta_4}{\eta_5}\right)$$

$$+ \frac{A_5}{8} e^{\Gamma_2 d} e^{-\Gamma_3 L} e^{-\Gamma_4 d} \left(1 - \frac{\eta_2}{\eta_3}\right) \left(1 + \frac{\eta_3}{\eta_4}\right) \left(1 - \frac{\eta_4}{\eta_5}\right)$$

$$B_2 = \frac{1}{2} e^{-\Gamma_2 d} \left[1 - \frac{\eta_2}{\eta_3}\right] \left[\frac{A_5}{4} e^{\Gamma_3 L} e^{\Gamma_4 d} \left(1 + \frac{\eta_3}{\eta_4}\right) \left(1 + \frac{\eta_4}{\eta_5}\right)\right.$$

$$\left. + \frac{A_5}{4} e^{\Gamma_3 L} e^{-\Gamma_4 d} \left(1 - \frac{\eta_3}{\eta_4}\right) \left(1 - \frac{\eta_4}{\eta_5}\right)\right]$$

$$+ \frac{1}{2} e^{-\Gamma_2 d} \left(1 + \frac{\eta_2}{\eta_3}\right) \left[\frac{A_5}{4} e^{-\Gamma_3 L} e^{\Gamma_4 d} \left(1 - \frac{\eta_3}{\eta_4}\right) \left(1 + \frac{\eta_4}{\eta_5}\right)\right.$$

$$\left. + \frac{A_5}{4} e^{-\Gamma_3 L} e^{-\Gamma_4 d} \left(1 + \frac{\eta_3}{\eta_4}\right) \left(1 - \frac{\eta_4}{\eta_5}\right)\right]$$

$$B_2 = \frac{A_5}{8} e^{-\Gamma_2 d} e^{\Gamma_3 L} e^{\Gamma_4 d} \left(1 - \frac{\eta_2}{\eta_3}\right) \left(1 + \frac{\eta_3}{\eta_4}\right) \left(1 + \frac{\eta_4}{\eta_5}\right)$$

$$+ \frac{A_5}{8} e^{-\Gamma_2 d} e^{\Gamma_3 L} e^{-\Gamma_4 d} \left(1 - \frac{\eta_2}{\eta_3}\right) \left(1 - \frac{\eta_3}{\eta_4}\right) \left(1 - \frac{\eta_4}{\eta_5}\right)$$

$$+ \frac{A_5}{8} e^{-\Gamma_2 d} e^{-\Gamma_3 L} e^{\Gamma_4 d} \left(1 + \frac{\eta_2}{\eta_3}\right) \left(1 - \frac{\eta_3}{\eta_4}\right) \left(1 + \frac{\eta_4}{\eta_5}\right)$$

$$\begin{aligned}
& + \frac{A_5}{8} e^{-\Gamma_2 d} e^{-\Gamma_3 L} e^{-\Gamma_4 d} \left(1 + \frac{\eta_2}{\eta_3}\right) \left(1 + \frac{\eta_3}{\eta_4}\right) \left(1 - \frac{\eta_4}{\eta_5}\right) \\
A_1 = & \frac{A_5}{16} e^{\Gamma_2 d} e^{\Gamma_3 L} e^{\Gamma_4 d} \left(1 + \frac{\eta_1}{\eta_2}\right) \left(1 + \frac{\eta_2}{\eta_3}\right) \left(1 + \frac{\eta_3}{\eta_4}\right) \left(1 + \frac{\eta_4}{\eta_5}\right) \\
& + \frac{A_5}{16} e^{\Gamma_2 d} e^{\Gamma_3 L} e^{-\Gamma_4 d} \left(1 + \frac{\eta_1}{\eta_2}\right) \left(1 + \frac{\eta_2}{\eta_3}\right) \left(1 - \frac{\eta_3}{\eta_4}\right) \left(1 - \frac{\eta_4}{\eta_5}\right) \\
& + \frac{A_5}{16} e^{\Gamma_2 d} e^{-\Gamma_3 L} e^{\Gamma_4 d} \left(1 + \frac{\eta_1}{\eta_2}\right) \left(1 - \frac{\eta_2}{\eta_3}\right) \left(1 - \frac{\eta_3}{\eta_4}\right) \left(1 + \frac{\eta_4}{\eta_5}\right) \\
& + \frac{A_5}{16} e^{\Gamma_2 d} e^{-\Gamma_3 L} e^{-\Gamma_4 d} \left(1 + \frac{\eta_1}{\eta_2}\right) \left(1 - \frac{\eta_2}{\eta_3}\right) \left(1 + \frac{\eta_3}{\eta_4}\right) \left(1 - \frac{\eta_4}{\eta_5}\right) \\
& + \frac{A_5}{16} e^{-\Gamma_2 d} e^{\Gamma_3 L} e^{\Gamma_4 d} \left(1 - \frac{\eta_1}{\eta_2}\right) \left(1 - \frac{\eta_2}{\eta_3}\right) \left(1 + \frac{\eta_3}{\eta_4}\right) \left(1 + \frac{\eta_4}{\eta_5}\right) \\
& + \frac{A_5}{16} e^{-\Gamma_2 d} e^{\Gamma_3 L} e^{-\Gamma_4 d} \left(1 - \frac{\eta_1}{\eta_2}\right) \left(1 - \frac{\eta_2}{\eta_3}\right) \left(1 - \frac{\eta_3}{\eta_4}\right) \left(1 - \frac{\eta_4}{\eta_5}\right) \\
& + \frac{A_5}{16} e^{-\Gamma_2 d} e^{-\Gamma_3 L} e^{\Gamma_4 d} \left(1 - \frac{\eta_1}{\eta_2}\right) \left(1 + \frac{\eta_2}{\eta_3}\right) \left(1 - \frac{\eta_3}{\eta_4}\right) \left(1 + \frac{\eta_4}{\eta_5}\right) \\
& + \frac{A_5}{16} e^{-\Gamma_2 d} e^{-\Gamma_3 L} e^{-\Gamma_4 d} \left(1 - \frac{\eta_1}{\eta_2}\right) \left(1 + \frac{\eta_2}{\eta_3}\right) \left(1 + \frac{\eta_3}{\eta_4}\right) \left(1 - \frac{\eta_4}{\eta_5}\right)
\end{aligned}$$

Therefore

$$\frac{A_1}{A_5} = \frac{1}{16\eta_2\eta_3\eta_4\eta_5} \left[ (\eta_2 + \eta_1)(\eta_3 + \eta_2)(\eta_4 + \eta_3)(\eta_5 + \eta_4) e^{(\Gamma_2 d + \Gamma_3 L + \Gamma_4 d)} \right]$$

$$\begin{aligned}
& + (\eta_2 + \eta_1)(\eta_3 + \eta_2)(\eta_4 + \eta_3)(\eta_5 - \eta_4) e^{(\Gamma_2 d + \Gamma_3 L - \Gamma_4 d)} \\
& + (\eta_2 + \eta_1)(\eta_3 - \eta_2)(\eta_4 - \eta_3)(\eta_5 + \eta_4) e^{(\Gamma_2 d - \Gamma_3 L + \Gamma_4 d)} \\
& + (\eta_2 + \eta_1)(\eta_3 - \eta_2)(\eta_4 + \eta_3)(\eta_5 - \eta_4) e^{(\Gamma_2 d - \Gamma_3 L - \Gamma_4 d)} \\
& + (\eta_2 - \eta_1)(\eta_3 - \eta_2)(\eta_4 + \eta_3)(\eta_5 + \eta_4) e^{(-\Gamma_2 d + \Gamma_3 L + \Gamma_4 d)} \\
& + (\eta_2 - \eta_1)(\eta_3 - \eta_2)(\eta_4 - \eta_3)(\eta_5 - \eta_4) e^{(-\Gamma_2 d + \Gamma_3 L - \Gamma_4 d)} \\
& + (\eta_2 - \eta_1)(\eta_3 + \eta_2)(\eta_4 - \eta_3)(\eta_5 + \eta_4) e^{(-\Gamma_2 d - \Gamma_3 L + \Gamma_4 d)} \\
& + (\eta_2 - \eta_1)(\eta_3 + \eta_2)(\eta_4 + \eta_3)(\eta_5 - \eta_4) e^{(-\Gamma_2 d - \Gamma_3 L - \Gamma_4 d)} \Big]
\end{aligned}$$

Now, thickness of medium 2 = thickness of medium 4,  $\eta_2 = \eta_4 = \eta_g$ , and

$$\Gamma_2 = \Gamma_4 = \Gamma_g$$

$$\begin{aligned}
\frac{A_1}{A_5} &= \frac{1}{16 \eta_g^2 \eta_3 \eta_5} \left[ (\eta_g + \eta_1)(\eta_3 + \eta_g)(\eta_g + \eta_3)(\eta_5 + \eta_g) e^{(2\Gamma_g d + \Gamma_3 L)} \right. \\
& + (\eta_g + \eta_1)(\eta_3 + \eta_g)(\eta_g - \eta_3)(\eta_5 - \eta_g) e^{(\Gamma_3 L)} \\
& \left. + (\eta_g + \eta_1)(\eta_3 - \eta_g)(\eta_g - \eta_3)(\eta_5 + \eta_g) e^{(2\Gamma_g d - \Gamma_3 L)} \right]
\end{aligned}$$

$$\begin{aligned}
& + (\eta_g + \eta_1)(\eta_3 - \eta_g)(\eta_g + \eta_3)(\eta_5 - \eta_g) e^{(-\Gamma_3 L)} \\
& + (\eta_g - \eta_1)(\eta_3 - \eta_g)(\eta_g + \eta_3)(\eta_5 + \eta_g) e^{(\Gamma_3 L)} \\
& + (\eta_g - \eta_1)(\eta_3 - \eta_g)(\eta_g - \eta_3)(\eta_5 - \eta_g) e^{(-2\Gamma_g d + \Gamma_3 L)} \\
& + (\eta_g - \eta_1)(\eta_3 + \eta_g)(\eta_g - \eta_3)(\eta_5 + \eta_g) e^{(-\Gamma_3 L)} \\
& + (\eta_g - \eta_1)(\eta_3 + \eta_g)(\eta_g + \eta_3)(\eta_5 - \eta_g) e^{(-2\Gamma_g d - \Gamma_3 L)}
\end{aligned}$$

which can be simplified somewhat for

$$\eta_1 = \eta_5 = \eta_0 \text{ (free space to either side of the dielectric sandwich)}$$

Break this up into four constants, C, D, E and F defined as follows:

$$\begin{aligned}
C = \frac{1}{16\eta_g^2 \eta_3 \eta_5} & \left[ (\eta_g + \eta_1)(\eta_3 + \eta_g)(\eta_g + \eta_3)(\eta_5 + \eta_g) \cdot e^{2\Gamma_g d} \right. \\
& \left. + (\eta_g - \eta_1)(\eta_3 - \eta_g)(\eta_g - \eta_3)(\eta_5 - \eta_g) \cdot e^{-2\Gamma_g d} \right]
\end{aligned}$$

$$\begin{aligned}
D = \frac{1}{16\eta_g^2 \eta_3 \eta_5} & \left[ (\eta_g + \eta_1)(\eta_3 - \eta_g)(\eta_g - \eta_3)(\eta_5 + \eta_g) \cdot e^{2\Gamma_g d} \right. \\
& \left. + (\eta_g - \eta_1)(\eta_3 + \eta_g)(\eta_g + \eta_3)(\eta_5 - \eta_g) \cdot e^{-2\Gamma_g d} \right]
\end{aligned}$$

$$E = \frac{1}{16\eta_g^2 \eta_3 \eta_5} \left[ (\eta_g + \eta_1)(\eta_3 + \eta_g)(\eta_g - \eta_3)(\eta_5 - \eta_g) \right]$$

$$\begin{aligned}
 & + (\eta_g - \eta_1)(\eta_3 - \eta_g)(\eta_g + \eta_3)(\eta_5 + \eta_g) \Big] \\
 F = & \frac{1}{16\eta_g^2\eta_3\eta_5} \left[ (\eta_g + \eta_1)(\eta_3 - \eta_g)(\eta_g + \eta_3)(\eta_5 - \eta_g) \right. \\
 & \left. + (\eta_g - \eta_1)(\eta_3 + \eta_g)(\eta_g - \eta_3)(\eta_5 + \eta_g) \right]
 \end{aligned}$$

Thus, at last,

$$\frac{A_1}{A_5} = (C + E) e^{\Gamma_3 L} + (D + F) e^{-\Gamma_3 L}$$

At millimeter wavelengths and for glass holders,  $e^{2\Gamma_g d} \gg e^{-2\Gamma_g d}$ , and thus the terms involving  $e^{-2\Gamma_g d}$  in C and D may be neglected. Thus,

$$\frac{A_1}{A_5} = \left[ K_1 e^{\Gamma_3 L} + K_2 e^{-\Gamma_3 L} \right] e^{2\Gamma_g d}$$

where  $K_1$  and  $K_2$  contain only the dominant terms of  $(C + E)$  and  $(D + F)$ , respectively. Thus,

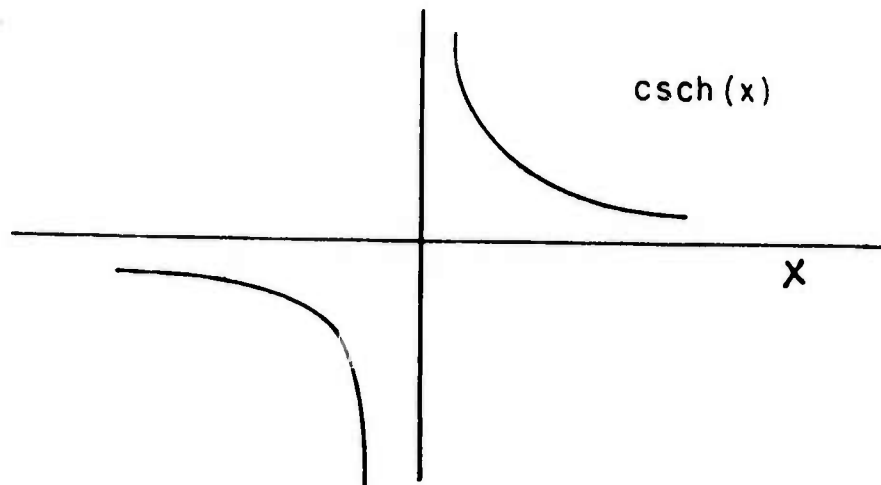
$$\begin{aligned}
 \frac{A_1}{A_5} &= \frac{(\eta_g + \eta_1)(\eta_5 + \eta_g)}{16\eta_g^2\eta_3\eta_5} \left[ (\eta_g + \eta_3)^2 e^{\Gamma_3 L} \right. \\
 & \left. + (-\eta_g + \eta_3)(\eta_g - \eta_3) e^{-\Gamma_3 L} \right] e^{2\Gamma_g d} \\
 &= \frac{(\eta_g + \eta_1)(\eta_5 + \eta_g)}{8\eta_g^2\eta_3\eta_5} \left[ \eta_3^3 \left( \frac{e^{\Gamma_3 L} - e^{-\Gamma_3 L}}{2} \right) + \eta_g^2 \left( \frac{e^{\Gamma_3 L} + e^{-\Gamma_3 L}}{2} \right) \right] e^{2\Gamma_g d}
 \end{aligned}$$

$$\begin{aligned}
 & + 2\eta_g \eta_3 \left( \frac{e^{\Gamma_3 L} - e^{-\Gamma_3 L}}{2} \right) \Big] \cdot e^{2\Gamma_g d} \\
 & = \frac{(\eta_g + \eta_1)(\eta_5 + \eta_g)(\eta_3 + \eta_g)^2}{8\eta_g^2 \eta_3 \eta_5} \sinh(\Gamma_3 L) \cdot e^{2\Gamma_g d}
 \end{aligned}$$

Thus the advancing component of the wave in medium (5) is given by the expression

$$\begin{aligned}
 E_{(5)} & = A_5 e^{-j\beta_0(2d + L + z)} \\
 & = \frac{8\eta_g^2 \eta_3 \eta_5}{(\eta_g + \eta_1)(\eta_5 + \eta_g)(\eta_3 + \eta_g)^2} \operatorname{csch}(\Gamma_3 L) \cdot e^{-2\Gamma_g d}
 \end{aligned}$$

The phase delay in medium (5) is thus a non-linear function of thickness of the dielectric since  $\operatorname{csch}(x)$  is a non-linear function which looks like



and the factor  $e^{-2\Gamma d}$  attenuates both the amplitude and phase variation.

Thus it is important that the glass dielectric holding material be as thin as possible. From this expression for E(5) it is clear that the measured phase variation would not be a linear function of (water) thickness, but would rather have some periodic, damped variation about a straight line best fitting the observed data points.